University of Alberta

Modal decomposition of tidally-forced internal waves (reconstructed from timeseries data)

by

Alexis K. Kaminski

A thesis submitted to the Faculty of Graduate Studies and Research in partial fulfillment of the requirements for the degree of

Master of Science

Department of Mechanical Engineering

Fall 2012
Edmonton, Alberta

Abstract

An algorithm is presented that disentangles the temporal and spatial structure of polychromatic internal wave fields generated through tidal conversion without *a-priori* knowledge of the topographic details. This spatial structure is relevant in estimating the location of ocean mixing. Using the $(J+1)$ forcing frequencies associated with the wave field, a $2(J+1)\times 2(J+1)$ system is solved yielding, mode-by-mode, the frequency-specific mode strengths γ_{jn} or normalized mode strength ratios $\gamma_{jn}/|\gamma_{j1}|$, where $j = 0, \ldots, J$. Both linear and nonlinear stratifications are considered.

Synthetic data at laboratory and oceanographic length scales are used for verification. Excellent agreement is seen between recovered mode strengths and theoretical values from the synthetic data when using exact forcing frequencies. When forcing frequencies are determined via fast Fourier transform, the agreement is slightly less robust, with up to 18% error, although qualitative trends are still well captured. The algorithm may therefore be extended to problems of internal wave generation beyond tidal conversion.

Acknowledgements

I would like to take a moment to thank those people who have helped me through the last couple of years. I have been really lucky to have such a great support network! In particular, I'd like to thank my family for their unending patience throughout my academic (and other) pursuits, and my friends, who are always there to listen to me talk endlessly about my research (both when the project was going well and when things were somewhat more stressful).

However, most of all, I'd like to thank my supervisor, Dr. Morris Flynn. His support has been invaluable throughout the ups and downs of the last couple of years, and I have never doubted that he has my best interests in mind. Choosing to work with him this degree was one of the best decisions I've made, and I couldn't have asked for a better supervisor.

Financial support was generously provided by the University of Alberta Faculties of Engineering and Graduate Studies and Research, the University of Alberta Department of Mechanical Engineering, the Government of Alberta, the Canadian Federation of University Women – Edmonton, and NSERC through an Alexander Graham Bell Canada Graduate Scholarship (Master's level).

Table of Contents

1 Introduction **1**

1.1 Internal waves 1

1.2 Ocean circulation 5

1.2.1 Energy requirements 5

1.2.2 Mechanisms of internal wave breaking 6

1.2.3 Mixing in circulation models 7

1.2.4 Analytical approaches 8

1.3 Thesis outline 9

2 Linear stratification **16**

2.1 Background 16

2.2 Theory 19

2.2.1 Formulation 19

2.2.2 Basic modal decomposition 23

2.3 Sparse discrete frequency spectrum 26

2.3.1 Frequency recovery 26

2.3.2 Mode recovery 29

2.4 Dense discrete frequency spectrum 34

2.4.1 All frequencies resolved from $\Theta = 40°$ to $\Theta = 50°$ 34

2.4.2 Unresolved frequencies above or below the main frequency range 37

2.5 Further considerations 37

2.5.1 Errors from neglected frequencies . . . 37
2.5.2 Bandpass filters for isolation of frequency components . . 42
2.5.3 Continuous frequency spectrum . . . 45
2.6 Discussion and conclusions . . . 52
2.A Zero-padding . . . 54
2.B Sample windows and frequency spectra . . . 56

3 Nonlinear stratification 62
3.1 Background . . . 62
3.2 Theory . . . 63
3.2.1 Formulation . . . 63
3.2.2 Modal decomposition . . . 66
3.3 Laboratory scales . . . 68
3.3.1 Frequency recovery . . . 70
3.3.2 Mode recovery . . . 72
3.4 Oceanographic scales . . . 74
3.5 Discussion and conclusions . . . 78
3.A Derivation of expressions from § 3.2.2 . . . 81
3.A.1 Derivation of the expression for β_{jn} . . . 81
3.A.2 Orthogonal and non-orthogonal components . . . 82

4 Conclusions 87
4.1 Summary of present contribution . . . 87
4.1.1 Linear stratification . . . 87
4.1.2 Nonlinear stratification . . . 90
4.2 Outlook and future work . . . 92

A Implementation in MATLAB 97
A.1 FFT routine for frequency recovery . . . 97

A.2 Mode recovery in a linear stratification 99
A.3 Mode recovery in a nonlinear stratification 102

List of Tables

2.1 Condition numbers vs. $\Delta\omega$ for the A matrix calculated for mode 1 with Θ ranging from 40° to 50°. 47

2.A.1 Effects of zero-padding on values of ω/N returned by FFT. . . . 56

3.3.1 Mode 1 relative values of β_{jn} and ς_{jn} when mapped onto the basis functions $\cos\omega_j t$ and $\sin\omega_j t$, at $x/h = 1$. Forcing frequencies ω_j are expressed in rad/s. 73

3.4.1 Primary tidal constituents included in the internal wave fields of figures 3.4.1 and 3.4.2. (Frequencies are based on data from NOAA Tides & Currents website (`http://co-ops.nos.noaa.gov/`).) 76

List of Figures

1.1 Structure of the first three vertical modes in linear stratification. The superposed vectors indicate the associated vertical velocities for each mode. 3

2.1 Parameter space for the current work. 19

2.2 Subcritical vs. supercritical internal wave fields. 21

2.3 Nondimensional vertical velocity field $w/(Nh)$ for seven superposed forcing frequencies. Note the left-to-right symmetry of the wave field. 27

2.4 Nondimensional vertical velocity field $w/(Nh)$ at $x/h = 1$ for $NT = 438$ ($T = 600\,\mathrm{s}$) for seven discrete forcing frequencies. . . 27

2.5 Tradeoff between sidelobe attenuation and mainlobe width of three windows in the frequency domain. 29

2.6 Mode strength magnitudes for the case of seven discrete forcing frequencies, with known excursion values δ_j. 31

2.7 As in figure 2.6 but showing the normalized mode strengths $|\gamma_{jn}|/|\gamma_{j1}|$. 33

2.8 FFT outputs with additional frequencies. 35

2.9 Mode strengths with additional frequencies. 36

2.10 Mode strength magnitudes for a flow field consisting of forcing frequencies corresponding to $\Theta = 40.00°$ to $50.00°$, with frequencies spaced at intervals of $0.25°$. 38

2.11 FFT output for wave fields with additional frequencies either above or below the primary range being considered. 39
2.12 Mode strength magnitudes corresponding to $\Theta = 40.00°$ to $\Theta = 50.00°$ with additional frequencies above or below. 40
2.13 Comparison of a filtered wave field with a reference wave field. . 43
2.14 Comparison of mode strength ratios obtained using the polychromatic matrix equation with those calculated from a filtered wave field. 45
2.15 Nondimensional vertical velocities at four times for frequencies corresponding to a "continuum" from $\Theta = 40.00°$ to $\Theta = 50.00°$. 49
2.16 Nondimensional vertical velocity field at $x/h = 1$ for $-NT/2 = -1642.5$ (-2250 s) to $NT/2 = 1642.5$ (2250 s) with frequencies corresponding to $\Theta = 40.00°$ to $\Theta = 50.00°$. The colourbar limits have been set to ± 0.1; the vertical velocities saturate the colourbar limits for small values of $|Nt|$. 50
2.17 Frequency spectrum for a band of frequencies corresponding to internal waves with angles of $\Theta = 40.00°$ to $\Theta = 50.00°$. 50
2.18 Mode strength ratios calculated using generating frequencies for the scenario of unresolved interstitial frequencies. 51
2.A.1 The effects of zero-padding and windowing on FFT outputs. . . 55
2.B.1 Increased side peaks in FFT with interstitial frequencies. 57
2.B.2 Results of the convolution of $\operatorname{sinc} t$ with the Heaviside step function. 58

3.3.1 Snapshot of nondimensional vertical velocities of internal wave field being considered. 69
3.3.2 Model stratification for laboratory length scales. 70
3.3.3 Nondimensional vertical velocity timeseries data for the internal wave field given by figure 3.3.1. 71

3.3.4 Frequency spectra of the vertical velocity data shown in figure 3.3.3. 72
3.3.5 Mode strengths calculated from the vertical velocity timeseries data of figure 3.3.3. 75
3.4.1 Snapshot of nondimensional vertical velocity field $w/(N_{\text{ave}}h)$ for oceanographic length scales. 76
3.4.2 Nondimensional vertical velocity timeseries data $w/(N_{\text{ave}}h)$ corresponding to the wave field in figure 3.4.1. Panel (a) is measured at $x/h = 3$, while panel (b) is measured at $x/h = -3$, for $N_{\text{ave}}T = 359$ ($T = 168\,\text{hr}$). 77
3.4.3 Calculated mode strengths for the synthetic data at oceanographic scales at $x/h = \pm 3$. 79

List of Symbols

A	Coefficient matrix from matrix equation.
a	One-sided characteristic horizontal length scale of topography (m).
a_{nj}	Vertical mode structure (non-dimensional).
$\mathbf{b}$	Column vector from matrix equation.
$\mathbf{b}^*, \mathbf{\Delta b}$	Column vectors from errors due to missing frequencies.
f	Coriolis frequency (rad/s).
f_{jn}	Lighthill viscosity correction factor (non-dimensional).
f_{jni}	Imaginary component of f_{jn}.
f_s	Sampling frequency (rad/s).
g	Gravitational acceleration (m/s^2).
h	Fluid depth (m).
h_0	Topographic height (m).
h_G	Topographic profile (m).
I_{mnkj}	Integral used in constructing expressions for matrix equation (m/s^2).

$J+1$	Number of frequencies present.
j, k	Subscripts indicating forcing frequencies.
k, m	Horizontal and vertical wavenumbers, respectively (m^{-1}).
m, n	Subscripts indicating mode numbers.
N	Buoyancy frequency (rad/s).
N_{ave}	Vertically-averaged buoyancy frequency (rad/s).
$\overline{N}_j$	Frequency-specific, vertically-integrated buoyancy frequency variable (rad/s).
$\mathcal{N}$	Partition length of time series (non-dimensional).
$\mathcal{N}_j$	Frequency-specific nondimensional buoyancy frequency.
p	Rescaled pressure ($\mathrm{m}^2/\mathrm{s}^2$).
T	Time series length (s).
t	Time variable (s).
U	Tidal flow speed (m/s).
u	In-plane horizontal (zonal) velocity (m/s).
v	Out-of-plane horizontal (meridional) velocity (m/s).
w	Vertical velocity (m/s).
X_j, Z or Z_j	Nondimensional horizontal and vertical coordinates, respectively.
x, z	Horizontal and vertical coordinates, respectively (m).
z'	Vertical coordinate extending downwards from fluid surface (m).

α_j	Frequency-specific internal wave ray slope (non-dimensional).
β_n	Mapped and integrated vertical velocity (m/s).
β_{jn}	Mapped and integrated vertical velocity (m^2/s^3).
β_{jn*}	"Orthogonal" component of β_{jn} (m^2/s^3).
γ	Column vector from matrix equation.
γ_{jn}	Frequency-specific complex mode strength (non-dimensional).
$\gamma_{jnr}, \gamma_{jni}$	Real and imaginary components of γ_{jn}, respectively.
Δf	Resolution of neighboring peaks in frequency spectrum (rad/s).
$\Delta x, \Delta z$	Spatial resolution (m).
$\Delta\omega_{\min}$	Minimum allowable frequency spacing in A matrix (rad/s).
δ_j	Frequency-specific tidal excursion (m).
ϵ_j	Frequency-specific criticality (non-dimensional).
ζ	Order-one coefficient of bandwidth increase due to choice of window function (non-dimensional).
Θ_j	Frequency-specific angle from vertical (rad).
θ	Buoyancy perturbation (m/s^2).
Λ	Topography height (m).
λ_x, λ_z	Horizontal and vertical wavelengths, respectively (m).
μ_j	Frequency parameter (non-dimensional).
ν	Fluid viscosity (m^2/s).

ξ_{jkn}	Coefficient for errors due to missing frequencies (m·s).
ρ_0	Reference density (kg/m^3).
$\overline{\rho}$	Unperturbed background density (kg/m^3).
σ_l, σ_r	Standard deviations for left and right sides, respectively, of $h_G(x)$ (m^{-2}).
ς_{jn}	"Non-orthogonal" component of β_{jn} (m^2/s^3).
$\boldsymbol{\Upsilon}$	Column vector from matrix equation.
$\boldsymbol{\Upsilon}^*, \boldsymbol{\Delta\Upsilon}$	Column vectors from errors due to missing frequencies.
Υ_{jn}	Product of γ_{jn} and f_{jn} (non-dimensional).
$\Upsilon_{jnr}, \Upsilon_{jni}$	Real and imaginary components of Υ_{jn}, respectively.
ϕ	Spatially-varying component of streamfunction (m).
ϕ_j	Frequency-specific phase (rad).
φ_j, φ_{kn}	Time-independent argument of oscillating component of w (non-dimensional).
χ	Excursion parameter (non-dimensional).
ψ	Streamfunction (m^2/s).
ω_j	Forcing frequency (rad/s).
$\bowtie_j$	Frequency-specific coefficient (m^2/s^3).
$\bowtie_{jn}$	Frequency-specific coefficient (m/s).

Chapter 1

Introduction

1.1 Internal waves

In a stationary continuously stratified fluid, if a fluid parcel is displaced vertically, buoyancy will act as a restoring force to return it to its initial elevation. However, due to the parcel's inertia, it will overshoot its initial location, at which point buoyancy again acts as a restoring force, but now in the opposite direction. This oscillation gives rise to internal waves [Kunze and Llewellyn Smith, 2004]. The frequency of oscillation of the displaced particle about its initial elevation is the buoyancy, or Brunt-Väisälä, frequency, $N(z)$, and is related to the background stratification in a Boussinesq fluid by [Kundu and Cohen, 2008]

$$N^2(z) = -\frac{g}{\rho_0}\frac{\mathrm{d}\overline{\rho}}{\mathrm{d}z}\,. \tag{1.1}$$

Here g is the gravitational acceleration, ρ_0 is a reference density of the fluid, and $\overline{\rho}(z)$ is the unperturbed background density.

For two-dimensional internal waves, spatial length scales can be described in terms of horizontal and vertical wavenumbers. These wavenumbers act much like "spatial frequencies" – if λ_x and λ_z are the horizontal and vertical wavelengths, respectively, then the wavenumbers k and m are defined as $k = 2\pi/\lambda_x$ and $m = 2\pi/\lambda_z$ [Kundu and Cohen, 2008]. These spatial frequencies are related to one another, the forcing frequency ω, and the buoyancy frequency N through

the dispersion relation for linear internal waves [Gill, 1982; Kundu and Cohen, 2008]

$$\omega^2 = \frac{N^2 k^2}{k^2 + m^2}\,. \tag{1.2}$$

In the presence of rotation, (1.2) becomes

$$\omega^2 = \frac{N^2 k^2 + f^2 m^2}{k^2 + m^2}\,, \tag{1.3}$$

where f is the Coriolis frequency [Gill, 1982]. Furthermore, the slope of the internal wave rays can be defined as [Garrett and Kunze, 2007]

$$\alpha = \sqrt{\frac{\omega^2 - f^2}{N^2 - \omega^2}}\,, \tag{1.4}$$

and the angle from vertical as [Echeverri et al., 2009]

$$\Theta = \cos^{-1}\sqrt{\frac{\omega^2 - f^2}{N^2 - f^2}}\,. \tag{1.5}$$

In the case of linear internal waves generated by a solid body oscillating at multiple frequencies, propagating waves will be excited at the same frequencies as the forcing frequencies provided they are below N [St. Laurent and Garrett, 2002]. Additionally, by employing a rigid-lid boundary condition at the upper (and lower) surface, the vertical structure of the resulting internal waves is restricted to a series of normal modes with $m_n = n\pi/h, n = 1, 2, 3, \ldots$, where h is the fluid depth [Echeverri et al., 2009]. For a linear background stratification, these modes are simply the sinusoids shown in figure 1.1 for the vertical velocity field.

For internal waves, the phase velocity (velocity of propagation of the wave crests, defined in two dimensions as $\mathbf{c}_p = \langle \omega k_x/[k_x^2 + k_z^2], \omega k_z/[k_x^2 + k_z^2]\rangle$) and group velocity (velocity of propagation of the wave energy, defined as $\mathbf{c}_g = \langle \partial\omega/\partial k_x, \partial\omega/\partial k_z\rangle$) are vector quantities [Gill, 1982; Sutherland, 2010]. Unlike surface waves, these velocities are not in the same direction; in fact, in the case of an incompressible fluid, these vectors are perpendicular (with the same sign

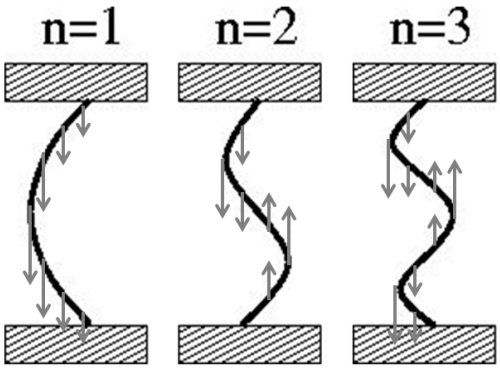

Figure 1.1: Structure of the first three vertical modes in linear stratification. The superposed vectors indicate the associated vertical velocities for each mode.

in the horizontal direction but opposite sign in the vertical direction) [Kundu and Cohen, 2008]. For internal waves in a non-rotating finite-depth fluid with a rigid-lid surface and constant N, the group velocity for mode n is [Baines, 1995]

$$\begin{aligned} \mathbf{c}_{g,n} &= \left\langle \frac{m_n^2 N}{(k^2+m_n^2)^{3/2}}, \frac{-k m_n N}{(k^2+m_n^2)^{3/2}} \right\rangle \\ &= \left\langle \frac{(n\pi/h)^2 N}{(k^2+(n\pi/h)^2)^{3/2}}, \frac{-k(n\pi/h) N}{(k^2+(n\pi/h)^2)^{3/2}} \right\rangle, \end{aligned} \tag{1.6}$$

which has magnitude $|\mathbf{c}_{g,n}| = Nh\sin^2\Theta/(n\pi)$. As such, it is clear that high modes are associated with lower group velocities and thus slower propagation of energy than low modes [St. Laurent and Garrett, 2002].

Internal waves are a common feature in the atmosphere and ocean [Sutherland, 2010]. In the atmosphere, they can be excited in the form of lee waves due to flow over mountain ranges (e.g. the Rocky Mountains) [Gill, 1982] or by anvil clouds intruding into the tropopause [Flynn and Sutherland, 2004]. In atmospheric settings, these waves can affect atmospheric circulation, but may also pose a serious risks when piloting aircraft [Sutherland, 2010]. In the ocean, internal waves can be generated through the action of wind at the sea surface [Wunsch and Ferrari, 2004] or through tidal flow over seafloor topography (including islands, midocean ridges, oceanic trenches, and the continental shelves) [St. Laurent and Garrett, 2002]. These tidally-forced internal waves are the

focus of this thesis.

Tide-topography generation of internal waves in the ocean is observed by satellite altimetry measurements of sea surface height, which show highly localized sinks of energy from the surface tide in the ocean. These locations of increased tidal dissipation correspond to regions of rough bathymetry, at which internal tides are generated [Egbert and Ray, 2000]; additionally, the locations of enhanced dissipation differ between the diurnal and semidiurnal tidal constituents [Egbert and Ray, 2003]. Such measurements also reveal the relative importance of supercritical topography (in which the maximum topographic slope is steeper than that of the internal wave rays): although the majority of the ocean floor is subcritical with respect to the primary tidal constituents, supercritical topography contributes a disproportionately large amount to tidal conversion at the global scale [Echeverri et al., 2009]. For example, the supercritical Hawaiian Ridge has an associated tidal dissipation of approximately 20 GW [Egbert and Ray, 2000; Rudnick et al., 2003]. In contrast, the largely subcritical Mid-Atlantic Ridge sees about 100 GW of dissipation despite occupying a much greater volume of ocean, i.e. there is a much higher energy loss per unit volume over the Hawaiian Ridge than the Mid-Atlantic Ridge [Rudnick et al., 2003].

The energy in the internal waves generated through tidal conversion (i.e. the transfer of energy from the barotropic tides into the internal tides) is concentrated in the lower modes [Di Lorenzo et al., 2006]. These lower modes are able to propagate long distance, i.e. 10^3 km or more without breaking [St. Laurent and Garrett, 2002]. They thereby redistribute energy for localized mixing elsewhere in the ocean [Alford, 2003].

1.2 Ocean circulation

1.2.1 Energy requirements

The global meridional overturning circulation is the "conveyor belt" that transports $\sim 30\,\mathrm{Sv}$ of cold, salty water from polar downwelling sites to the equator, where this fluid upwells and reaches the ocean surface. (Note that $30\,\mathrm{Sv}{=}30 \times 10^6\,\mathrm{m}^3/\mathrm{s}$). Estimates of the required power to drive the observed mixing and stratification on a global scale range from 2 TW [Munk and Wunsch, 1998] to 3 TW [St. Laurent and Simmons, 2006]. This is associated with an average diapycnal diffusivity of $10^{-4}\,\mathrm{m}^2/\mathrm{s}$ [Munk, 1966].

There are numerous possible sources for the power required to drive this circulation. These include the action of the wind at the ocean surface, exchanges of heat and freshwater with the atmosphere, geothermal heating through the seafloor, tides, atmospheric pressure loading, and mixing performed by the marine biosphere [Wunsch and Ferrari, 2004; Dewar et al., 2006]. However, of these sources, the primary contributors are thought to be wind and tidal forcing, and, more conjecturally, the biosphere. The wind contributes approximately 1 TW of power to ocean circulation through the Ekman layer, and an additional 0.5 TW through the generation of inertial gravity waves (with frequencies near that of the local Coriolis frequency, f) [Wunsch and Ferrari, 2004]. The net biosphere contribution is suggested to be approximately 1 TW [Dewar et al., 2006]. Finally, of the $\sim$3.5 TW of power supplied to the ocean by the tides (due to the Earth-Moon system) [Garrett, 2003], as much as 1 TW is thought to be available for abyssal mixing due to tidal conversion (with the remainder dissipating in the shallow bottom boundary layer [Llewellyn Smith, 2011]). The tides, in particular, are a good candidate for mixing of the abyssal ocean, because they act throughout the ocean depth rather than strictly at the ocean surface [Wunsch and Ferrari, 2004].

1.2.2 Mechanisms of internal wave breaking

As previously mentioned, the process of tidal conversion causes energy to be converted from the background barotropic tides into the ocean's internal wave field. Some of these waves will break close to the generation site leading to local mixing; the remainder break at far distant continental shelves or topographic features, etc., after first propagating throughout the ocean and possibly transferring some of their energy to smaller length scales through mechanisms to be outlined below. Whether local or nonlocal, wave breaking leads to turbulence, thereby mixing the temperature and salinity fields. On a large scale, this impacts the overall ocean circulation and sea level [Jayne et al., 2004]. Wave breaking can occur via several different mechanisms, depending on the structure of the internal waves in question.

Shear instabilities lead to wave breaking, particularly near their generation point. This process is most important for high modes with very small length scales, while low modes are generally stable to shear [St. Laurent and Garrett, 2002]. An estimated 30% or less of internal wave energy is thought to be lost to turbulence near generation points through this process [St. Laurent et al., 2002].

Internal waves interacting with one another may exhibit nonlinear effects that lead to wave breaking. For example, in the Parametric Subharmonic Instability (PSI), interacting waves will result in new internal waves of subharmonic and interharmonic frequencies and larger vertical wavenumbers which are more susceptible to wave breaking, for example due to the shear flows discussed in the previous paragraph [St. Laurent and Garrett, 2002; Korobov and Lamb, 2008]. PSI is of greater concern for waves that already have a relatively large vertical wavenumber: their lower group velocities (when compared to those of low-mode waves) mean that they are much more likely to experience wave-wave

interactions before reflection from the ocean surface or floor [St. Laurent and Garrett, 2002].

Internal waves that do not break due to shear instabilities or wave-wave interactions may undergo a series of reflections from the seafloor and sea surface. During these reflections, the internal waves may interact with seafloor topography having a smaller length scale than that of the wave in question. As a result, the waves may be scattered into the smaller length scales of the topography, again becoming more susceptible to wave breaking and thus mixing [Kunze and Llewellyn Smith, 2004].

When an internal wave encounters a topographic feature with slope comparable to that of the incoming beam, it can undergo a process known as critical reflection. Equation (1.4) demonstrates that the angle of the internal wave ray is determined not by the topographic slope but rather by the background stratification and rotation. Hence reflection from a feature of similar slope leads to a focusing of the internal wave energy. This focusing leads in turn to higher amplitudes and enhanced breaking. While critical reflection may seem rather inconsequential as a wave breaking mechanism due to the requirement of coincidental slopes, a large percentage of the continental shelves have slopes that are nearly critical for the internal tide associated with the M2 (principal lunar semidiurnal) tidal constituent. As such, critical reflection can be a major contributor to wave breaking of low-mode M2 internal waves [Kunze and Llewellyn Smith, 2004].

1.2.3 Mixing in circulation models

As suggested by the previous discussion of sub- and supercritical topography, mixing in the ocean is highly localized. Observations of diffusivities in the Brazil Basin show low diffusivities directly over smooth abyssal plains, near the background value of $0.1 \times 10^{-4}\,\mathrm{m}^2/\mathrm{s}$. However, over regions of rough topography,

(for example, near the rougher though still subcritical flanks of the Mid-Atlantic Ridge), there is a marked increase in diffusivity – values may be one to two orders of magnitude higher than that of the background value [Polzin et al., 1997; Mauritzen et al., 2002].

Having a good understanding of the spatial variability of ocean mixing is very important in ocean circulation models. Because processes such as wave breaking and turbulent mixing are unresolved in such models, abyssal mixing must be parameterized as accurately as possible [Jayne, 2009]. For example, Simmons et al. [2004] find, in their computer simulations, that when mixing is set to a spatially uniform value of $0.9 \times 10^{-4}\,\mathrm{m}^2/\mathrm{s}$ (approximately the global average), their results differ greatly from simulations in which mixing is made to be spatially variable (although still with an average value of $0.9 \times 10^{-4}\,\mathrm{m}^2/\mathrm{s}$). These differences are not only quantitative (e.g. the magnitudes of the calculated upwelling and downwelling in different basins and the total energy consumption by diapycnal mixing were higher in the uniform mixing vs. the variable mixing scenario), but also qualitative. Significant differences are observed in such quantities as the diapycnal mass flux and vertically averaged flow fields (including an opposite direction of flow along certain latitudes). Additionally, when compared with results derived from observational evidence, their estimates of meridional heat transport with variable mixing were a better match with the observational data [Simmons et al., 2004]. As heat transport is a critical component of Earth's climate system [Jayne et al., 2004], proper parameterizations of mixing in ocean circulation models can thus play an important role in global climate models, whether the focus is on present-day, past, or future climate.

1.2.4 Analytical approaches

In recent years, analytical work in calculating tidal conversion has frequently taken a Green's function approach, by which an integral equation is solved to

find the structure of the internal waves forced by tidal sloshing over topography. A wide variety of scenarios are considered with this method: infinite [Balmforth et al., 2002; Balmforth and Peacock, 2009] and finite ocean depths [Llewellyn Smith and Young, 2003; Pétrélis et al., 2006; Echeverri and Peacock, 2010]; subcritical [Balmforth et al., 2002] and supercritical [Balmforth and Peacock, 2009] topographic slopes; idealized [Balmforth et al., 2002; Llewellyn Smith and Young, 2003; Pétrélis et al., 2006; Nycander, 2006; Balmforth and Peacock, 2009] and arbitrary [Echeverri and Peacock, 2010] topographic profiles [Echeverri and Peacock, 2010]; and constant [Balmforth et al., 2002; Pétrélis et al., 2006; Balmforth and Peacock, 2009] and varying [Llewellyn Smith and Young, 2003; Echeverri and Peacock, 2010] background stratifications.

More recently, Maas [2011], by mapping the wave equation onto a domain with a known solution of the hyperbolic Cauchy-Riemann equations, considers topographic profiles that do not lead to tidal conversion. He finds that minor changes to topographic profiles which normally lead to tidal conversion (such as the Gaussian profile considered by Llewellyn Smith and Young [2002]) can result in a complete absence of radiating internal wave energy. This analytical result is supported by numerical simulations and also the related analytical investigation of Pétrélis et al. [2006]. These considerations impose quite stringent demands of spatial resolution. Indeed the smoothing required by general circulation models can lead to underestimates of tidal conversion of about 20%, while inadequate resolution of topography can lead to overestimates of up to 35% [Di Lorenzo et al., 2006]. From a numerical point of view, therefore, estimates of tidal conversion are limited by the available resolution of seafloor bathymetry.

1.3 Thesis outline

In this thesis, an algorithm that determines the temporal and spatial information of a polychromatic wave field from velocity timeseries data alone is

presented. This algorithm is able to calculate the frequency-specific modal decomposition for each forcing frequency without requiring specific details of the associated topographic profile. Both linear and nonlinear background stratifications are considered. The algorithm is verified using synthetic data at both laboratory and oceanographic length scales.

The remainder of this thesis is organized as follows. § 2 presents the modal decomposition algorithm for wave fields in linear background stratification, while § 3 extends this algorithm to nonlinear background stratification. Finally, conclusions of this work are discussed in § 4, along with future considerations that outline further improvements to be made so that the algorithm can be confidently applied to real geophysical data.

Note also that § 2 and § 3 of this thesis have been submitted to the Journal of Geophysical Research – Oceans as "Modal decomposition of tidally-forced internal waves. Part 1: Linear stratification" and "Modal decomposition of tidally-forced internal waves. Part 2: Nonlinear stratification", respectively. The algorithm for linear stratification was also discussed at the European Geosciences Union General Assembly 2012, held in April 2012 in Vienna. Writing responsibilities for the journal manuscripts were shared between the author of this thesis and Dr. Morris Flynn, with the former playing a larger role than the latter. The thesis has been prepared according to the FGSR guidelines for a "paper-based" thesis; consequently, each chapter contains its own self-contained bibliography and possibly appendix or appendices.

The contributions of the author of this thesis include:

- Extending the existing modal decomposition algorithm to account for multiple forcing frequencies.
- Modifying the associated fast Fourier transform algorithm to include windowing and zero-padding.

- Analyzing the impact of additional unresolved frequencies on the recovered mode strengths.

- Considering wave fields forced by a continuum of frequencies, which requires characterizing the minimum frequency spacing within the matrix equation and examining the application of bandpass filters to isolate individual frequency components.

- Adapting the multiple-frequency algorithm to wave fields with vertically-varying buoyancy frequency $N(z)$.

- Verifying, using synthetic data, both the constant- and varying-N algorithms.

Bibliography

M. H. Alford. Redistribution of energy available for ocean mixing by long-range propagation of internal waves. *Nature*, 423:159–163, 2003.

P. G. Baines. *Topographic Effects in Stratified Flows*. Cambridge University Press, Cambridge, UK, 1995. ISBN 0-521-62923-3.

N. J. Balmforth and T. Peacock. Tidal conversion by supercritical topography. *Journal of Physical Oceanography*, 39(8):1965–1974, 2009.

N. J. Balmforth, G. R. Ierley, and W. R. Young. Tidal conversion by subcritical topography. *Journal of Physical Oceanography*, 32(10):2900–2914, 2002.

W. K. Dewar, R. J. Bingham, R. L. Iverson, D. P. Nowacek, L. C. St. Laurent, and P. H. Wiebe. Does the marine biosphere mix the ocean? *Journal of Marine Research*, 64:541–561, 2006.

E. Di Lorenzo, W. R. Young, and S. Llewellyn Smith. Numerical and analytical estimates of M_2 tidal conversion at steep oceanic ridges. *Journal of Physical Oceanography*, 36(6):1072–1084, 2006.

P. Echeverri and T. Peacock. Internal tide generation by arbitrary two-dimensional topography. *Journal of Fluid Mechanics*, 659:247–266, 2010.

P. Echeverri, M. R. Flynn, K. B. Winters, and T. Peacock. Low-mode internal tide generation by topography: an experimental and numerical investigation. *Journal of Fluid Mechanics*, 636:91–108, 2009.

G. D. Egbert and R. D. Ray. Significant dissipation of tidal energy in the deep ocean inferred from satellite altimeter data. *Nature*, 93:775–778, 2000.

G. D. Egbert and R. D. Ray. Semi-diurnal and diurnal tidal dissipation from TOPEX/Poseidon altimetry. *Geophysical Research Letters*, 30(17):1–4, 2003.

M. R. Flynn and B. R. Sutherland. Intrusive gravity currents and internal gravity wave generation in stratified fluid. *Journal of Fluid Mechanics*, 514: 355–383, 2004.

C. Garrett. Internal tides and ocean mixing. *Science*, 301:1858–1859, 2003.

C. Garrett and E. Kunze. Internal tide generation in the deep ocean. *Annual Review of Fluid Mechanics*, 39(1):57–87, 2007.

A. E. Gill. *Atmosphere-Ocean Dynamics*. Academic Press, Inc., New York, NY, 1982. ISBN 0-12-283520-4.

S. R. Jayne. The impact of abyssal mixing parameterizations in an ocean general circulation model. *Journal of Physical Oceanography*, 39:1756–1775, 2009.

S. R. Jayne, L. C. St. Laurent, and S. T. Gille. Connections between ocean bottom topography and Earth's climate. *Oceanography*, 17(1):65–74, 2004.

A. S. Korobov and K. G. Lamb. Interharmonics in internal gravity waves generated by tide-topography interaction. *Journal of Fluid Mechanics*, 611:61–95, 2008.

P. K. Kundu and I. M. Cohen. *Fluid Mechanics*. Academic Press, Inc., Burlington, MA, fourth edition, 2008.

E. Kunze and S. G. Llewellyn Smith. The role of small-scale topography in turbulent mixing of the global ocean. *Oceanography*, 17(1):55–64, 2004.

S. G. Llewellyn Smith. A conundrum in conversion. *Journal of Fluid Mechanics*, 684:1–4, 2011.

S. G. Llewellyn Smith and W. R. Young. Conversion of the barotropic tide. *Journal of Physical Oceanography*, 32(2):1554–1566, 2002.

S. G. Llewellyn Smith and W. R. Young. Tidal conversion at a very steep ridge. *Journal of Fluid Mechanics*, 495:175–191, 2003.

L. R. M. Maas. Topographies lacking tidal conversion. *Journal of Fluid Mechanics*, 684:5–24, 2011.

C. Mauritzen, K. L. Polzin, M. S. McCartney, R. C. Millard, and D. E. West-Mack. Evidence in hydrography and density fine structure for enhanced vertical mixing over the Mid-Atlantic ridge in the western Atlantic. *Journal of Geophysical Research*, 107(C10):1–19, 2002.

W. Munk and C. Wunsch. Abyssal recipes II: energetics of tidal and wind mixing. *Deep Sea Research Part I: Oceanographic Research Papers*, 45:1977–2010, 1998.

W. H. Munk. Abyssal recipes. *Deep Sea Research and Oceanographic Abstracts*, 13:707–730, 1966.

J. Nycander. Tidal generation of internal waves from a periodic array of steep ridges. *Journal of Fluid Mechanics*, 567:415, 2006.

F. Pétrélis, S. Llewellyn Smith, and W. R. Young. Tidal conversion at a submarine ridge. *Journal of Physical Oceanography*, 36(6):1053–1071, 2006.

K. L. Polzin, J. M. Toole, J. R. Ledwell, and R. W. Schmitt. Spatial variability of turbulent mixing in the abyssal ocean. *Science*, 276:93–96, 1997.

D. L. Rudnick, T. J. Boyd, R. E. Brainard, G. S. Carter, G. D. Egbert, M. C. Gregg, P. E. Holloway, J. M. Klymak, E. Kunze, C. M. Lee, M. D. Levine, D. S. Luther, J. P. Martin, M. A. Merrifield, J. N. Moum, J. D. Nash, R. Pinkel, L. Rainville, and T. B. Sanford. From tides to mixing along the Hawaiian ridge. *Science*, 301:355–357, 2003.

H. L. Simmons, S. R. Jayne, L. C. St. Laurent, and A. J. Weaver. Tidally driven mixing in a numerical model of the ocean general circulation. *Ocean Modelling*, 6:245–263, 2004.

L. St. Laurent and C. Garrett. The role of internal tides in mixing the deep ocean. *Journal of Physical Oceanography*, 32:2882–2899, 2002.

L. St. Laurent and H. Simmons. Estimates of power consumed by mixing in the ocean interior. *Journal of Climate*, 19:4877–4890, 2006.

L. C. St. Laurent, H. L. Simmons, and S. R. Jayne. Estimating tidally driven mixing in the deep ocean. *Geophysical Research Letters*, 29(23):19–22, 2002.

B. Sutherland. *Internal Gravity Waves*. Cambridge University Press, Cambridge, UK, 2010. ISBN 978-0-521-83915-0.

C. Wunsch and R. Ferrari. Vertical mixing, energy, and the general circulation of the oceans. *Annual Review of Fluid Mechanics*, 36(1):281–314, 2004.

Chapter 2

Linear stratification[1]

2.1 Background

Ocean circulation plays a critical role in global climate models in that different specifications of vertical diapycnal mixing can lead to qualitatively different results in the modelled circulation, such as model predictions of deep-ocean circulation, heat transport from the equator to poles, etc. [Jayne et al., 2004; Simmons et al., 2004]. It is thought that the meridional overturning circulation requires an approximate 2 TW of power in order to cause the observed upwelling of abyssal water [Alford, 2003]. Internal waves created by tidal forcing may account for as much as 1 TW of this requirement [Wunsch and Ferrari, 2004]. These internal waves have their energy transferred into smaller length scales through wave-wave interactions, scattering, and critical reflection, causing breaking, turbulence, and thus mixing [Kunze and Llewellyn Smith, 2004]. The mechanism and location by which this scattering and mixing occur depends on the spatial structure of the internal wave field in question [St. Laurent and Garrett, 2002]. Given the importance of correctly defining mixing in global climate models, having a robust understanding of the structure of the internal tides is desirable.

Oceanic internal waves may be generated by a variety of mechanisms. Proba-

[1] A version of this chapter has been submitted for publication. Kaminski and Flynn 2012. *Journal of Geophysical Research – Oceans.*

bly the most important of these is tidal sloshing over seafloor bathymetry, such as oceanic islands, oceanic trenches, and midoceanic ridges [St. Laurent and Garrett, 2002]. Enhanced local mixing over rough seafloor bathymetry has been observed in the Brazil Basin [Polzin et al., 1997] and in the Hawaiian Islands [Rudnick et al., 2003]. Corroborating these measurements, satellite altimetry data indicates highly localized mixing at regions of rough bottom topography, coinciding with many known locations of internal tide generation [Egbert and Ray, 2003]. Internal tides may propagate up to thousands of kilometres from their sources [Alford, 2003], leading to dissipation elsewhere, e.g. along continental shelves.

Past work has considered the problem of calculating mode strengths from the shape of the topography, often using a Green's function approach, and has subsequently calculated the tidal conversion based on these mode strengths. A variety of scenarios have been considered in this manner, including finite- [Pétrélis et al., 2006] and infinite-depth oceans [Balmforth et al., 2002; Balmforth and Peacock, 2009], constant [Pétrélis et al., 2006; Echeverri et al., 2009] and variable [Llewellyn Smith and Young, 2003; Echeverri and Peacock, 2010] stratification, shallow [Balmforth et al., 2002] and steep [Balmforth and Peacock, 2009] topographies, and idealized [Pétrélis et al., 2006] and more realistic topographic shapes [Echeverri and Peacock, 2010]. In general, the structure of the resulting wave field is very sensitive to the shape of the generating topography [Echeverri et al., 2009]. In fact, a recent analytical study suggests that small changes in topographic shape may lead to a lack of tidal conversion by the topography for given forcing and buoyancy frequencies [Maas, 2011].

Unlike this previous line of inquiry, here the inverse problem is considered: given knowledge about an internal wave field, can the mode strengths be straightforwardly recovered? The answer is an affirmative "yes" in the case of a monochromatic wave field [Echeverri et al., 2009], however this is not repre-

sentative of true tidal flows. In reality, tides are made up of multiple frequency components, and dissipation maps have been calculated for several tidal constituents [Egbert and Ray, 2003]. As such, the present work considers the case of a polychromatic wave field, with the aim of recovering the temporal and spatial modal information from given velocity information. This can be accomplished without knowledge of the specific shape of the generating topography, and thus an algorithm of general applicability is sought that can be employed in disparate locales and over length scales of interest to the experimental modeller and observationalist alike. A constant buoyancy frequency N is considered here; variable background stratification (i.e. variable N) is discussed in Chapter 3. Although attention is restricted to linear wave fields, there exist numerous complications when decomposing a polychromatic wave field even in the absence of nonlinear effects. Disentangling these details is the central objective of this investigation.

The remainder of this chapter is outlined as follows. In § 2.2, the theory governing linear internal waves in an inviscid, finite-depth ocean with constant buoyancy frequency is described, as well as the process used to recover frequency and spatial information from velocity measurements of such an internal wave field. In § 2.3 and § 2.4, the modal decomposition of synthetic data consisting of multiple sparsely-spaced and multiple densely-spaced frequencies, respectively, are considered. This is followed by § 2.5, in which further strengths and limitations of the approach are considered. Finally, in § 2.6, the algorithm described by § 2.2 is applied to wave fields forced by a continuum of frequencies, and the associated complexities arising in this scenario are discussed. Although laboratory synthetic data is examined here, the algorithm can also be applied at geophysical scales, as examined further in Chapter 3.

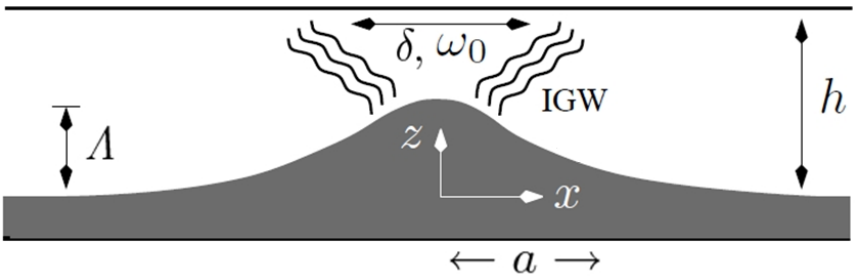

Figure 2.1: Parameter space for the current work.

2.2 Theory

2.2.1 Formulation

Figure 2.1 is a cartoon schematic showing internal wave generation by two-dimensional topography. Here, the internal wave field is assumed to be two-dimensional in an ocean of depth h. The topography is Gaussian, with a height Λ and a one-sided characteristic width a. The background tidal forcing is assumed sinusoidal

$$\mathbf{U} = \sum_{j=0}^{J} U_j \cos(\omega_j t)\hat{\mathbf{x}}\,, \tag{2.1}$$

where $U_j = \delta_j \omega_j$, with δ_j the frequency-specific tidal excursion and ω_j an individual tidal forcing frequency. Additionally, the buoyancy (Brunt-Väisäla) frequency, N, and the Coriolis frequency, f, are assumed constant. Knowing the forcing frequency, buoyancy frequency, and Coriolis frequency, the slope of the internal wave rays can be defined as [Garrett and Kunze, 2007]

$$\alpha_j = \sqrt{\frac{\omega_j^2 - f^2}{N^2 - \omega_j^2}}\,. \tag{2.2}$$

Additionally, the horizontal and vertical coordinates can be nondimensionalized and scaled as

$$X_j = \frac{\pi x}{\mu_j h} \qquad \text{and} \qquad Z = \frac{\pi z}{h} \tag{2.3}$$

in which the parameter μ_j is defined as

$$\mu_j = \frac{N}{\sqrt{\omega_j^2 - f^2}} \tag{2.4}$$

where it is now explicitly assumed that $\omega \ll N$ [Pétrélis et al., 2006]. In this hydrostatic case, relevant to many oceanographic scenarios of interest, the slope is redefined as

$$\alpha_j = \frac{\sqrt{\omega_j^2 - f^2}}{N}\,. \tag{2.5}$$

Alternatively, in a laboratory setting, the forcing frequencies are often the same order of magnitude as the buoyancy frequency [Echeverri et al., 2009] so as to avoid a rapid contamination of the wave field by waves reflected from the end walls of the tank. Also, the Coriolis frequency is typically neglible. In this case, μ and α can be redefined as:

$$\mu_j = \frac{\sqrt{N^2 - \omega_j^2}}{\omega_j} \qquad \text{and} \qquad \alpha_j = \frac{\omega_j}{\sqrt{N^2 - \omega_j^2}}\,. \tag{2.6}$$

Based on the parameters given, three important nondimensional numbers can be defined [Echeverri et al., 2009]. The excursion parameter, $\chi = \delta/a$, relates the magnitude of the tidal excursion to the width of the topography. The depth ratio, Λ/h, relates the height of the topography to the ocean depth. Finally, the criticality, ε, is defined as the ratio of the maximum topographic slope to the internal wave ray slope, α. Topography for which $\varepsilon < 1$ is referred to as "subcritical", while topography for which $\varepsilon > 1$ is "supercritical". The internal waves resulting from subcritical topography are qualitatively different from those produced by supercritical topography, as shown in figure 2.2. It can be seen that waves generated by supercritical topography will propagate both upwards and downwards from the point of excitation, while those from subcritical topography will only propagate upwards [Balmforth et al., 2002].

Solutions such as those of figure 2.2 are computed by examining the motion of the linear internal waves arising from topographic forcing with constant Coriolis

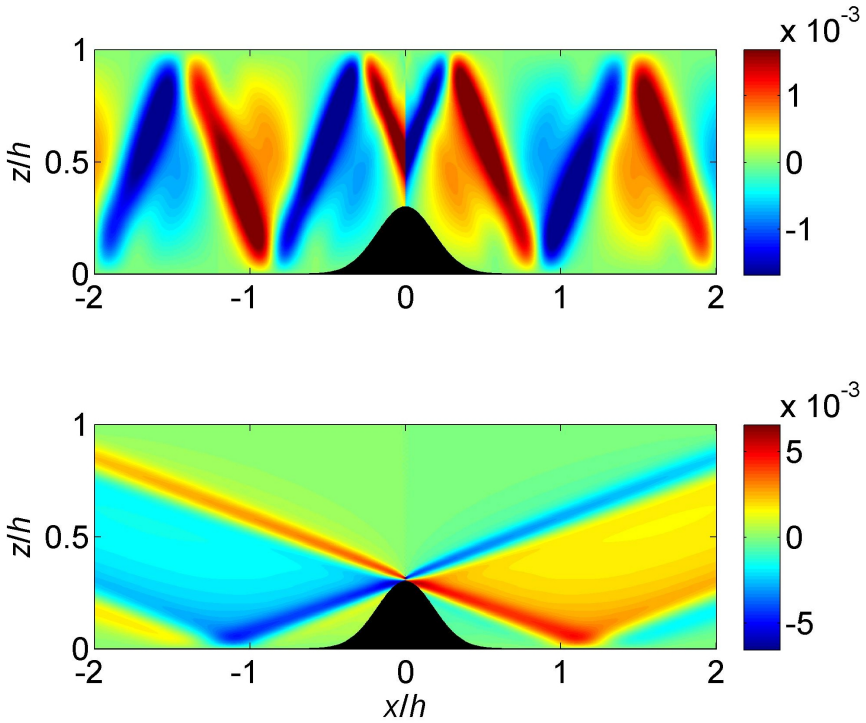

Figure 2.2: Subcritical vs. supercritical internal wave fields. The top image shows nondimensional vertical velocities ($w/(Nh)$) for a subcritical wave field ($\varepsilon < 1$) and the bottom image shows nondimensional vertical velocities for a supercritical wave field ($\varepsilon > 1$). Both images correspond to time $t = 0$. Solutions are computed using the methodology of Echeverri et al. [2009], which is itself based on the algorithm given by Pétrélis et al. [2006].

and buoyancy frequencies. This motion is dictated by the following governing equations:

$$\begin{aligned} u_t - fv + p_x &= 0 \\ v_t + fu &= 0 \\ w_t + p_z - \theta &= 0 \\ \theta_t + N^2 w &= 0 \\ u_x + w_z &= 0\,, \end{aligned} \tag{2.7}$$

which presume inviscid and non-hydrostatic flow. In the above equations, u and w are the in-plane horizontal (zonal) and vertical velocities, respectively, while v refers to the out-of-plane (meridional) component of velocity. θ is the buoyancy perturbation, while p is a rescaled pressure.

Echeverri et al. [2009] define the vertical velocity field arising from the topographic forcing of internal waves at a single frequency ω_0 as

$$w = \frac{U}{\mu}\mathrm{Real}\left\{\sum_{n=1}^{\infty}\gamma_n f_n \mathrm{e}^{-nXf_{nI}}\sin nZ\,\mathrm{e}^{\mathrm{i}(nX-\omega_0 t+\frac{\pi}{2})}\right\}, \tag{2.8}$$

and

$$f_n = f_{nR} + \mathrm{i}f_{nI} = 1 + \frac{\mathrm{i}\nu}{2\omega_0}\left(\frac{n\pi}{h}\right)^2\left[\frac{N^2}{N^2-\omega_0^2}\right]^2 \tag{2.9}$$

whose complex part is a Lighthill correction factor, added *a posteriori* in order to account for the effects of viscous dissipation on the internal waves, which is not negligible at laboratory length scales [Lighthill, 1978]. The subscripts R and I denote the real and imaginary parts, respectively. Equation (2.8) represents a solution to (2.7) under the assumption of time-periodic flow over topography, whose geometric particulars are reflected in the complex mode strengths γ_n. (Details can be found in Llewellyn Smith and Young [2003], Pétrélis et al. [2006], etc.) Expressions for the horizontal velocity field and buoyancy perturbation fields can also be obtained by suitable adaptation of (2.7). (See, for instance, Echeverri et al. [2009].)

From the assumption of a linear wave field, the vertical velocity field for multiple forcing frequencies can be written as a superposition of the contributions from each individual frequency. Thus in the polychromatic case

$$w = \sum_{j=0}^{J} \frac{\delta_j \omega_j}{\mu_j} \mathrm{Real} \left\{ \sum_{n=1}^{\infty} \gamma_{jn} f_{jn} \mathrm{e}^{-nX_j f_{jnI}} \sin nZ \, \mathrm{e}^{\mathrm{i}(nX_j - \omega_j t + \frac{\pi}{2})} \right\} , \tag{2.10}$$

in which

$$f_{jn} = 1 + \frac{\mathrm{i}\nu}{2\omega_j} \left(\frac{n\pi}{h} \right)^2 \left[\frac{N^2}{N^2 - \omega_j^2} \right]^2 \tag{2.11}$$

and $\varphi_j = nX_j + \pi/2$. By defining

$$\gamma_{jn} f_{jn} = \Upsilon_{jn} = \Upsilon_{jnR} + \mathrm{i}\Upsilon_{jnI} \, , \tag{2.12}$$

(2.10) can be written

$$w = \sum_{j=0}^{J} \frac{\delta_j \omega_j}{\mu_j} \left\{ \sum_{n=1}^{\infty} (\Upsilon_{jnR} \cos(\varphi_j - \omega_j t) - \Upsilon_{jnI} \sin(\varphi_j - \omega_j t)) \sin nZ \, \mathrm{e}^{-nX_j f_{jnI}} \right\} . \tag{2.13}$$

2.2.2 Basic modal decomposition

As previously mentioned, here the focus is not on the calculation of the mode strengths associated with a specific topographic profile and subsequent calculation of the corresponding wave field. Rather, the recovery of the mode strengths from the velocity data associated with the wave field in question is examined, without requiring specific details of the (2D) topographic shape.

By projecting the vertical velocity field onto the trigonometric basis functions $\sin nZ$, a parameter β_n can be defined as

$$\begin{aligned} \beta_n &= \int_0^{\pi} w \sin nZ \, \mathrm{d}Z \qquad (2.14) \\ &= \frac{\pi}{2} \sum_{j=0}^{J} \frac{\delta_j \omega_j}{\mu_j} \left[\Upsilon_{jnR} \cos(\varphi_j - \omega_j t) - \Upsilon_{jnI} \sin(\varphi_j - \omega_j t) \right] \mathrm{e}^{-nX_j f_{jnI}} . \end{aligned}$$

The vertical velocity field is chosen here for the purposes of mode strength recovery owing to its dependence on $\sin nZ$, rather than $\cos nZ$ as in the horizontal

velocity or perturbation buoyancy fields. Because the sine function vanishes at the boundaries $Z = 0$ and $Z = \pi$, any missing information near the extreme edges of the domain would have less overall impact on the solution than if the cosine function were used. There may be difficulties in obtaining velocity measurements at these extremities, both in experiments and in oceanographic measurements.

Mapping β_n onto the basis functions $\cos\omega_k t$ and $\sin\omega_k t$, in which $k = 0, 1, ..., J$ corresponds to each forcing frequency present, yields the following system of $2(J+1)$ equations in the $2(J+1)$ unknowns Υ_{jnR} and Υ_{jnI}:

$$\begin{aligned}\int_0^T \beta_n \cos\omega_k t \,\mathrm{d}t &= \sum_{j=0}^{J} \bowtie_{jn} \Upsilon_{jnR} \int_0^T \cos(\varphi_j - \omega_j t)\cos\omega_k t \,\mathrm{d}t \\ &\quad - \sum_{j=0}^{J} \bowtie_{jn} \Upsilon_{jnI} \int_0^T \sin(\varphi_j - \omega_j t)\cos\omega_k t \,\mathrm{d}t \end{aligned} \tag{2.15}$$

$$\begin{aligned}\int_0^T \beta_n \sin\omega_k t \,\mathrm{d}t &= \sum_{j=0}^{J} \bowtie_{jn} \Upsilon_{jnR} \int_0^T \cos(\varphi_j - \omega_j t)\sin\omega_k t \,\mathrm{d}t \\ &\quad - \sum_{j=0}^{J} \bowtie_{jn} \Upsilon_{jnI} \int_0^T \sin(\varphi_j - \omega_j t)\sin\omega_k t \,\mathrm{d}t\,. \end{aligned} \tag{2.16}$$

These equations can be written in an abbreviated matrix form as $A\boldsymbol{\Upsilon} = \mathbf{b}$, where A, $\mathbf{b}$, and $\boldsymbol{\Upsilon}$ are defined as

$$A_{ij} = \begin{cases} \bowtie_{bn} \int_0^T \cos(\varphi_b - \omega_b t)\cos\omega_c t \,\mathrm{d}t & \text{if } i = 2c+1 \text{ and } j = 2b+1 \\ -\bowtie_{bn} \int_0^T \sin(\varphi_b - \omega_b t)\cos\omega_c t \,\mathrm{d}t & \text{if } i = 2c+1 \text{ and } j = 2b+2 \\ \bowtie_{bn} \int_0^T \cos(\varphi_b - \omega_b t)\sin\omega_c t \,\mathrm{d}t & \text{if } i = 2c+2 \text{ and } j = 2b+1 \\ -\bowtie_{bn} \int_0^T \sin(\varphi_b - \omega_b t)\sin\omega_c t \,\mathrm{d}t & \text{if } i = 2c+2 \text{ and } j = 2b+2 \end{cases}, \tag{2.17}$$

$$\mathbf{b} = \begin{bmatrix} \int_0^T \beta_n \cos\omega_0 t \,\mathrm{d}t \\ \int_0^T \beta_n \sin\omega_0 t \,\mathrm{d}t \\ \int_0^T \beta_n \cos\omega_1 t \,\mathrm{d}t \\ \vdots \\ \int_0^T \beta_n \sin\omega_J t \,\mathrm{d}t \end{bmatrix}, \tag{2.18}$$

and

$$\boldsymbol{\Upsilon} = \begin{bmatrix} \Upsilon_{0nR} \\ \Upsilon_{0nI} \\ \Upsilon_{1nR} \\ \vdots \\ \Upsilon_{JnI} \end{bmatrix} . \tag{2.19}$$

Here, f_{jn} is given by (2.11), and

$$\bowtie_{jn} = \frac{\pi}{2} \frac{\delta_j \omega_j}{\mu_j} \mathrm{e}^{-nX_j f_{jnI}} . \tag{2.20}$$

The integrals in (2.17) can be evaluated analytically, thus avoiding the need for numerical integration to find the elements A_{ij}. In the case where $\omega_b = \omega_c$ (as defined in (2.17) based on the indices of A),

$$A_{ij} = \begin{cases} \bowtie_{bn} \left(\frac{T \cos\varphi_b}{2} - \frac{\sin(\varphi_b - 2\omega_b T) - \sin\varphi_b}{4\omega_b} \right) & \text{if } i = 2c+1 \text{ and } j = 2b+1 \\ \bowtie_{bn} \left(\frac{-T \sin\varphi_b}{2} - \frac{\cos(\varphi_b - 2\omega_b T) - \cos\varphi_b}{4\omega_b} \right) & \text{if } i = 2c+1 \text{ and } j = 2b+2 \\ \bowtie_{bn} \left(\frac{T \sin\varphi_b}{2} - \frac{\cos(\varphi_b - 2\omega_b T) - \cos\varphi_b}{4\omega_b} \right) & \text{if } i = 2c+2 \text{ and } j = 2b+1 \\ \bowtie_{bn} \left(\frac{T \cos\varphi_b}{2} + \frac{\sin(\varphi_b - 2\omega_b T) - \sin\varphi_b}{4\omega_b} \right) & \text{if } i = 2c+2 \text{ and } j = 2b+2 \end{cases} , \tag{2.21}$$

and in the case where $\omega_b \neq \omega_c$,

$$A_{ij} = \begin{cases} -\frac{\bowtie_{bn}}{2} \left[\frac{\sin(\varphi_b - (\omega_b + \omega_c)T)}{\omega_b + \omega_c} + \frac{\sin(\varphi_b - (\omega_b - \omega_c)T)}{\omega_b - \omega_c} - \frac{2\omega_b \sin\varphi_b}{\omega_b^2 - \omega_c^2} \right] & \text{if } i = 2c+1 \text{ and } j = 2b+1 \\ -\frac{\bowtie_{bn}}{2} \left[\frac{\cos(\varphi_b - (\omega_b + \omega_c)T)}{\omega_b + \omega_c} + \frac{\cos(\varphi_b - (\omega_b - \omega_c)T)}{\omega_b - \omega_c} - \frac{2\omega_b \cos\varphi_b}{\omega_b^2 - \omega_c^2} \right] & \text{if } i = 2c+1 \text{ and } j = 2b+2 \\ -\frac{\bowtie_{bn}}{2} \left[\frac{\cos((\omega_b + \omega_c)T - \varphi_b)}{\omega_b + \omega_c} + \frac{\cos((\omega_c - \omega_b)T + \varphi_b)}{\omega_c - \omega_b} - \frac{2\omega_c \cos\varphi_b}{\omega_c^2 - \omega_b^2} \right] & \text{if } i = 2c+2 \text{ and } j = 2b+1 \\ -\frac{\bowtie_{bn}}{2} \left[\frac{\sin(\varphi_b - (\omega_b - \omega_c)T)}{\omega_b - \omega_c} - \frac{\sin(\varphi_b - (\omega_b + \omega_c)T)}{\omega_b + \omega_c} - \frac{2\omega_c \sin\varphi_b}{\omega_b^2 - \omega_c^2} \right] & \text{if } i = 2c+2 \text{ and } j = 2b+2 \end{cases} . \tag{2.22}$$

In (2.21) and (2.22), T denotes the upper bound of integration, which need not be an integer multiple of one of the constituent forcing periods. Note, however, that there is an advantage in choosing T to be large (i.e. $TN \gg 1$ for all j), which imposes important restrictions on the application of the modal

decomposition algorithm to experimental data sets of short duration – further details are presented below.

Recalling (2.12), the (complex) mode strengths can be found from Υ_{jn} via

$$\gamma_{jn} = \frac{\Upsilon_{jnR} + f_{jnI}\Upsilon_{jnI}}{1 + f_{jnI}^2} + i\left[\Upsilon_{jnI} - \frac{f_{jnI}}{1 + f_{jnI}^2}(\Upsilon_{jnR} + f_{jnI}\Upsilon_{jnI})\right], \qquad (2.23)$$

i.e. the mode strengths can be recovered for a given vertical velocity field if w, ω_j, and $\delta_j = U_j/\omega_j$ are known. Of course in many practical instances, though not the problem of tidal conversion, ω_j may be unknown *a-priori* so that it becomes necessary to perform a temporal as well as spatial decomposition of the wave field. The requisite procedure is illustrated by way of example in the following section.

2.3 Sparse discrete frequency spectrum

2.3.1 Frequency recovery

For illustrative purposes, synthetic data are generated at individual forcing frequencies using a code based on the theory of Pétrélis et al. [2006]. Experimental evidence suggests an excellent agreement between model predictions and measured results [Echeverri et al., 2009], so this synthetic data may be regarded as surrogate laboratory data, albeit of high fidelity. The data in question correspond to a Gaussian topography at laboratory length scales, with Coriolis effects ignored. Owing again to the assumption of a linear flow field, individual frequency components are superposed to give a single flow field corresponding to multiple forcing frequencies ($\omega/N = 1/10, 1/4, 1/2, 1/\sqrt{2}, 3/4, \sqrt{3}/2$, and $9/10$). Apart from the frequency $\omega/N = 1/\sqrt{2}$ (the critical frequency for the topography in question), there is no particular significance to the frequency values chosen, and similar results would be expected for other choices of ω/N. For the range of forcing frequencies used to generate figure 2.3, the topography is simultaneously supercritical for some frequencies and subcritical for others, thereby

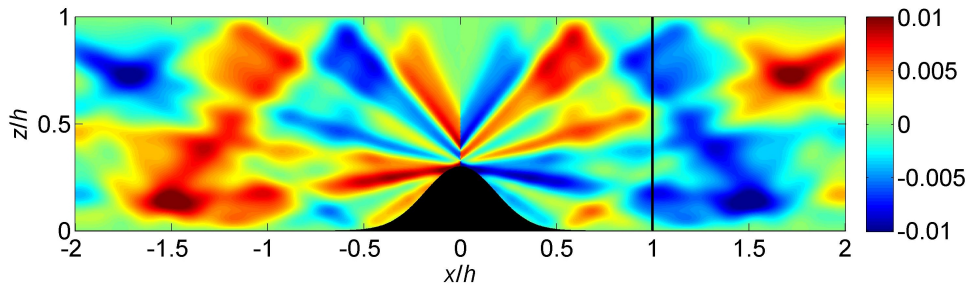

Figure 2.3: Nondimensional vertical velocity field $w/(Nh)$ for seven superposed forcing frequencies. Note the left-to-right symmetry of the wave field.

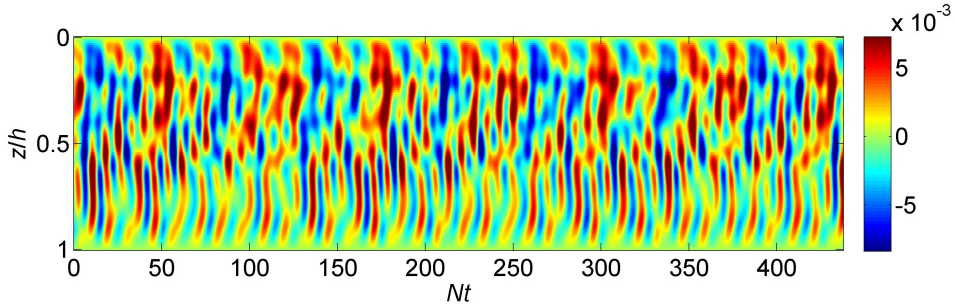

Figure 2.4: Nondimensional vertical velocity field $w/(Nh)$ at $x/h = 1$ for $NT = 438$ ($T = 600\,\mathrm{s}$) with seven discrete forcing frequencies. This x position corresponds to the vertical black line indicated in figure 2.3.

leading to qualitatively different internal wave fields being generated concurrently. For both figures 2.3 and 2.4 the spatial resolution is $\Delta x = \Delta z = h/100$.

Vertical velocity timeseries data, shown in figure 2.4, are generated at a sampling frequency of 4 Hz for a total time of $NT = 438$ ($T = 600\,\mathrm{s}$) at the location $x/h = 1$. Although the frequency information used to construct this vertical velocity field is known, for the purposes of illustrating the modal decomposition process described in § 2.2 the forcing frequencies and mode strengths are treated as unknown quantities. The "known" frequency and modal (or mode strength) information from the synthetic data can then be used to quantitatively assess the accuracy of the modal decomposition algorithm.

In order to obtain the frequency information from the vertical velocity timeseries data of figure 2.4, a fast Fourier transform (FFT) routine is employed at

each location in z. The resulting spectra are then averaged in order to give a mean frequency spectrum for the wave field. The presence of a given forcing frequency is revealed in the frequency spectrum by a peak at the corresponding frequency location. Furthermore, in the not atypical geophysical scenario in which a mean flow is superposed on the internal wave field, the presence of this flow can be detected using the frequency spectrum as a peak at frequency $\omega/N = 0$.

When using the FFT routine to find the frequency components of a given vertical velocity field, certain strategies are employed in order to improve the frequency resolution and decrease the spectral leakage of the obtained spectrum. First, due to the finite time interval, spectral leakage can become a significant concern, particularly in the scenario in which the peaks related to certain forcing frequencies have heights of the order of magnitude of the leakage from adjacent peaks. In order to combat this difficulty, window functions may be applied to the vertical velocity field being examined.

Window functions have drawbacks of their own, however. Often there is a tradeoff between the sidelobe attenuation of a given window (where stronger attenuation suppresses spectral leakage) and the mainlobe width of the peaks (where better peak resolution is given by narrower mainlobes). Of the three windows shown in figure 2.5, the rectangular window (a) has the narrowest mainlobe but poorest sidelobe attenuation, while the Parzen window (c) shows excellent sidelobe attenuation but a wide mainlobe, and the Gauss window (b) falls in between. For use on data such as that shown in figure 2.4, some sidelobe attenuation is sacrificed and the Gauss window is chosen.

The resolution Δf of neighbouring peaks in the frequency spectrum is determined by

$$\Delta f = \zeta \frac{f_s}{\mathcal{N}}\,, \tag{2.24}$$

where ζ is an order-one coefficient related to the increase in bandwidth from

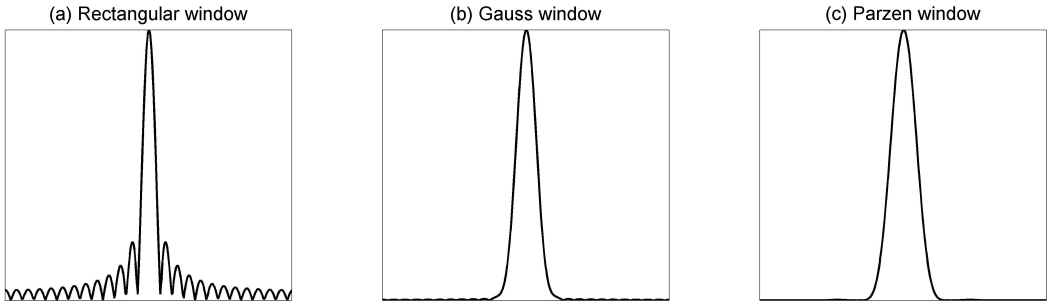

Figure 2.5: Tradeoff between sidelobe attenuation and mainlobe width of three windows in the frequency domain. The above images are obtained by applying each window to the FFT of the constant function $f(t) = 1$. The amplitudes of these peaks are not the same, but will vary depending on the window being applied.

a specific window, f_s is the sampling frequency, and $\mathcal{N}$ is the partition length [Harris, 1978]. So, for the application of a window with a wide mainlobe, the signal must be sampled for a longer period of time in order to achieve the required resolution as compared to a window with a narrower mainlobe. For a signal with closely-spaced forcing frequencies, this may lead to required sample times that are both computationally expensive and unrealistic for experimental measurements. Further details regarding the mainlobe width and sidelobe attenuation of various windows can be found in table 1 of Harris [1978].

Finally, because the frequency resolution of the FFT improves with an increase in the length of the transform, zero-padding is employed by adding additional zeros to the end of the windowed data. In Appendix 2.A, the quantitative benefit of zero-padding is examined in the context of the wave field shown in figure 2.4.

2.3.2 Mode recovery

All frequencies resolved

Upon recovery of the forcing frequencies, the complex mode strengths γ_{jn} can then be found for each forcing frequency. The method by which these mode strengths are recovered is relatively straightforward in light of the analysis of

§ 2.2.2: the frequencies are substituted into the expressions given by (2.21) and (2.22) to solve for the elements A_{ij}, and trapezoidal integration is used to solve for the elements of $\mathbf{b}$, as given by (2.18). Inverting the matrix equation then yields the values of Υ_{jnR} and Υ_{jnI} at each frequency. Finally, substitution into (2.23) gives the complex mode strengths, i.e. γ_{jn}.

However, in spite of the relative ease with which this method is implemented in MATLAB, there remain several practical considerations. Calculation of the higher mode strengths, such as those corresponding to $n = 7$ or higher, often leads to ill-conditioned matrices, particularly for higher forcing frequencies. This is largely due to the influence of the $\mathrm{e}^{-nX_j f_{jnI}} \propto \mathrm{e}^{-n^3 X_j}$ term, which approaches zero more quickly for larger ω_j and results in a division of small numbers by other small numbers, leading to relatively large round-off errors in the inversion of the A matrix [Gilat and Subramaniam, 2008]. As such, the total number of mode strengths that can be calculated is limited. In practice this is not so significant a drawback because higher modes such as $n = 7, 8, ...$ are usually much less energetic than the lower modes such as $n = 1, 2, ...$ [Di Lorenzo et al., 2006].

Determination of γ_{jn} requires that the frequency-specific tidal excursion, δ_j, be known. These calculated mode strength magnitudes, $|\gamma_{jn}|$, are shown in figure 2.6, which indicates good agreement between the calculated mode strengths and those used in generating the synthetic data. Furthermore, figure 2.6 demonstrates the importance of accuracy of the recovered frequencies; quantitative errors are apparent in the calculated mode strengths for $\omega/N = 1/2$ when using the frequency value $\omega/N = 0.4962$ returned from the FFT analysis with $NT = 438$ ($T = 600\,\mathrm{s}$) in place of the exact frequency of $\omega/N = 0.5$. It should be noted, however, that even in those plots indicating discrepancies between the calculated and exact mode strengths, there remains excellent qualitative and good quantitative agreement.

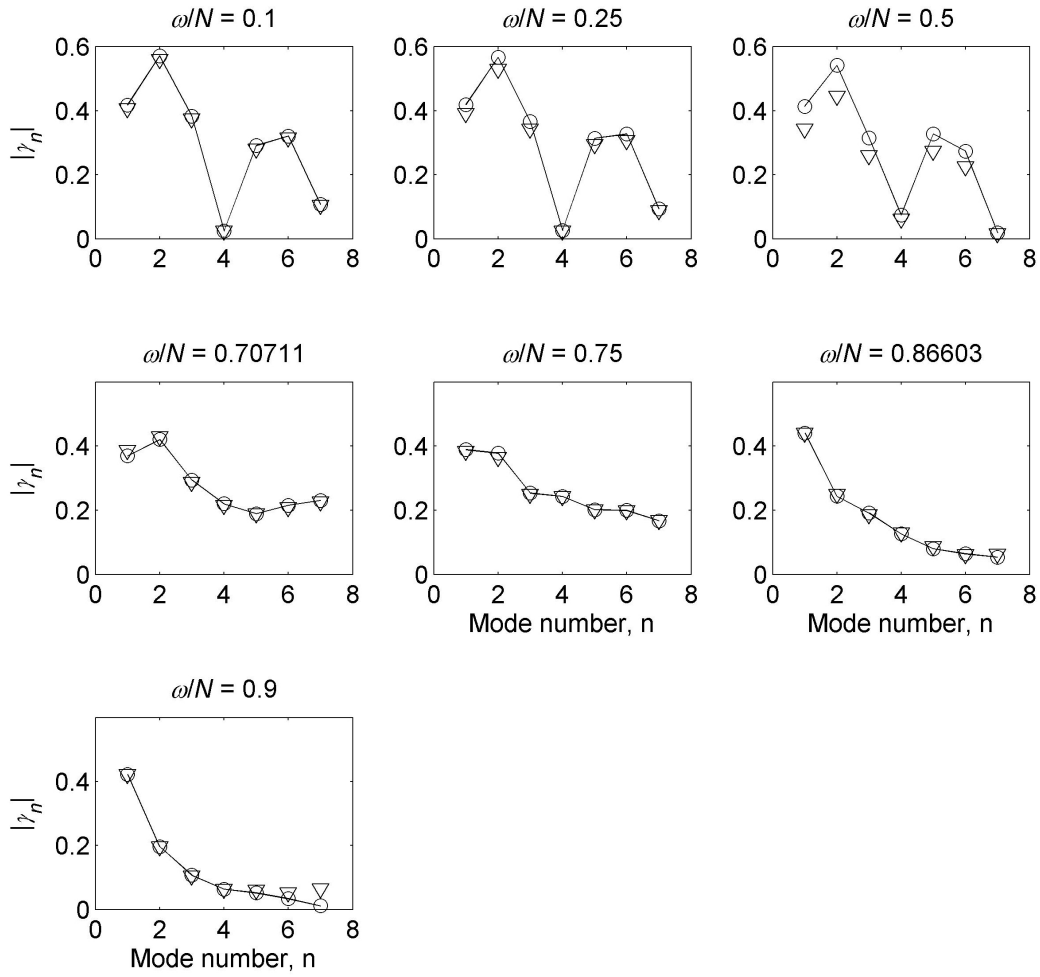

Figure 2.6: Mode strength magnitudes for the case of seven discrete forcing frequencies, with known excursion values δ_j. Here, the solid black lines indicate the exact mode strengths from synthetic data, the circles indicate the mode strengths determined using the input forcing frequencies, and the triangles indicate the mode strengths determined using the peak values from the FFT output.

In the case in which the excursion values δ_j are unknown, the exact values of the complex mode strengths are not as easily determined. More specifically, solving the matrix equation $A\boldsymbol{\Upsilon} = \mathbf{b}$ yields estimates not of γ_{jn} but rather $\gamma_{jn}\delta_j$. Note, however, that by manipulating (2.13), the vertical velocity w can be written as

$$\begin{aligned} w &= \sum_{j=0}^{J} \frac{\delta_j \omega_j}{\mu_j} \left\{ \left(\sum_{n=1}^{\infty} \left[-\Upsilon_{jnR} \sin nX - \Upsilon_{jnI} \cos nX \right] \mathrm{e}^{-nXf_{jnI}} \sin nZ \right) \cos \omega_j t \right. \\ &\quad \left. + \left(\sum_{n=1}^{\infty} \left[\Upsilon_{jnR} \cos nX - \Upsilon_{jnI} \sin nX \right] \mathrm{e}^{-nXf_{jnI}} \sin nZ \right) \sin \omega_j t \right\} . \end{aligned} \tag{2.25}$$

From (2.25), an expression for the heights of the associated peaks in the frequency spectrum can be derived. As shown by the following equation, these peak heights are proportional to the excursion values and also depend on the mode strengths.

$$\begin{aligned} \text{pk.ht.}_j^2 &= \left(\frac{\delta_j \omega_j}{\mu_j} \right)^2 \left\{ \left(\sum_{n=1}^{\infty} \left[-\Upsilon_{jnR} \sin nX - \Upsilon_{jnI} \cos nX \right] \mathrm{e}^{-nXf_{jnI}} \sin nZ \right)^2 \right. \\ &\quad \left. + \left(\sum_{n=1}^{\infty} \left[\Upsilon_{jnR} \cos nX - \Upsilon_{jnI} \sin nX \right] \mathrm{e}^{-nXf_{jnI}} \sin nZ \right)^2 \right\} . \end{aligned} \tag{2.26}$$

Provided the peak heights can be determined from an FFT analysis, (2.26) provides a second equation relating δ_j and γ_{jn} and so offers the possibility of estimating the value of one or the other parameter. On the other hand, the distinction between δ_j and γ_{jn} is somewhat arbitrary: both are a measure of wave amplitude. The effort required to further separate the two values is therefore not necessarily worth the gain, particularly because $\delta_j \gamma_{jn}$ still gives information about which modes are most energetic within the wave field at a particular forcing frequency. Therefore when δ_j is unknown, it is expedient to consider not the values $|\gamma_{jn}|$ but rather $|\gamma_{jn}|/|\gamma_{j1}|$ (figure 2.7). Note finally that one can still determine the phase information (i.e. ϕ_{jn}) even when γ_{jn} is not specifically resolved.

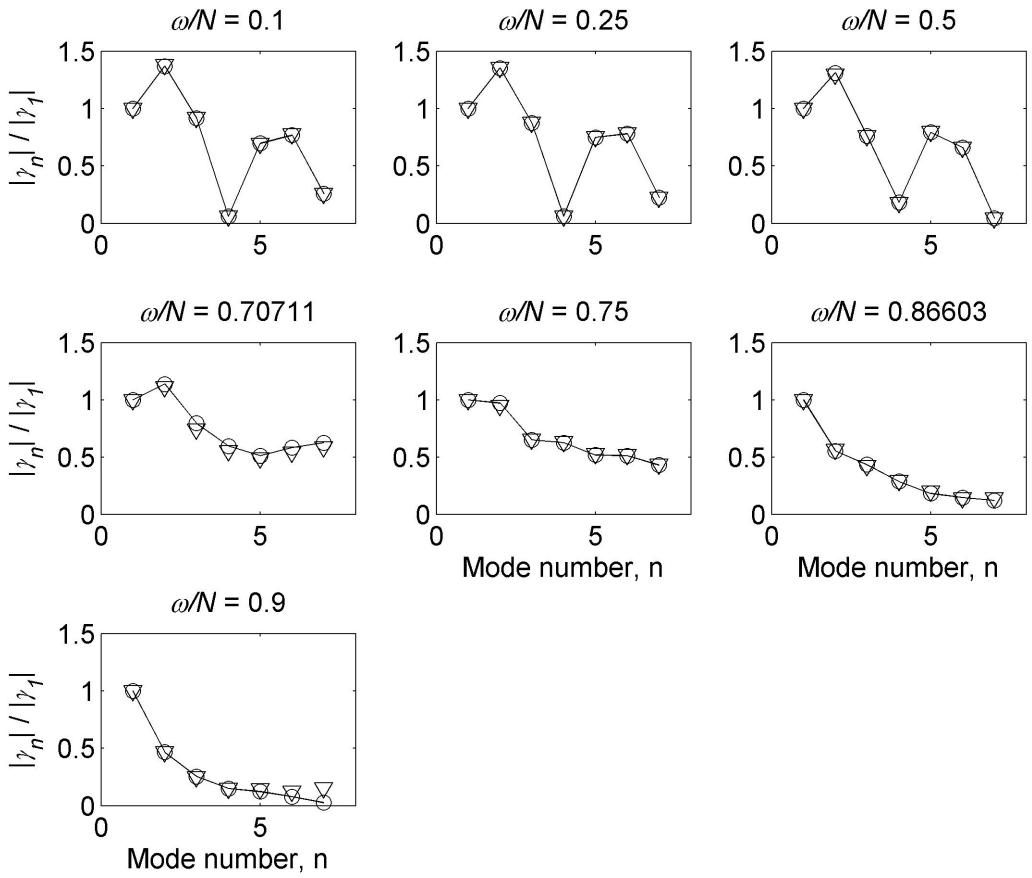

Figure 2.7: As in figure 2.6 but showing the normalized mode strengths $|\gamma_{jn}|/|\gamma_{j1}|$.

Unresolved frequencies

The previous discussion suggests scenarios in which particular frequency components are inadequately resolved and therefore go unrecognized in the spectral analysis of § 2.3.1. For example, for insufficiently long timeseries, closely-neighbouring frequencies on the FFT outputs may appear to be a single peak, as indicated by (2.24). Additionally, the peaks associated with some frequency components may be substantially smaller than those of neighbouring frequencies, causing these peaks to be overlooked when examining the frequency spectrum (particularly in instances of large spectral leakage).

In order to consider the effects of isolated unresolved frequencies on the calculated mode strengths, wave fields containing an additional low frequency component ($\omega/N = 1/20$), an additional high frequency component ($\omega/N = 19/20$), or an additional intermediate frequency component ($\omega/N = 1/\sqrt{5}$) are generated for 600 s worth of data ($NT = 438$), the frequency spectra of which are shown in figure 2.8.

To ascertain how these additional frequencies ignored when forming the system of equations described by $A\boldsymbol{\Upsilon} = \mathbf{b}$ might affect the modal decomposition of a given internal wave field, the mode strengths are calculated using only the seven frequencies listed in § 2.3.1. Results are indicated in figure 2.9 for each of the wave fields represented in figure 2.8. Fortuitously, and as is examined in more detail in § 2.5.1, the presence of the additional frequencies does not have any marked influence on the calculated mode strengths.

2.4 Dense discrete frequency spectrum

2.4.1 All frequencies resolved from $\Theta = 40^\circ$ to $\Theta = 50^\circ$

Having analyzed the scenario in which the forcing frequencies are broadly spaced and cover much of the range $0 < \omega < N$, an alternative scenario in which the

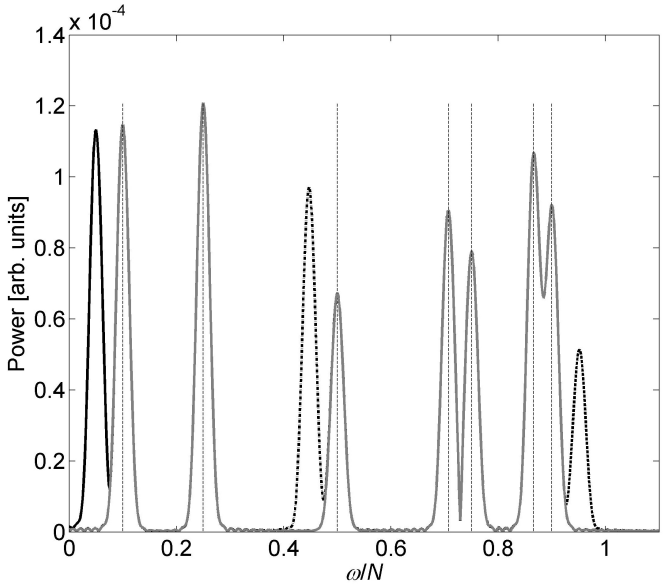

Figure 2.8: FFT outputs with additional frequencies. The grey line represents the original frequency spectrum. The narrow vertical dashed lines represent the generating frequencies from § 2.3.1. The solid black line, dashed black line, and dot-dash black line represent the spectra with an additional low, high, and intermediate frequency, respectively. Zero-padding and a Gauss window are used here.

forcing frequencies are densely spaced is now considered. A flow field consisting of the frequencies corresponding to angles of $40.0° : 0.25° : 50.00°$ from the vertical is generated. These frequencies are referred to as the "resolved frequencies" for the remainder of this discussion. For simplicity, a constant tidal excursion $\chi = \delta/a = 0.0275$ is used for each frequency. Examining 4500 s of data at 4 Hz is sufficient to resolve each quarter-degree peak in the FFT output.

Using the resolved frequencies, the mode strength magnitudes, $|\gamma_{jn}|$, for each forcing frequency are then calculated (figure 2.10). Whereas the nature of the modal decomposition for each frequency changes (particularly as the topography varies from sub- to supercritical), the variation occurs fairly gradually. More importantly, figure 2.10 indicates that the modal decomposition algorithm of § 2.3 can successfully recover the correct values for γ_{jn} even with many more forcing frequencies present. This is seen as a positive first step towards being

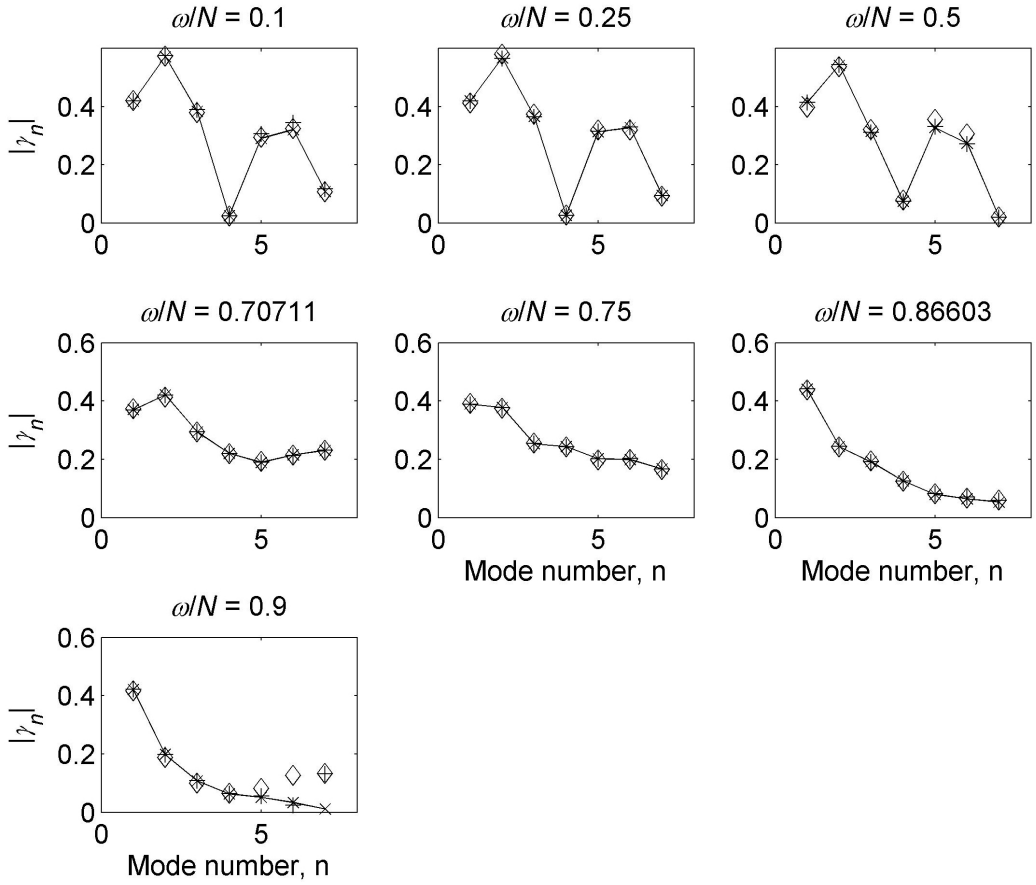

Figure 2.9: Mode strength magnitudes with additional frequencies. Mode strengths corresponding to the wave field with an additional low frequency, high frequency, and intermediate frequency are denoted by $+$, $\times$, and $\diamond$, respectively. For the majority of the points, the symbols overlap. The solid black lines represent the mode strengths from the synthetic data itself. All mode strengths shown here are calculated using the generating frequencies, however, similar results were found when using the frequencies returned by the FFT analysis.

able to adequately "bin" a continuous frequency spectrum in order to estimate mode strengths in instances where, for example, internal waves are generated by fluid-fluid rather than solid-fluid interactions. This idea is discussed in further detail in § 2.5.3 and § 2.5.3.

2.4.2 Unresolved frequencies above or below the main frequency range

A further problem investigated for the case of many densely spaced forcing frequencies is, much like the discussion of § 2.3.2, the impact of unresolved frequencies outside of the frequency range being considered. Thus, additional frequencies corresponding to 4.5° bands (spaced at intervals of 0.5°) are included in the vertical velocity field, as shown in figure 2.11. For $40° \leq \Theta \leq 50°$, there is close agreement between the spectra of the wave fields with and without additional frequency data (figure 2.11, inset).

The calculated mode strengths corresponding to the resolved frequencies (from $\Theta = 40°$ to $\Theta = 50°$) are indicated in figure 2.12. Notwithstanding the prominence of unresolved frequencies in figure 2.11 but consistent with the discussion of § 2.3.2, the presence of additional frequencies outside of the range for which the mode strengths were being calculated appears to have very little effect on the values of γ_{jn} recovered using the algorithm of § 2.2.2. Possible explanations for this counterintuitive result are examined in the following section.

2.5 Further considerations

2.5.1 Errors from neglected frequencies

In order to understand why the neglected frequencies seem to have negligible influence, the theoretical error that arises from ignoring this spectral contribution must be considered. For the case in which all but one frequency ω_k is omitted in the formulation of the matrix equation $A\boldsymbol{\Upsilon} = \mathbf{b}$ (i.e. mode strengths

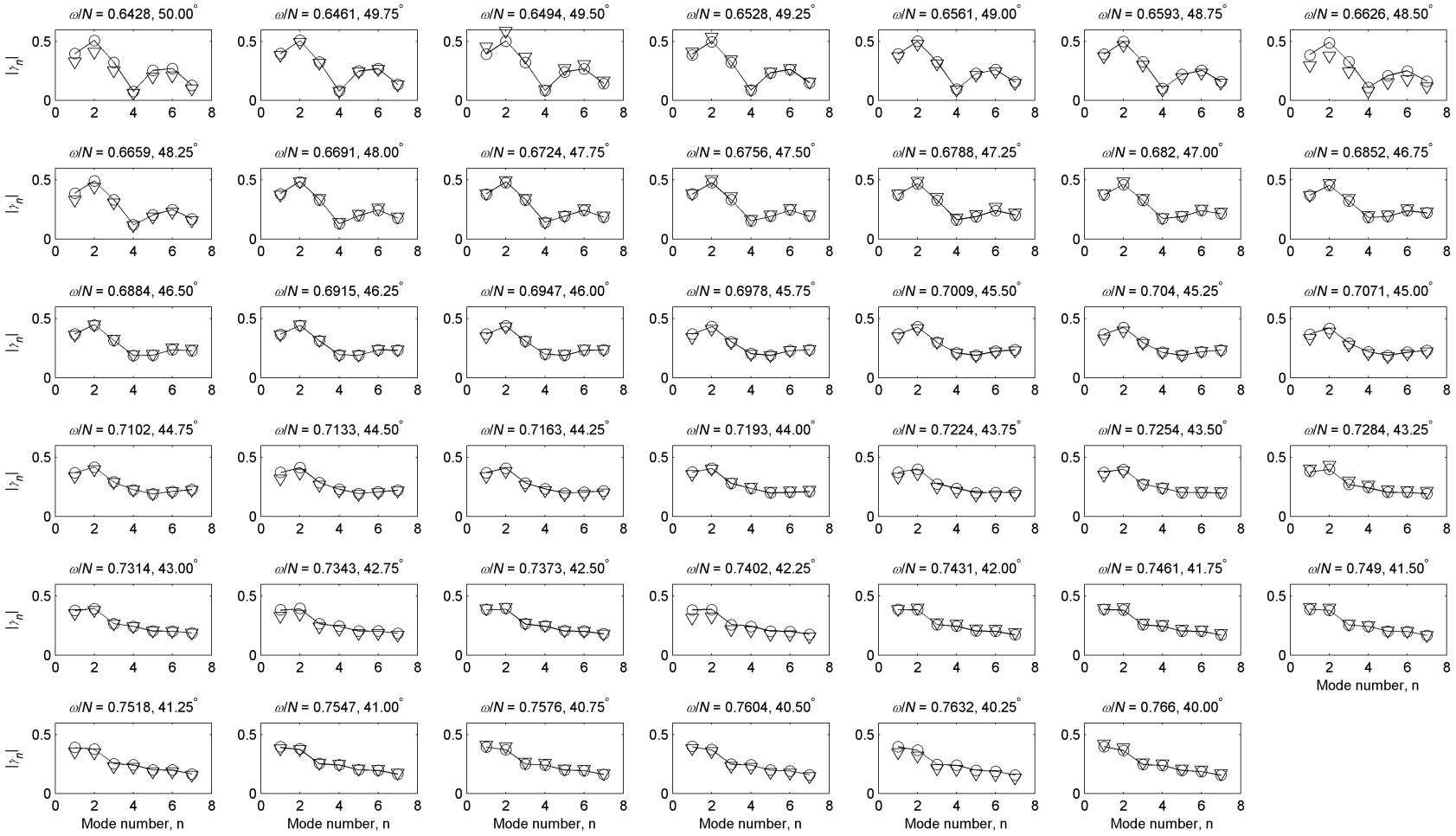

Figure 2.10: Mode strength magnitudes for a flow field consisting of forcing frequencies corresponding to $\Theta = 40.00°$ to $50.00°$, with frequencies spaced at intervals of $0.25°$. Triangles represent mode strengths calculated with the frequencies from FFT, while circles represent mode strengths calculated with the generating frequencies. Solid lines represent the mode strengths from the synthetic data itself.

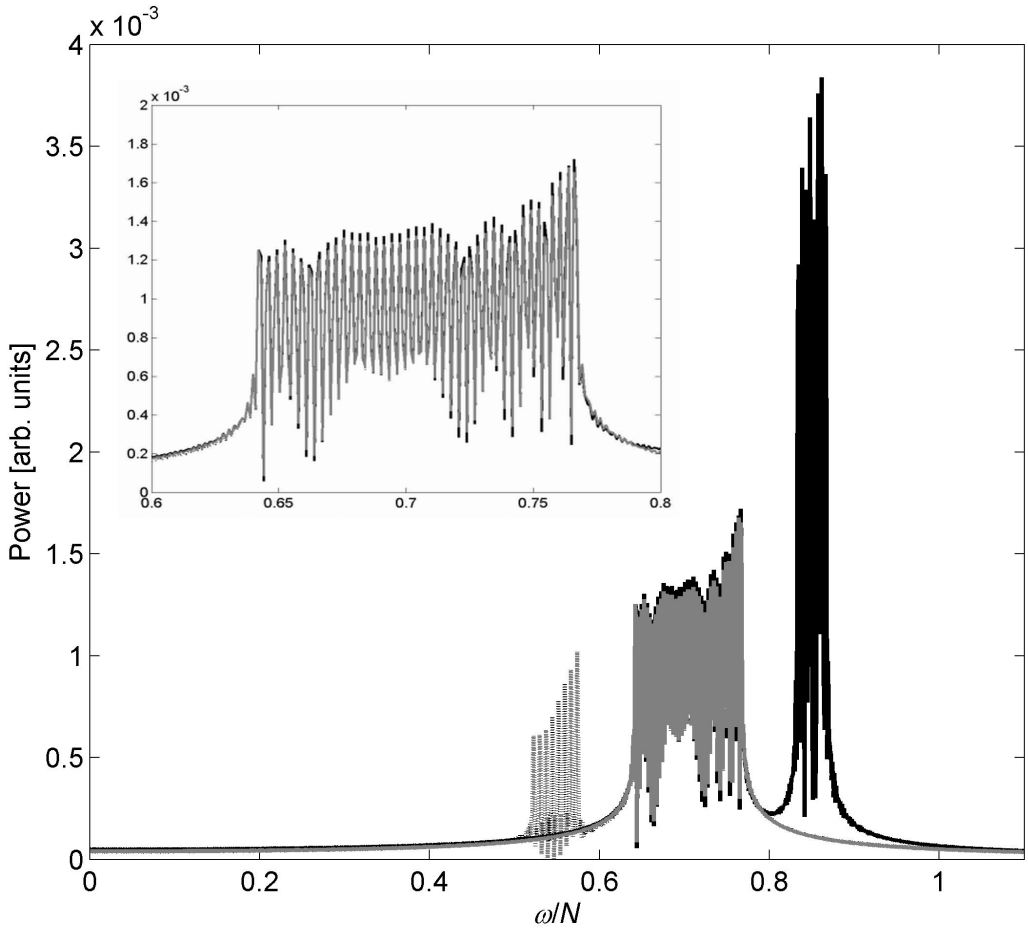

Figure 2.11: FFT output for wave fields with additional frequencies either above or below the primary range being considered. Here, the solid black line and dashed black line represent the power spectra for wave fields in which frequencies corresponding to angles ranging from $\Theta = 30°$ to $34°$ (from the vertical) and $\Theta = 55°$ to $59°$, respectively, are included. The grey line represents the power spectrum of a wave field in which only the frequencies between $\Theta = 40.00°$ and $\Theta = 50.00°$ are present. (For greater clarity, this latter frequency range is reproduced in the inset).

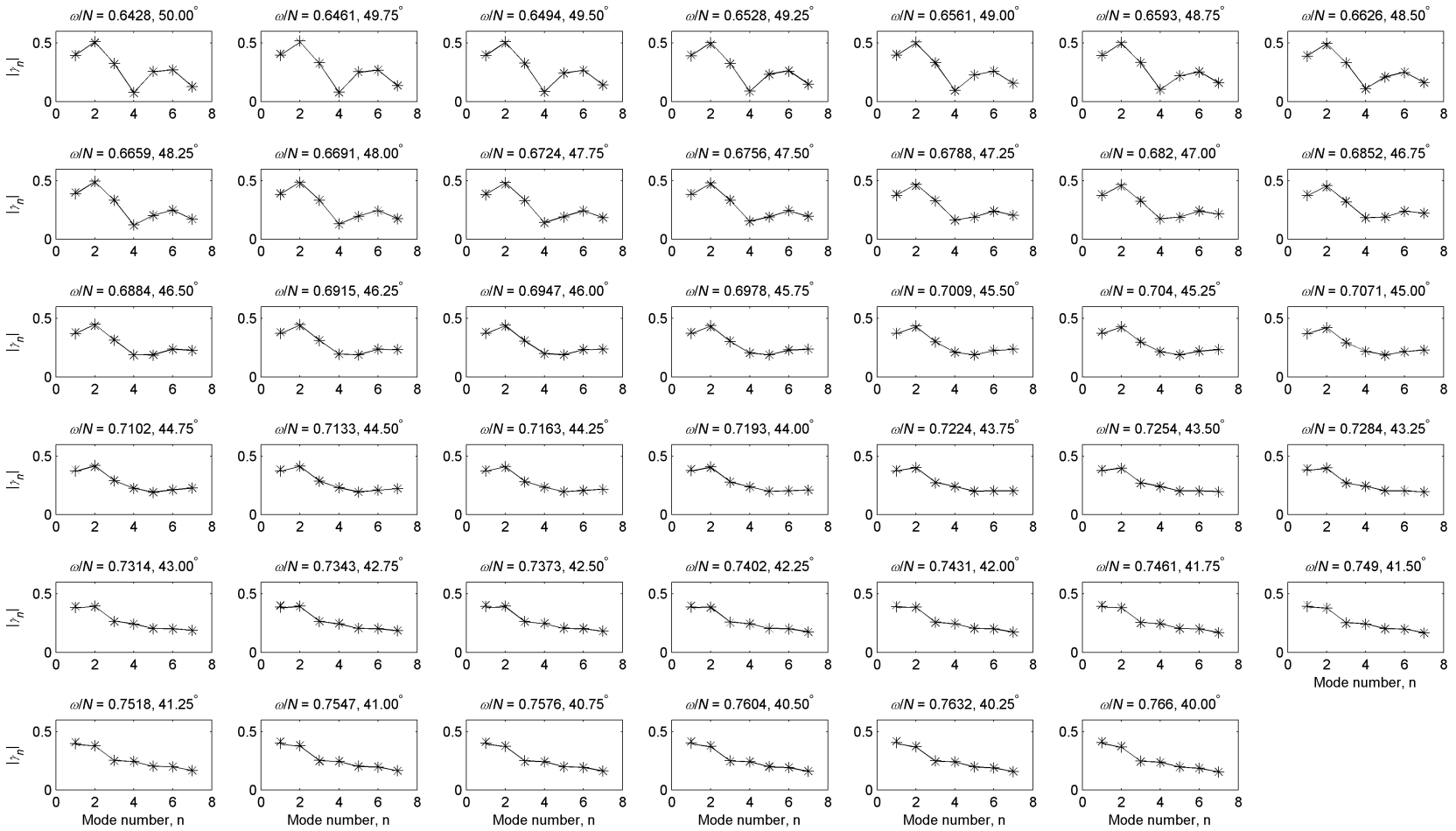

Figure 2.12: Mode strength magnitudes corresponding to $\Theta = 40.00°$ to $\Theta = 50.00°$ with additional frequencies above or below. Mode strength magnitudes corresponding to the wave field with additional low frequencies ($\Theta = 55°$ to $59°$ from vertical) are denoted by $+$, while mode strengths corresponding to the wave field with additional high frequencies ($\Theta = 30°$ to $34°$ from vertical) are denoted by $\times$. For the majority of the points, the symbols overlap. The solid black lines represent the mode strengths from the synthetic data itself. Consistent with figure 2.9, all mode strengths shown here are calculated using the generating frequencies.

are calculated for a single frequency only and A is of dimension 2×2), estimates of the associated error can be derived as follows. Let $\boldsymbol{\Upsilon}^*$ and $\mathbf{b}^*$ be the corresponding vectors from (2.18) and (2.19) calculated with this single frequency, ω_k. The errors $\boldsymbol{\Delta\Upsilon} = \boldsymbol{\Upsilon}^* - \boldsymbol{\Upsilon}$ and $\boldsymbol{\Delta b} = \mathbf{b}^* - \mathbf{b}$ can then be defined. With some algebraic manipulation of (2.14), (2.17), and (2.18), the matrix equation $\boldsymbol{\Delta\Upsilon} = A^{-1}\boldsymbol{\Delta b}$ is found, where

$$A^{-1} = \frac{\bowtie_{kn}}{|A|} \begin{bmatrix} \frac{T\cos\varphi_k}{2} + \frac{\sin(\varphi_k - 2\omega_k T) - \sin\varphi_k}{4\omega_k} & \frac{T\sin\varphi_k}{2} + \frac{\cos(\varphi_k - 2\omega_k T) - \cos\varphi_k}{4\omega_k} \\ \frac{-T\sin\varphi_k}{2} + \frac{\cos(\varphi_k - 2\omega_k T) - \cos\varphi_k}{4\omega_k} & \frac{T\cos\varphi_k}{2} - \frac{\sin(\varphi_k - 2\omega_k T) - \sin\varphi_k}{4\omega_k} \end{bmatrix} \tag{2.27}$$

in which

$$|A| = \bowtie_{kn}^2 \left(\frac{T^2}{4} + \frac{\cos 2\omega_k T - 1}{8\omega_k^2} \right) , \tag{2.28}$$

$$\boldsymbol{\Delta b} = \begin{bmatrix} \sum_{j=0, j\neq k}^{J} -\operatorname{Im}\left\{ \xi_{jkn} \left[\omega_j \cos\omega_k T + \mathrm{i}\omega_k \sin\omega_k T - \omega_j \mathrm{e}^{\mathrm{i}\omega_j T} \right] \right\} \\ \sum_{j=0, j\neq k}^{J} \operatorname{Re}\left\{ \xi_{jkn} \left[\omega_k \cos\omega_k T + \mathrm{i}\omega_j \sin\omega_k T - \omega_k \mathrm{e}^{\mathrm{i}\omega_j T} \right] \right\} \end{bmatrix} \tag{2.29}$$

where

$$\xi_{jkn} = \frac{\bowtie_{jn} \Upsilon_{jn} \mathrm{e}^{\mathrm{i}(\varphi_j - \omega_j T)}}{\omega_j^2 - \omega_k^2} , \tag{2.30}$$

and

$$\boldsymbol{\Delta\Upsilon} = \begin{bmatrix} \Delta\Upsilon_{jnR} \\ \Delta\Upsilon_{jnI} \end{bmatrix} . \tag{2.31}$$

Of note is the impact of the length of the timeseries, T, on the magnitude of the calculated error. The presence of T^2 in (2.28) (and $|A|^{-1}$ in equation 2.27) shows that an increase in the value of T will lead to a greater than linear decrease in the values of $\Delta\Upsilon_{jnR}$ and $\Delta\Upsilon_{jnI}$. In the case of the synthetic data considered here, neglected frequencies such as those discussed in § 2.3.2 and § 2.4.2 do not have a large impact on the calculated mode strengths because of the sufficiently large time periods being considered. Conversely, in the case of experimental data in which T may be much smaller (on the order of 10-60 s), these additional frequencies cannot be ignored. When T is relatively small, it is thus necessary

to resolve all forcing frequencies. However, this may be difficult to achieve if frequencies are closely-packed together in light of (2.24), in which case one needs to carefully apply (2.27), (2.29), and (2.31) to estimate the associated errors.

2.5.2 Bandpass filters for isolation of frequency components

An alternative approach to solving the $2(J+1)$ by $2(J+1)$ matrix equation described in § 2.2.2 is to instead isolate individual frequency components through the use of bandpass filters. In doing so, a filtered polychromatic wave field could be treated as being comprised of only a single frequency, and the theory of Echeverri et al. [2009] could be employed directly.

In order to isolate a specific frequency, a Butterworth bandpass filter is considered. This filter is chosen for its maximally flat passband and stopband. The tradeoff for obtaining such attractive behaviour in the pass- and stopbands is a wider transition band relative to other similar bandpass filters [Mandal and Asif, 2007]. By using the built-in MATLAB Butterworth filter design function, the filter order, passband width, and desired frequency at the center of the passband can be varied for a given data set.

Isolation of individual frequency components from a sparse discrete-frequency wave field can give good qualitative results when comparing the filtered timeseries data with reference timeseries data containing only the associated desired frequency. For example, the filtered wave field shown in figure 2.13 shows good qualitative agreement when compared with a reference wave field, especially away from the lower and upper limits of the timeseries. Note, however, that the application of the filter leads to a change in the magnitudes of the vertical velocities observed, thus necessitating the use of normalized mode strength ratios in the process of mode recovery.

On the basis of this qualitative comparison, one might expect to see corre-

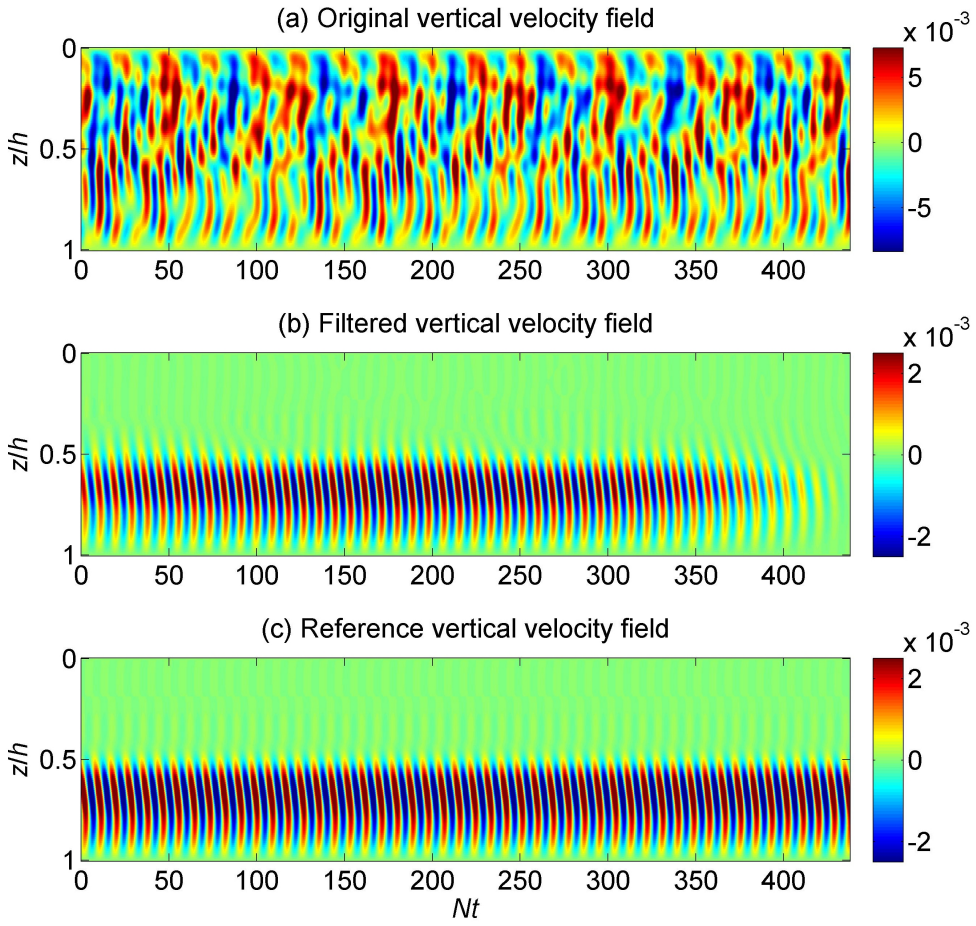

Figure 2.13: Comparison of a filtered wave field with a reference wave field. (a) The original nondimensional vertical velocity field, forced by the same frequencies as in figure 2.4, for $NT = 438$. (b) The resulting wave field after applying a first-order Butterworth bandpass filter to the data in (a). The passband used has a width of $0.02N$ and is centered at $\omega/N = 1/\sqrt{2}$. (c) A reference nondimensional vertical velocity field generated with only the forcing frequency $\omega/N = 1/\sqrt{2}$ for $NT = 438$.

spondingly positive agreement between the recovered and input mode strengths when considering a bandpass filtered wave field. This assumption is true for sufficiently large NT: panel (a) of figure 2.14 shows that the discrepancies in the mode strengths calculated with either the filtering approach or the full 14×14 matrix equation based on the theory of § 2.2.2 are quite small in the case of the $NT = 438$ timeseries. However, when the timeseries length is reduced, panel (b) indicates that larger errors are seen in the calculated mode ratios from the filtered wave field, and these mode ratios begin to deviate from the overall trend given by the synthetic data. This occurs due to the behaviour of filters with short timeseries: in general, for shorter timeseries, filters display increasingly non-ideal behaviour in the form of wider transition bands, for instance [Mandal and Asif, 2007]. Because the Butterworth filter already exhibits wide transition bands, this can lead to especially poor filtering of unwanted frequency components from the wave field. Unfortunately, related filters with narrower transition bands, such as the Chebyshev or elliptic bandpass filters, are not without problems of their own when considering shorter timeseries, because higher ripples in pass- and stopbands are observed with shorter data sets [Mandal and Asif, 2007].

Therefore, in the scenario in which the timeseries being considered is comparatively short, mode strength ratios are more accurately determined if explicit account is made of the other frequency components present in the wave field. Additionally, in using the algorithm of § 2.2.2, the actual mode strengths γ_{jn} can be calculated, rather than the ratios $\gamma_{jn}/|\gamma_{j1}|$. Finally, it should be noted that the results presented above consider several broadly-spaced frequencies. When examining densely-spaced frequencies like those discussed in § 2.4, the accuracy of the mode strengths calculated from a filtered wave field would be no better, and possibly significantly worse, for short timeseries.

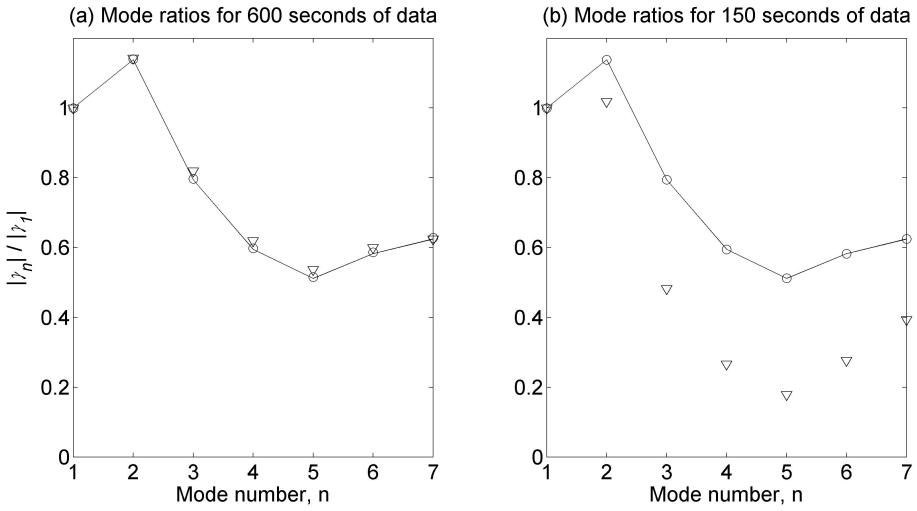

Figure 2.14: Comparison of mode strength ratios, corresponding to the forcing frequency $\omega/N = 1/\sqrt{2}$, calculated using the multiple frequency matrix equation (§ 2.2.2) with those calculated from a filtered wave field (§ 2.5.2). (a) Mode strength ratios for $NT = 438$ (600 s of data). Here, the circles represent the mode ratios calculated with a full 14×14 matrix equation (all frequencies resolved), while the triangles represent those calculated from a wave field after filtering with a Butterworth bandpass filter. (b) As above, but for $NT = 109.5$ (150 s of data).

2.5.3 Continuous frequency spectrum

In many instances of geophysical relevance, the frequency spectrum associated with the generation of internal waves does not consist of discrete forcing frequencies, but rather a continuous frequency spectrum. Such is the case when internal waves are generated by fluid-fluid interactions; there are many papers on this topic as evidenced by the long list of references in Flynn and Sutherland [2004]. As such, it is desirable to be able to perform a modal decomposition of a frequency continuum. Furthermore, following from the discussion of § 2.3.1 and Harris [1978], for short time scales, discrete forcing frequencies may be insufficiently resolved and thus a frequency spectrum composed of discrete forcing frequencies may in fact appear continuous in Fourier space. In either circumstance, it is necessary as in § 2.4.2 to consider the effects of unresolved interstitial frequencies – that is, frequencies within the range being considered for which

the FFT is unable to resolve a clearly defined peak.

Frequency spacing in the A matrix

In order to construct the matrix equation $A\boldsymbol{\Upsilon} = \mathbf{b}$, it is necessary to recover discrete frequencies from the frequency spectrum. This can be thought of as sampling individual frequencies from the continuous frequency spectrum. As illustrated by figure 2.10, the mode strengths evolve slowly with small changes in Θ, even when transitioning from a subcritical to a supercritical wave field. Thus, the modal decomposition associated with a given frequency can be considered to be representative of the neighbouring unresolved interstitial frequency components provided the frequency spacing, $\Delta\omega$, is not too broad. Nor, however, can $\Delta\omega$ be chosen to be too small: from (2.22) and more specifically the factor $\omega_b - \omega_c$ appearing in the denominators, poorly conditioned matrices will arise as $\omega_b \to \omega_c$.

By considering the condition number of the A matrix, the minimum frequency spacing $\Delta\omega_{\min}$ is found to be

$$\Delta\omega_{\min} = 2\pi/T\,. \tag{2.32}$$

This value corresponds to the minimum frequency spacing along the power spectrum given by FFT [Harris, 1978], when zero-padding is not employed.

Values of the condition number for mode 1 corresponding to $40^\circ \leq \Theta \leq 50^\circ$ are shown in table 2.1. When $\Delta\omega \geq \Delta\omega_{\min}$, A is well-conditioned and thus the matrix inversion does not lead to large errors in the solution of $A\boldsymbol{\Upsilon} = \mathbf{b}$. Recall that the data of table 2.1 are based on synthetic laboratory data for which T can be made arbitrarily large; thus the condition $\Delta\omega \geq \Delta\omega_{\min}$ is not especially restrictive. In circumstances where NT cannot be made to be large such as when examining real laboratory data, A may become very ill-conditioned when the frequency spacing is too small relative to $\Delta\omega_{\min}$. Coarse frequency

Table 2.1: Condition numbers vs. $\Delta\omega$ for the A matrix calculated for mode 1 with Θ ranging from 40° to 50°.

T	$\Delta\omega = 0.5\Delta\omega_{\min}$	$\Delta\omega = 0.75\Delta\omega_{\min}$	$\Delta\omega = \Delta\omega_{\min}$	$\Delta\omega = 2\Delta\omega_{\min}$
100	20.2309	2.1129	1.4608	1.0170
600	667633	1417	1.6500	1.6488
1000	33812007	1740121	1.6827	1.6823
1500	606956230	4164321	1.6707	1.6294
3000	621358538	33175049	1.6707	1.6712

spacing may then be required. However, because the modal decomposition associated with each forcing frequency may change appreciably between sampled frequencies (compare, for instance, the mode strength profiles corresponding to $\Theta = 40°$ and $\Theta = 50°$ in figure 2.10), the resulting modal decomposition may not be representative of some or all of the neighbouring unresolved interstitial frequencies.

Frequency recovery

Expanding on the results of table 2.1, an approximation of a continuous frequency spectrum is created using the same method as outlined in § 2.4. Synthetic data are generated at frequencies corresponding to the $40.00° \leq \Theta \leq 50.00°$ range, with constant excursion of $\chi = 0.0275$. Unlike before, the frequency spacing is chosen to be 0.05°. At this frequency spacing, 4500 s of data is insufficient to resolve all of the frequencies present in the wave field. Snapshots of the wave field at four different times are shown in figure 2.15. As expected, rather than seeing sharply defined internal wave beams, the wave field now appears more diffuse about $\Theta = 45°$. A vertical time series of w corresponding to the location of the vertical black lines of figure 2.15 is presented in figure 2.16. Of note here is that due to constructive and destructive interference, the wave field intermittently exhibits large amplitude motions for a relatively short interval of time, seen for small values of $|Nt|$ in figure 2.16, followed by long periods

of very small amplitudes.

The frequency spectrum of the vertical velocity field is found with the FFT routine, and results are shown in figure 2.17. In this case, no window function is applied to the data; as such, some spectral leakage is expected. Consistent with earlier remarks and in contrast to the frequency spectra of figures 2.8 and 2.11, each forcing frequency is no longer individually resolved. However, the frequency spectrum obtained via the FFT still gives an indication of the most energetic frequencies in a particular wave field.

Mode recovery

Using the frequencies corresponding to $\Theta = 40.00^\circ : 0.25^\circ : 50.00^\circ$ in constructing the matrix equations $A\boldsymbol{\Upsilon} = \mathbf{b}$, a set of mode strength ratios are found, as shown in figure 2.18. (This frequency spacing is larger than the corresponding value of $\Delta\omega_{\min} = 0.0014\,\text{rad/s}$ as defined by (2.32).) For this data set, sampled from $-T/2$ to $T/2$, there is good agreement between the calculated and theoretical mode strength ratios. (Further explanation of this choice of sampling interval as compared to the more conventional interval 0 to T is found in Appendix 2.B.) Note, however, that owing to the presence of the unresolved interstitial frequencies in the frequency spectrum, the magnitudes of the entries in the $\mathbf{b}$ column vector (as defined by equation 2.18) are substantially increased. This leads to errors in the magnitudes of γ_{jn} calculated using matrix inversion, and thus necessitates the use of the normalized mode strength ratios, rather than mode strengths themselves, in figure 2.18.

It is also important to emphasize that the above discussion relies heavily on the fact that the synthetic data in question is generated for arbitrarily large values of the timeseries length NT. In this scenario, and following the discussion of § 2.5.1 and § 2.5.3, not only is the error associated with ignoring the additional interstitial frequencies small, but the spectrum can also be sampled with a fine

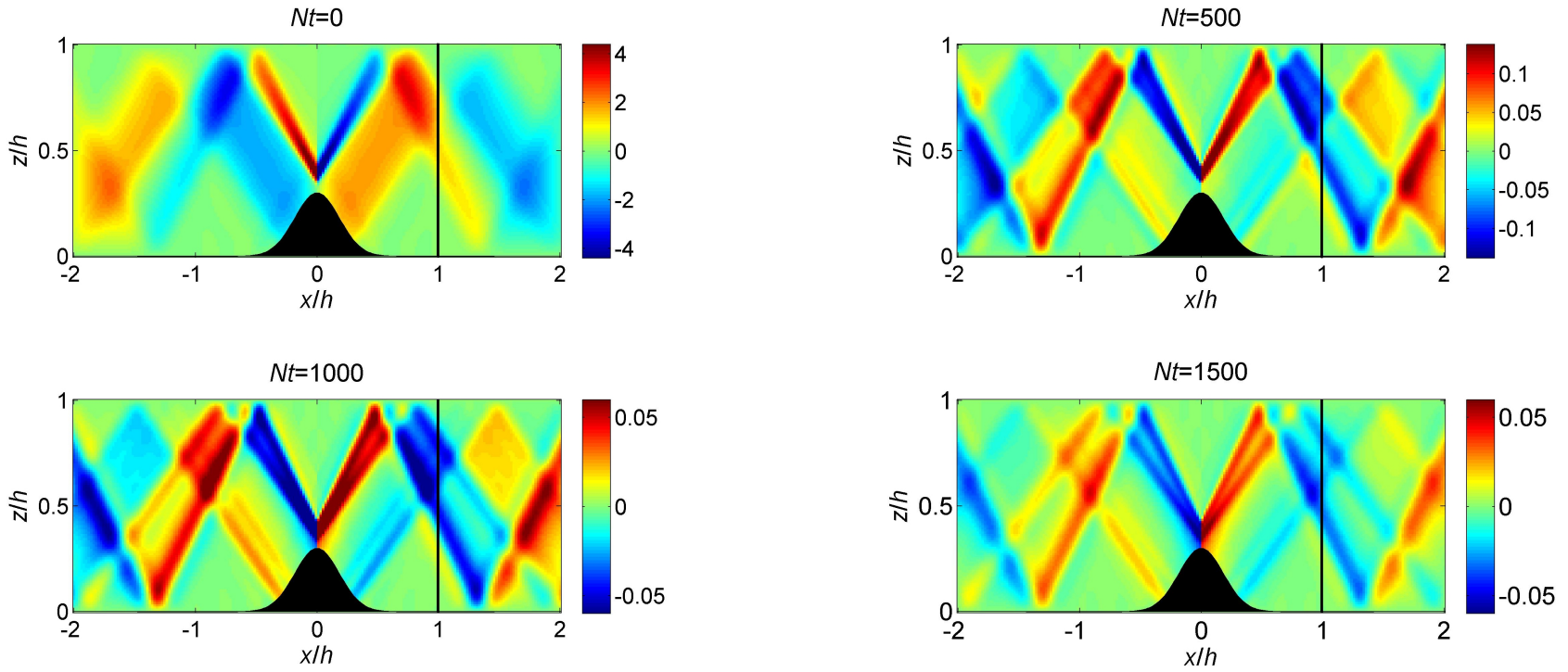

Figure 2.15: Nondimensional vertical velocities at four times for frequencies corresponding to a "continuum" from $\Theta = 40.00°$ to $\Theta = 50.00°$. Note that the colourbar limits vary from one panel to the next.

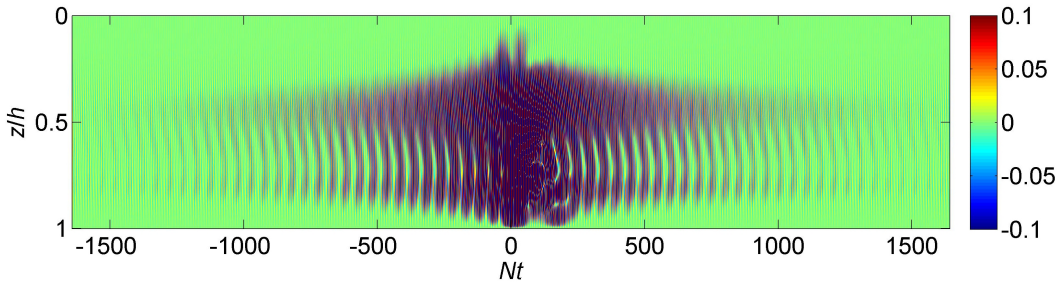

Figure 2.16: Nondimensional vertical velocity field at $x/h = 1$ for $-NT/2 = -1642.5$ (-2250 s) to $NT/2 = 1642.5$ (2250 s) with frequencies corresponding to $\Theta = 40.00°$ to $\Theta = 50.00°$. The colourbar limits have been set to ± 0.1; the vertical velocities saturate the colourbar limits for small values of $|Nt|$.

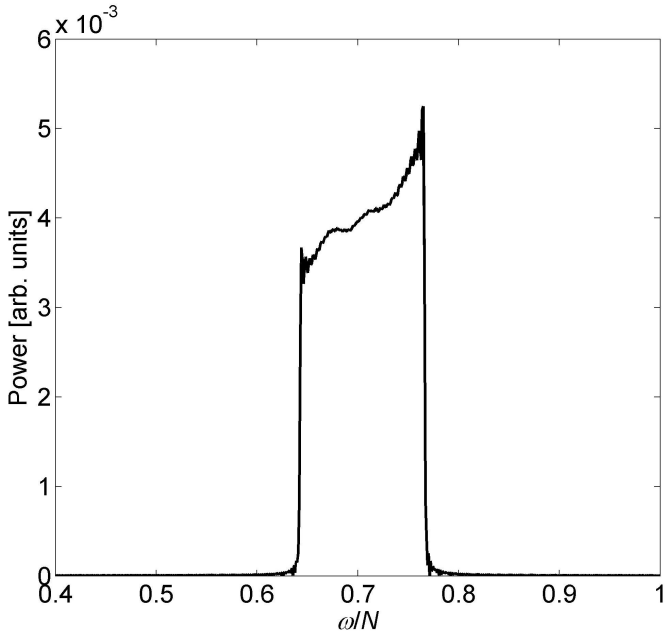

Figure 2.17: Frequency spectrum for a band of frequencies corresponding to internal waves with angles of $\Theta = 40.00°$ to $\Theta = 50.00°$. The data are sampled from $-NT/2 = -1642.5$ (-2250 s) to $NT/2 = 1642.5$ (2250 s). No window is applied to the associated timeseries data.

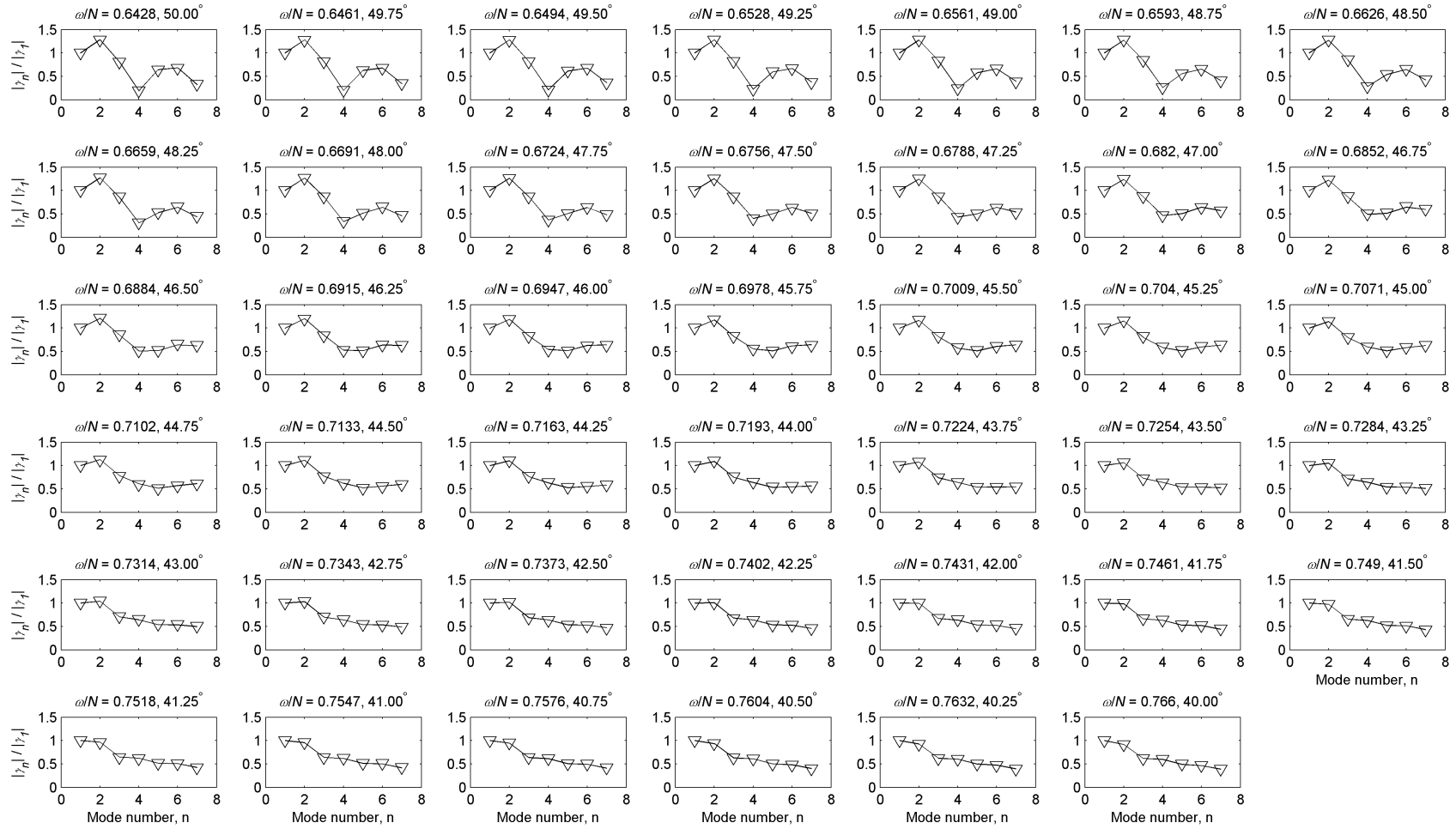

Figure 2.18: Mode strength ratios calculated using generating frequencies for the scenario of unresolved interstitial frequencies. Frequencies used correspond to wave angles of $\Theta = 40.00° : 0.25° : 50.00°$. The triangles correspond to a wave field sampled from $-NT/2 = -1642.5$ (-2250 s) to $NT/2 = 1642.5$ (2250 s).

frequency spacing. When considering experimental flows, however, e.g. in the context of a lock-released gravity current propagating through a continuously stratified ambient [Flynn and Sutherland, 2004], one does not have the luxury of sampling for arbitrarily long time intervals. In fact, such flows have considerably shorter time scales - on the order of 10-60 s (i.e. $NT \simeq 30$). This implies a coarse spacing in Fourier space which results in a great deal of frequency information being ignored in the matrix equation, and thus large errors associated with the unresolved interstitial frequencies.

Additionally, as mentioned in the discussion of § 2.5.2, bandpass filters exhibit more pronounced non-ideal behaviour as NT becomes small, leading to less accurate filtered wave fields with such short timeseries lengths. Attempting to calculate normalized mode ratios by bandpass filtering experimental data is thus prone to large errors. So, while the approaches of § 2.2.2 and § 2.5.2 can be used to analyze long timeseries of observational data with continuous frequency spectra, further developments are necessary for application to most data sets collected in the laboratory.

Whereas such difficulties are anticipated for experimental scales, it should be noted that for moored observations, timeseries lengths may be on the order of weeks [Boyd et al., 2002]. In this scenario, the product NT may be on the order of hundreds or thousands, implying fine frequency spacing in the A matrix and reduced impact of unresolved frequencies.

2.6 Discussion and conclusions

The problem of the modal decomposition of an internal wave field forced by multiple forcing frequencies interacting with ocean-floor topography has been considered. Unlike previous studies [Balmforth et al., 2002; Llewellyn Smith and Young, 2003; Pétrélis et al., 2006; Echeverri et al., 2009; Balmforth and Peacock, 2009; Echeverri and Peacock, 2010] in which the mode strengths of

the wave field are calculated from the shape of the generating topography, the inverse problem is considered here. Using velocity timeseries data (generated by adapting the theory of Pétrélis et al. [2006]), the frequency information and mode strengths of the wave field are calculated, without specific reference to the topographic profile. This modal decomposition algorithm can be applied to both laboratory and oceanographic length scales (see also Chapter 3).

If unknown, the frequency information present in the wave field is found using a fast Fourier transform (FFT) routine, which leverages zero-padding and windowing. In the case of a frequency spectrum consisting only of discrete forcing frequencies, if the tidal excursion values δ_j corresponding to the forcing frequencies ω_j are known, then the mode strength magnitudes $|\gamma_{jn}|$ can be found to good precision using the system of equations described by (2.17), (2.18), and (2.19). In the scenario in which the tidal excursions are unknown, the mode strengths are more difficult to determine. However, the product $\delta_j\gamma_{jn}$ can be straightforwardly found and likewise the ratio $|\gamma_{jn}|/|\gamma_{j1}|$. The resulting mode strengths may be sensitive to errors in the frequencies recovered via FFT; however, very good qualitative and quantitative agreement is found even when errors exist in the recovered frequencies.

In examining the details of the associated algorithm, it has been shown that the error arising from neglected frequencies decreases with increasing timeseries length NT, i.e. for longer timeseries, less error is incurred by ignoring some of the frequency information present, as expressed by (2.27) and (2.29). This missing information may correspond to a frequency or frequencies either inside or outside of the range of frequencies included in the matrix equation. A further benefit of long timeseries is that they allow one to examine a finer range of frequencies – see (2.24).

As a result, in extending the modal decomposition algorithm to the scenario in which the frequency spectrum is continuous, the effect of timeseries length

plays an important role. For synthetic data, in which NT can be made arbitrarily large, excellent quantitative agreement is found between the recovered scaled mode strength magnitudes $|\gamma_{jn}|/|\gamma_{j1}|$ and those used in generating the synthetic data. However, as T is decreased, the impact on both the allowable spacing of recovered frequencies used to construct the matrix equation $A\boldsymbol{\Upsilon} = \mathbf{b}$ and the errors from the neglected interstitial frequencies lead to significant errors in the recovered mode strengths.

Further adaptations to this algorithm such as incorporating nonlinear stratifications would allow for consideration of more geophysically relevant scenarios, as the background stratification is generally a strong function of z in the ocean [Pedlosky, 2003]. Such adaptations are pursued in Chapter 3.

2.A Zero-padding

The impact of applying the Gauss window to $NT = 438$ (600 s) of vertical velocity data (as shown in figure 2.4) and the addition of $NT = 1752$ (2400 s) worth of zeroes to the end of the windowed array can be seen in table 2.A.1 and figure 2.A.1. The addition of the zeroes leads to a smoother spectrum with finer frequency resolution [Press, 1988], while the use of the Gauss window reduces the majority of the spectral leakage. The errors in the frequencies found from the FFT output are quantified in table 2.A.1, which gives percent errors for $NT = 438$ (600 s) of data, $NT = 2190$ (3000 s) of data, and $NT = 438$ padded by $NT = 1752$ (2400 s) of zeroes, all for a wave field sampled at 4 Hz and after application of a Gauss window. It is clear that the addition of the zeroes reduces the error in the recovered frequencies to that of the longer set of data.

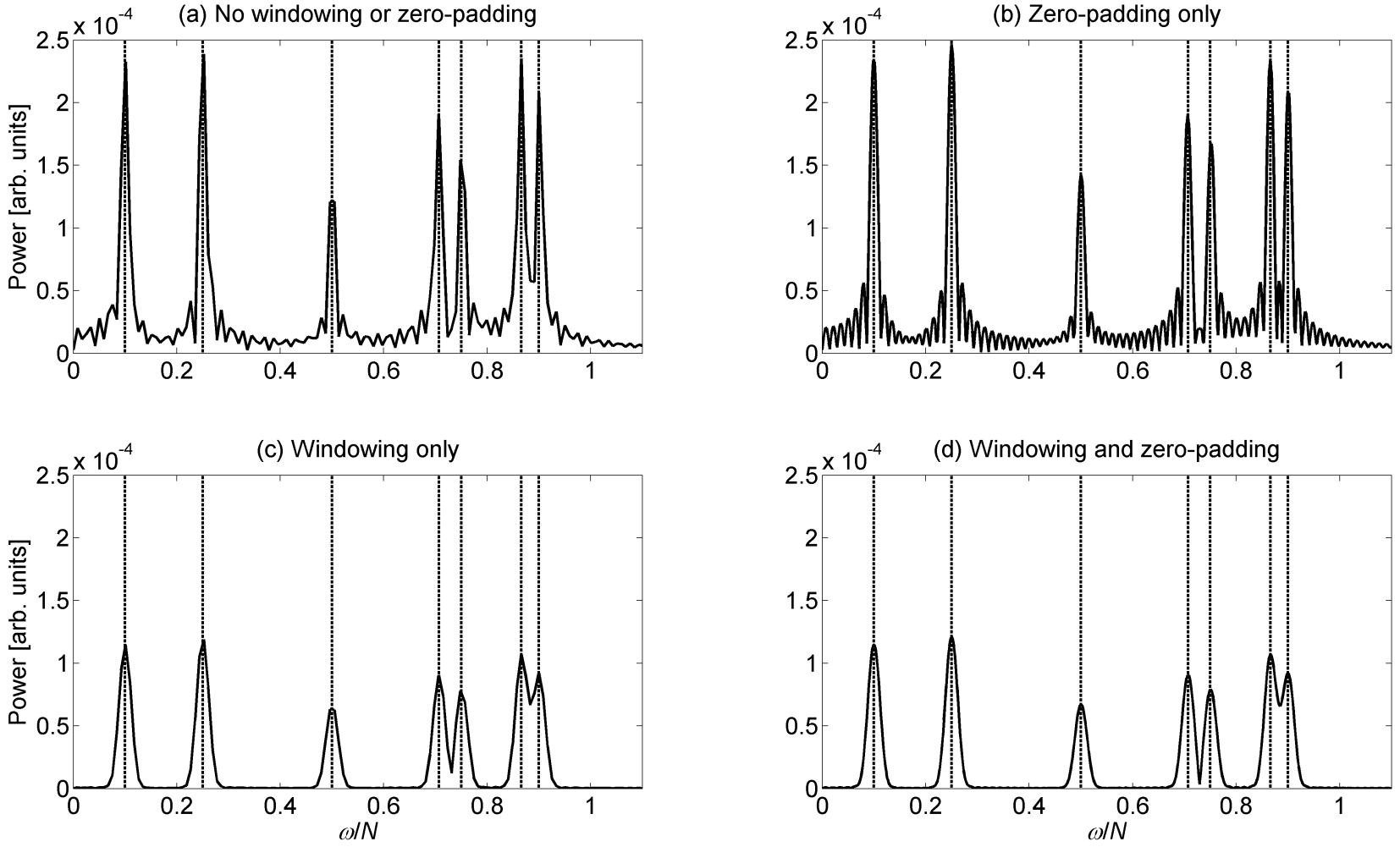

Figure 2.A.1: The effects of zero-padding and windowing on FFT outputs. (a) The frequency power spectrum of the signal. (b) The spectrum after the addition of 2400 s of zeroes. (c) The spectrum after applying a Gauss window. (d) The spectrum with both the Gauss window and addition of 2400 s of zeroes.

Table 2.A.1: Effects of zero-padding on values of ω/N returned by FFT. Here, "$NT = 438$" and "$NT = 2190$" refer to 600 and 3000 s of data, respectively, while "$NT = 438 + 1752$" refers to 600 s of data padded by 2400 s of zeroes.

ω/N	% error ($NT = 438$)	% error ($NT = 2190$)	% error ($NT = 438 + 1752$)
$1/10$	0.959	0.822	0.822
$1/4$	0.932	0.055	0.055
$1/2$	0.767	0.027	0.027
$1/\sqrt{2}$	0.095	0.133	0.133
$3/4$	0.201	0.037	0.037
$\sqrt{3}/2$	0.016	0.016	0.016
$9/10$	0.015	0.061	0.061

2.B Sample windows and frequency spectra

When examining a frequency spectrum in which unresolved interstitial frequencies are present, care must be taken in choosing upper and lower limits of the sampled timeseries data. The frequency spectrum of the velocity field given by figure 2.16 is presented in figure 2.B.1. While the solid line is the same as that given by figure 2.17, the dotted line corresponds to the FFT of data sampled from 0 to $NT = 3285$ ($T = 4500$ s). In this case, the spectrum exhibits significant increases in amplitude at the upper and lower extremities of the frequency band, while this behaviour is largely absent when sampling symmetrically about the origin, i.e. from $-NT/2$ to $NT/2$.

Further investigation indicates that these increases in amplitude are likely due to the fact that sampling only for positive time, as for the spectra shown in figures 2.11 and 2.A.1, is essentially equivalent to multiplying the data by the Heaviside step function in the time domain. This corresponds to a convolution with the Heaviside step function in the frequency domain. While this convolution does not significantly alter the sharp peaks of the frequency spectrum for discrete forcing frequencies, the impact is expected to be nontrivial

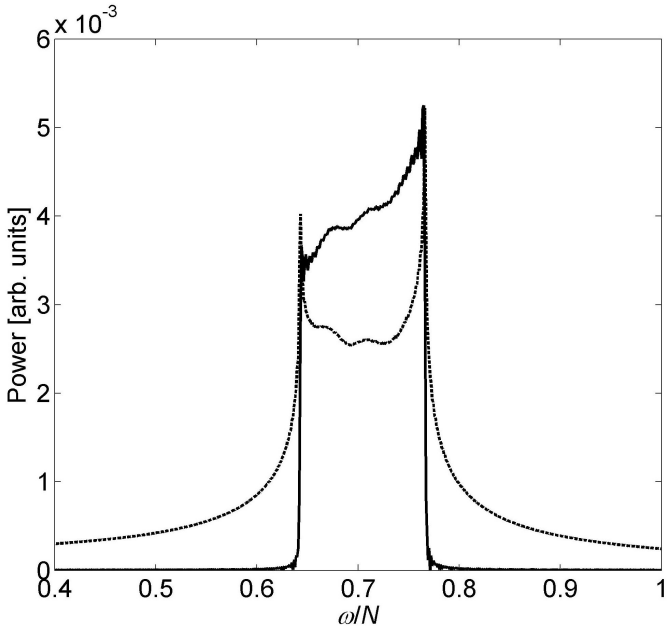

Figure 2.B.1: Frequency spectra corresponding to internal waves with angles of $\Theta = 40.00°$ to $\Theta = 50.00°$. The dashed bold line represents data sampled from $NT = 0$ to 3285 ($T = 4500\,\mathrm{s}$) and the FFT output shows increased side peaks at the edges of the passband. The solid bold line represents data sampled from $NT = -1642.5$ to 1642.5. Over this symmetric time interval, this side peak behaviour is largely absent. No window is applied to the associated timeseries data.

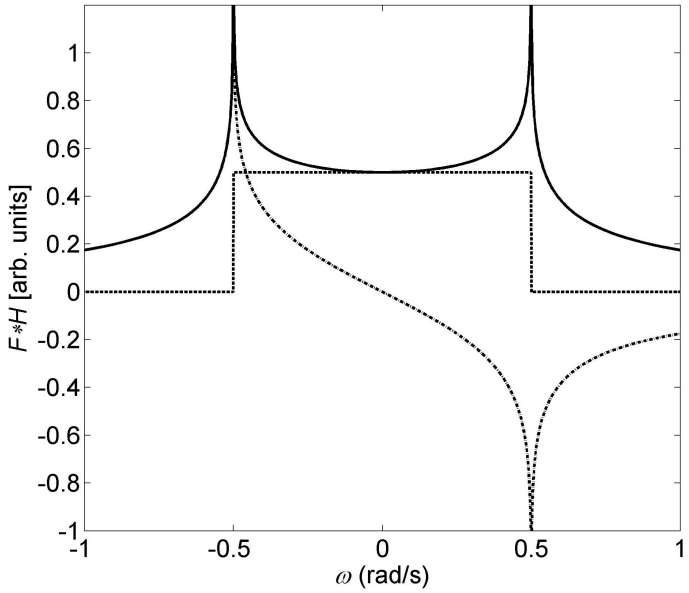

Figure 2.B.2: Results of the convolution of $\operatorname{sinc} t$ with the Heaviside step function. The dashed line represents the real part of (2.B.1), the dot-dashed line represents the imaginary part, and the solid line represents the complex magnitude.

when considering a continuum of frequencies within some interval of Fourier space. Consider, for example, the function $\operatorname{sinc} t$. The Fourier transform is the "tophat" function, $F = \operatorname{rect} \omega$, which is similar to the bandwidth-limited spectrum shown in figure 2.17. The result of the convolution of $\operatorname{sinc} t$ with the Heaviside step function is given by

$$(F * H)(\omega) = \begin{cases} \frac{1}{2} - \frac{\mathrm{i}}{2\pi} \ln \left| \frac{\omega+1/2}{\omega-1/2} \right| & \text{if } \omega < |1/2| \\ -\frac{\mathrm{i}}{2\pi} \ln \left| \frac{\omega+1/2}{\omega-1/2} \right| & \text{if } \omega > |1/2| \\ \mathrm{i}\infty & \text{if } \omega = -1/2 \\ -\mathrm{i}\infty & \text{if } \omega = 1/2 \end{cases} . \tag{2.B.1}$$

When plotted (see figure 2.B.2), (2.B.1) gives similar behaviour on the edges of the band of frequencies as that shown in figure 2.17. Additionally, because $\int_0^\infty |\operatorname{sinc} t|^2 \, \mathrm{d}t = \int_{-\infty}^\infty |(F * H)(\omega)|^2 \, \mathrm{d}\omega = \frac{1}{2}$, Parseval's theorem is satisfied by (2.B.1). In light of these considerations, only the $-T/2 \ldots T/2$ data are considered in § 2.5.3.

Bibliography

M. H. Alford. Redistribution of energy available for ocean mixing by long-range propagation of internal waves. *Nature*, 423:159–163, 2003.

N. J. Balmforth and T. Peacock. Tidal conversion by supercritical topography. *Journal of Physical Oceanography*, 39(8):1965–1974, 2009.

N. J. Balmforth, G. R. Ierley, and W. R. Young. Tidal conversion by subcritical topography. *Journal of Physical Oceanography*, 32(10):2900–2914, 2002.

T. Boyd, M. D. Levine, S. R. Gard, and W. Waldorf. Mooring observations from the Hawaiian Ridge November 2000-January 2001. Technical report, Oregon State University, Corvallis, OR, 2002.

E. Di Lorenzo, W. R. Young, and S. Llewellyn Smith. Numerical and analytical estimates of M_2 tidal conversion at steep oceanic ridges. *Journal of Physical Oceanography*, 36(6):1072–1084, 2006.

P. Echeverri and T. Peacock. Internal tide generation by arbitrary two-dimensional topography. *Journal of Fluid Mechanics*, 659:247–266, 2010.

P. Echeverri, M. R. Flynn, K. B. Winters, and T. Peacock. Low-mode internal tide generation by topography: an experimental and numerical investigation. *Journal of Fluid Mechanics*, 636:91–108, 2009.

G. D. Egbert and R. D. Ray. Semi-diurnal and diurnal tidal dissipation from TOPEX/Poseidon altimetry. *Geophysical Research Letters*, 30(17):1–4, 2003.

M. R. Flynn and B. R. Sutherland. Intrusive gravity currents and internal gravity wave generation in stratified fluid. *Journal of Fluid Mechanics*, 514: 355–383, 2004.

C. Garrett and E. Kunze. Internal tide generation in the deep ocean. *Annual Review of Fluid Mechanics*, 39(1):57–87, 2007.

A. Gilat and V. Subramaniam. *Numerical Methods for Engineers and Scientists: An Introduction with Applications Using MATLAB*. John Wiley & Sons, Inc., Hoboken, NJ, 2008. ISBN 978-0-471-73440-6.

F. Harris. On the use of windows for harmonic analysis with the discrete Fourier transform. *Proceedings of the IEEE*, 66(1):51–83, 1978.

S. R. Jayne, L. C. St. Laurent, and S. T. Gille. Connections between ocean bottom topography and Earth's climate. *Oceanography*, 17(1):65–74, 2004.

E. Kunze and S. G. Llewellyn Smith. The role of small-scale topography in turbulent mixing of the global ocean. *Oceanography*, 17(1):55–64, 2004.

J. Lighthill. *Waves in Fluids*. Cambridge University Press, Cambridge, UK, 1978. ISBN 0-521-29233-6.

S. G. Llewellyn Smith and W. R. Young. Tidal conversion at a very steep ridge. *Journal of Fluid Mechanics*, 495:175–191, 2003.

L. R. M. Maas. Topographies lacking tidal conversion. *Journal of Fluid Mechanics*, 684:5–24, 2011.

M. Mandal and A. Asif. *Continuous and Discrete Time Signals and Systems*. Cambridge University Press, Cambridge, UK, 2007. ISBN 978-0-521-85455-9.

J. Pedlosky. *Waves in the Ocean and Atmosphere: Introduction to Wave Dynamics*. Springer-Verlag, Berlin, 2003. ISBN 3540003401.

F. Pétrélis, S. Llewellyn Smith, and W. R. Young. Tidal conversion at a submarine ridge. *Journal of Physical Oceanography*, 36(6):1053–1071, 2006.

K. L. Polzin, J. M. Toole, J. R. Ledwell, and R. W. Schmitt. Spatial variability of turbulent mixing in the abyssal ocean. *Science*, 276:93–96, 1997.

W. H. Press. *Numerical Recipes in C*. Cambridge University Press, Cambridge, UK, 1988. ISBN 0-521-35465-X.

D. L. Rudnick, T. J. Boyd, R. E. Brainard, G. S. Carter, G. D. Egbert, M. C. Gregg, P. E. Holloway, J. M. Klymak, E. Kunze, C. M. Lee, M. D. Levine, D. S. Luther, J. P. Martin, M. A. Merrifield, J. N. Moum, J. D. Nash, R. Pinkel, L. Rainville, and T. B. Sanford. From tides to mixing along the Hawaiian ridge. *Science*, 301:355–357, 2003.

H. L. Simmons, S. R. Jayne, L. C. St. Laurent, and A. J. Weaver. Tidally driven mixing in a numerical model of the ocean general circulation. *Ocean Modelling*, 6:245–263, 2004.

L. St. Laurent and C. Garrett. The role of internal tides in mixing the deep ocean. *Journal of Physical Oceanography*, 32:2882–2899, 2002.

C. Wunsch and R. Ferrari. Vertical mixing, energy, and the general circulation of the oceans. *Annual Review of Fluid Mechanics*, 36(1):281–314, 2004.

Chapter 3

Nonlinear stratification[1]

3.1 Background

Chapter 2 considers the modal decomposition of a polychromatic internal wave field, i.e. one forced by multiple forcing frequencies. One of the limiting assumptions made in Chapter 2 is that the buoyancy frequency, N, is constant (i.e. the density stratification is linear). In many scenarios, however, the stratification varies with z, the vertical coordinate. Nonlinear stratifications are ubiquitous in the ocean, for example, and show little variability with time in deep water [King et al., 2012].

Often, the Wentzel-Kramers-Brillouin (WKB) approximation is employed as an expeditious means of treating this variable stratification. Here, N is assumed to change slowly relative to the (vertical) length scale of the internal waves, so that locally the wave field behaves much like one for which N is a constant [Gill, 1982; Pedlosky, 2003]. Under this assumption, the vertical structure of the internal waves can then be recovered. More specifically, the WKB approximation has been used in previous analytical investigations as a means of calculating the complex mode strengths associated with a specific generating topography by means of a Green's function approach [Llewellyn Smith and Young, 2003; Echeverri and Peacock, 2010].

[1] A version of this chapter has been submitted for publication. Kaminski and Flynn 2012. *Journal of Geophysical Research – Oceans.*

As in Chapter 2, the principal aim lies not in calculating the mode strengths associated with the wave field based on a particular topographic shape, but rather on recovery of the mode strengths from velocity data of the wave field with no *a-priori* knowledge of the specifics of its generation. Unlike in Chapter 2, however, the modal decomposition algorithm now accounts for nonlinear background stratification ($N = N(z)$); this allows extension of the methodology to still more geophysically relevant scenarios. It should be noted, however, that the wave fields themselves are still linear in the sense of their dynamics, i.e. nonlinear interactions between individual waves are not considered.

This chapter is structured as follows. In § 3.2, the theory relating to internal waves forced in a non-uniform stratification using the WKB approximation is outlined, and modifications to the algorithm of Chapter 2 to allow for variable N are introduced. The modal decomposition algorithm described in § 3.2.2 is then applied in recovering the mode strengths of two synthetic wave fields: the former is generated at laboratory length scales for an exponential stratification (§ 3.3), while the latter considers data at oceanographic scales (§ 3.4). Finally, a series of conclusions and ideas for future research is outlined in § 3.5.

3.2 Theory

3.2.1 Formulation

Assuming a two-dimensional inviscid flow with constant Coriolis frequency, the motion of linear topographically-forced internal waves is governed by the fol-

lowing system of equations:

$$\begin{aligned} u_t - fv + p_x &= 0 \\ v_t + fu &= 0 \\ w_t + p_z - \theta &= 0 \\ \theta_t + N(z)^2 w &= 0 \\ u_x + w_z &= 0 \end{aligned} \tag{3.2.1}$$

where u and w are the horizontal and vertical components, respectively, of in-plane velocity, p is the rescaled pressure, θ is the buoyancy perturbation, and v is the out-of-plane component of velocity. In a geophysical setting, u and v are the zonal and meridional components of velocity.

Following the approach of Llewellyn Smith and Young [2003], Echeverri and Peacock [2010], and others, the WKB approximation is employed to account for this vertically varying background stratification. Thus, for non-hydrostatic waves, the frequency-specific and vertically-integrated variable $\overline{N}_j$ can be defined as

$$\overline{N}_j = \frac{1}{h}\int_0^h \sqrt{N(z')^2 - \omega_j^2}\,\mathrm{d}z' \,. \tag{3.2.2}$$

in which h is the ocean depth and ω_j a forcing frequency. Using $\overline{N}_j$, a nondimensional buoyancy frequency and stretched vertical coordinate are given as

$$\mathcal{N}_j = \frac{1}{\overline{N}_j}\sqrt{N(z)^2 - \omega_j^2} \tag{3.2.3}$$

and

$$Z_j = \frac{\pi}{h\overline{N}_j}\int_0^z \sqrt{N(z')^2 - \omega_j^2}\,\mathrm{d}z' \,, \tag{3.2.4}$$

respectively [Echeverri and Peacock, 2010]. The horizontal coordinate is defined in an analogous way [Llewellyn Smith and Young, 2003; Echeverri and Peacock, 2010], i.e.

$$X_j = \frac{\pi x}{\mu_j h} \tag{3.2.5}$$

where

$$\mu_j = \frac{\overline{N}_j}{\sqrt{\omega_j^2 - f^2}}\,. \tag{3.2.6}$$

The structure of the vertical modes under the WKB approximation can then be written as [Llewellyn Smith and Young, 2003]

$$a_{nj}(z) \approx \frac{\sin nZ_j}{\sqrt{\mathcal{N}_j(z)}}\,. \tag{3.2.7}$$

Setting $N =$ constant in the above expressions yields $\overline{N}_j = \sqrt{N^2 - \omega_j^2}$, $\mathcal{N}_j = 1$, $Z = \pi z/h$, $\mu_j = \sqrt{(N^2 - \omega_j^2)/(\omega_j^2 - f^2)}$, and $a_{nj}(z) = \sin nZ$, thus giving identical expressions to those in Chapter 2 under the assumption of linear stratification.

In deriving time-periodic solutions to (3.2.1), Echeverri and Peacock [2010] define a streamfunction, ψ, such that $u = -\partial\psi/\partial z$, $w = \partial\psi/\partial x$ (thus satisfying the last equation of (3.2.1)), and

$$\psi(x, z, t) = U\text{Real}\{\phi(x, z)\mathrm{e}^{-\mathrm{i}\omega t}\} \tag{3.2.8}$$

where

$$\phi^{\pm}(X, Z) = \frac{h}{\pi}\sum_{m=1}^{\infty}\frac{\gamma_m^{\pm}}{m}\frac{\sin mZ}{\sqrt{\mathcal{N}}}\mathrm{e}^{\pm\mathrm{i}mX}\,. \tag{3.2.9}$$

The $\gamma_m^{\pm}$ in the above expression are the complex mode strengths describing the spatial structure of the wave field, and are sensitive functions of the topographic shape. From equations (3.2.1), (3.2.7), (3.2.8), and (3.2.9), an equation for the far-field vertical velocity, w, can then be found in terms of $\gamma_m^{\pm}$, i.e.

$$w = \begin{cases} \frac{U}{\mu}\text{Real}\left\{\sum_{m=1}^{\infty}\gamma_m\mathrm{e}^{\mathrm{i}(mX-\omega t+\pi/2)}\frac{\sin mZ}{\sqrt{\mathcal{N}(z)}}\right\} & X \geq 0 \\ -\frac{U}{\mu}\text{Real}\left\{\sum_{m=1}^{\infty}\gamma_m\mathrm{e}^{\mathrm{i}(-mX-\omega t+\pi/2)}\frac{\sin mZ}{\sqrt{\mathcal{N}(z)}}\right\} & X < 0 \end{cases}\,. \tag{3.2.10}$$

In examining a polychromatic wave field, the previous expression can be written as a superposition of the vertical velocity contributions from multiple

frequencies ω_j. With some further algebraic manipulation, and including this (linear) superposition, (3.2.10) can then be written as

$$w = \sum_{k=0}^{J} \mathrm{sgn}(X_k) \frac{\delta_k \omega_k}{\mu_k} \left\{ \sum_{m=1}^{\infty} [\gamma_{kmr} \cos(\varphi_{km} - \omega_k t) - \gamma_{kmi} \sin(\varphi_{km} - \omega_k t)] \frac{\sin m Z_k}{\sqrt{\mathcal{N}_k}} \right\} \tag{3.2.11}$$

where

$$\varphi_{km} = |m X_k| + \pi/2 \,, \tag{3.2.12}$$

and the complex mode strengths $\gamma_{km} = \gamma_{kmr} + \mathrm{i}\gamma_{kmi}$ now depend on both the forcing frequency ω_k as well as the topographic shape.

3.2.2 Modal decomposition

In order to determine γ_{jn} when the stratification is z-dependent, the following integral is defined:

$$I_{mnkj} = \sqrt{\overline{N}_j \overline{N}_k} \int_0^h \sin m Z_k \sin n Z_j \sqrt[4]{\frac{(N^2 - \omega_j^2)^3}{N^2 - \omega_k^2}} \, \mathrm{d}z \tag{3.2.13}$$

Because of orthogonality, it is possible to simplify the above expression when $k = j$, i.e. $I_{mnjj} = (h\overline{N}_j^2/2)\, \delta_{mn}$ where δ_{mn} is the Kronecker delta function. Conversely, when $k \neq j$, orthogonality cannot be exploited and (3.2.13) describes instead a diagonally-dominant matrix.

Multiplying the expression for the vertical velocity given by (3.2.11) by

$$\frac{\sin m Z_j}{\sqrt{\mathcal{N}_j}} (N^2 - \omega_j^2) \, \mathrm{sgn}(X_j) \tag{3.2.14}$$

and integrating over the fluid depth yields a parameter β_{jn}, where

$$\begin{aligned} \beta_{jn} &= \int_0^h \frac{w}{\mathrm{sgn}(X_j)} \frac{\sin m Z_j}{\sqrt{\mathcal{N}_j}} (N^2 - \omega_j^2) \, \mathrm{d}z \qquad (3.2.15) \\ &= \sum_{k=0}^{J} \frac{\delta_k \omega_k}{\mu_k} \sum_{m=1}^{\infty} [\gamma_{kmr} \cos(\varphi_{km} - \omega_k t) - \gamma_{kmi} \sin(\varphi_{km} - \omega_k t)] \, I_{mnkj} \,. \end{aligned}$$

A more detailed derivation of the above expression is given in Appendix 3.A. This parameter can be further decomposed as follows:

$$\beta_{jn} = \beta_{jn*} + \varsigma_{jn} \,, \tag{3.2.16}$$

in which

$$\beta_{jn*} = \sum_{k=0}^{J} \frac{\delta_k \omega_k}{\mu_k} [\gamma_{knr} \cos(\varphi_{kn} - \omega_k t) - \gamma_{kni} \sin(\varphi_{kn} - \omega_k t)] \frac{h\overline{N}_j^2}{2} \tag{3.2.17}$$

and

$$\begin{aligned} \varsigma_{jn} \quad = \quad & \sum_{k=0, k\neq j}^{J} \frac{\delta_k \omega_k}{\mu_k} \left\{ \sum_{m=1}^{\infty} [\gamma_{kmr} \cos(\varphi_{km} - \omega_j t) - \gamma_{kmi} \sin(\varphi_{km} - \omega_j t)] I_{mnkj} \right. \\ & \left. - [\gamma_{knr} \cos(\varphi_{kn} - \omega_j t) - \gamma_{kni} \sin(\varphi_{kn} - \omega_j t)] \frac{h\overline{N}_j^2}{2} \right\} . \end{aligned} \tag{3.2.18}$$

Following the discussion of Appendix 3.A, the variables β_{jn*} and ς_{jn} can be thought of as the orthogonal and non-orthogonal components, respectively, of β_{jn}.

As in the constant stratification scenario, the β_{jn} terms can then be mapped onto the basis functions $\cos \omega_k t$ and $\sin \omega_k t$, where $k = 0, 1, ..., J$ correspond to the $J + 1$ frequencies present in the internal wave field. This mapping yields a system of $2(J+1)$ equations in the $2(J+1)$ unknowns γ_{jnR} and γ_{jnI}. However, unlike in the constant stratification case, there is the still an infinite sum present in each of these equations – namely, that of (3.2.18).

Rather than retaining this infinite sum, it is assumed that its associated contribution is of second-order significance compared to β_{jn}, or in other words, that I_{mnkj} is very close to a diagonal matrix. Then, the $2(J+1)$ equations can be formulated by mapping the basis functions onto $\beta_{jn} \approx \beta_{jn*}$. The validity of this assumption is examined in further detail below.

The resulting system of equations can then be expressed in compact matrix form as $A\gamma = \mathbf{b}$, where $\gamma = [\gamma_{0nr}, \gamma_{0ni}, \gamma_{1nr}, \ldots, \gamma_{Jni}]^{\mathrm{T}}$ and the matrix A and column vector $\mathbf{b}$ are defined as in (2.17) and (2.18), respectively, of Chapter 2. Here, however, the frequency-specific coefficient $\bowtie_j$ is redefined as

$$\bowtie_j = \frac{h\delta_j \omega_j \overline{N}_j^2}{\mu_j} . \tag{3.2.19}$$

Although the structure of A and $\mathbf{b}$ are similar to that of Chapter 2, it should be recalled that many of the parameters involved in constructing the matrix equation (e.g. μ_j and Z_j) are defined differently from their constant-N counterparts. In particular, the parameter β_{jn} does not have the same form as β_n from Chapter 2; β_n involves mapping the vertical velocity w onto $\sin nZ$ rather than the expression given by (3.2.14), and as such is frequency-independent in contrast to the strong dependence of frequency, ω_j, of β_{jn}. Even so, as in the constant-N scenario, the elements of the matrix A and column vector $\mathbf{b}$ can be found by quadrature. Thereafter it is straightforward to determine the complex mode strengths $\gamma_{jn} = \gamma_{jnR} + \mathrm{i}\gamma_{jnI}$ through matrix inversion.

3.3 Laboratory scales

In order to verify the algorithm outlined in § 3.2.2, a synthetic data set, representative of laboratory conditions, is generated. The iTides software (developed by the MIT ENDlab [Saidi et al., 2012]) is used to compute complex mode strengths corresponding to an input topographic profile, stratification, forcing frequency, and Coriolis frequency. It should be noted that the WKB approximation is used both in iTides for the calculation of the mode strengths themselves as well as in constructing the synthetic wave field.

Following the approach of Echeverri and Peacock [2010], the two-dimensional topography being considered here is an asymmetric Gaussian profile:

$$h_G(x) = h_0 \begin{cases} \exp\left(-\frac{x^2}{2\sigma_l^2}\right) & x \leq 0 \\ \exp\left(-\frac{x^2}{2\sigma_r^2}\right) & x > 0 \end{cases}, \tag{3.3.1}$$

where h_0 is the topographic height, and σ_l and σ_r are the standard deviations for the left and right sides, respectively. σ_r is chosen to be $h_0\mathrm{e}^{-0.5}$, and σ_l to be $\sigma_r/2$; h_0 is set to $0.3h$. The resulting shape can be seen in figure 3.3.1.

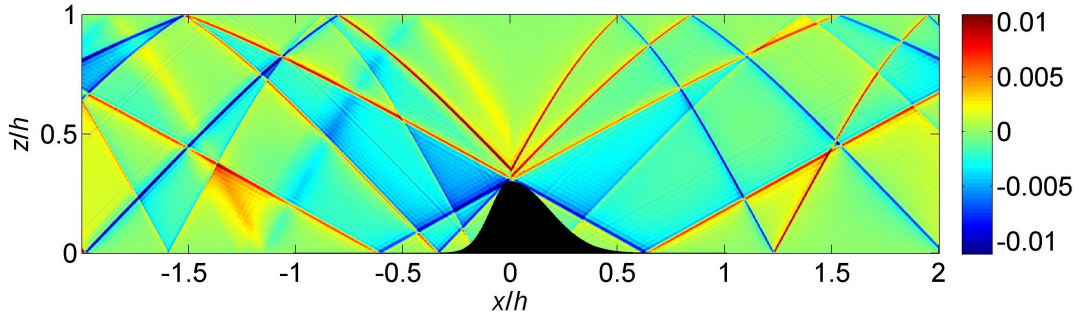

Figure 3.3.1: Snapshot of nondimensional vertical velocities $w/(N_{\text{ave}}h)$ of the internal wave field being considered, with the topographic profile given by (3.3.1).

The background stratification (with units of rad/s) is chosen to be

$$N(z) = 0.98 + 0.2506\left(\mathrm{e}^{\frac{6(z-h)}{h}} - 1\right). \tag{3.3.2}$$

This exponential profile for N is inspired by those found by Llewellyn Smith and Young [2003] in fitting data from the World Ocean Database and Hawaiian Ocean Time Series. The stratification is shown in figure 3.3.2.

An additional frequency- and depth-independent averaged buoyancy frequency N_{ave} is defined for purposes of nondimensionalization as

$$N_{\text{ave}} = \frac{1}{h}\int_0^h N(z)\,\mathrm{d}z\,. \tag{3.3.3}$$

For the stratification given by (3.3.2), the associated value of N_{ave} is 0.7710 rad/s.

Three forcing frequencies are chosen for this particular scenario, i.e. $\omega = 0.3650$ rad/s, 0.5162 rad/s, and 0.6322 rad/s (corresponding to $\omega/N_{\text{ave}} = 0.4686$, 0.6626, and 0.8116 respectively). The Coriolis frequency is chosen to be $f = 0.1825$ rad/s (corresponding to $f/N_{\text{ave}} = 0.2343$). For these frequencies, the topography described by (3.3.1) is supercritical for $x \leq 0$. For $x > 0$, the topography is subcritical for $\omega/N_{\text{ave}} = 0.8116$, supercritical for $\omega/N_{\text{ave}} = 0.4686$, and very nearly critical for $\omega/N_{\text{ave}} = 0.6626$.

The vertical velocity data are generated at each frequency and linearly superposed; the resulting (nondimensional) internal wave field is shown in figure 3.3.1

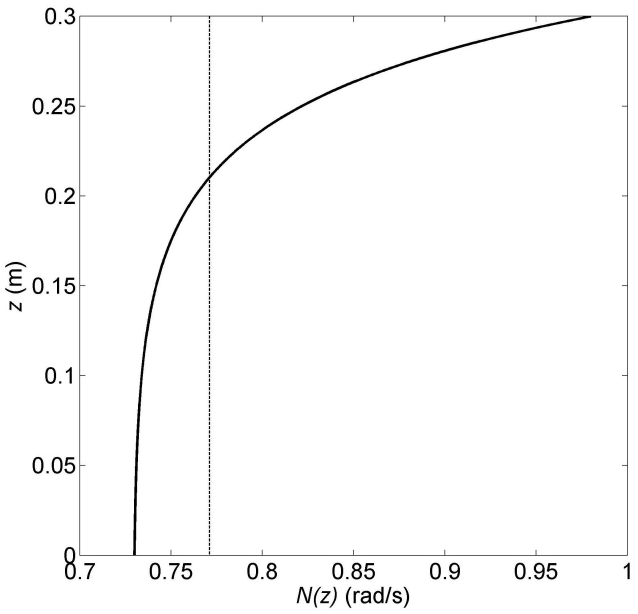

Figure 3.3.2: Model stratification for laboratory length scales. The solid black line represents the stratification given by (3.3.2), while the dashed line shows the corresponding value of N_{ave}.

at a particular instant in time, i.e. $t = 0$. Unlike the figures shown in Chapter 2 for constant stratification, internal wave rays are no longer straight lines [Kistovich and Chashechkin, 1998]. Additionally, with the topography being considered here, the resulting internal wave field exhibits a left-to-right asymmetry.

The associated timeseries data at the locations $x/h = \pm 1$ are shown in figure 3.3.3. The data here are sampled at 4 Hz for a total time of $N_{\text{ave}}T = 234$ ($T = 300\,\text{s}$). Consistent with figure 3.3.1, the wave fields on either side of the topography exhibit nontrivial qualitative differences from one another.

3.3.1 Frequency recovery

When the forcing frequencies of the internal wave field in question are unknown *a-priori*, a fast Fourier transform (FFT) is employed to find the frequency spectrum associated with the timeseries data. Although the background stratification is varying, the forcing frequencies ω_j are, of course, constant in z. As

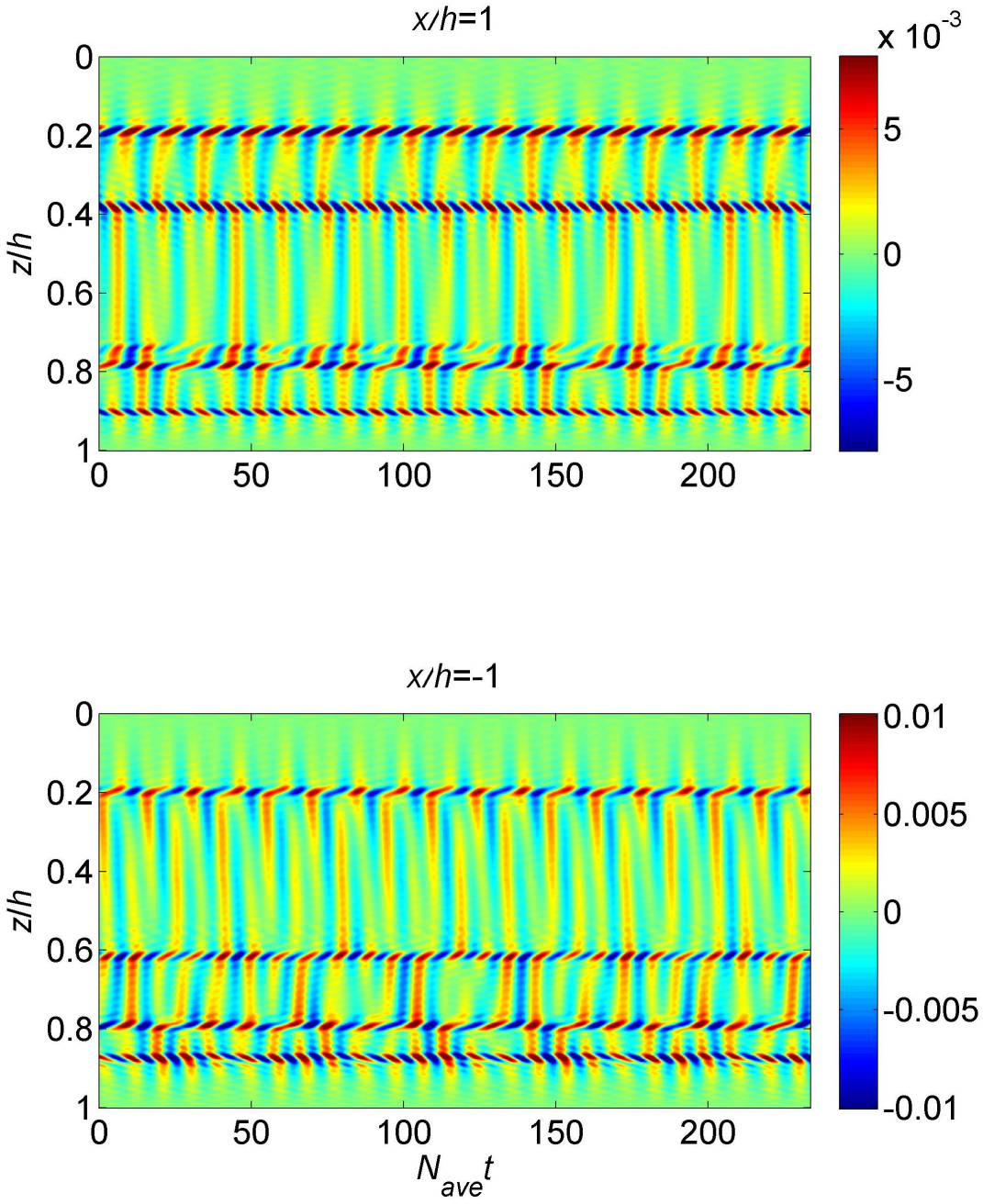

Figure 3.3.3: Nondimensional vertical velocity timeseries data $w/(N_{\text{ave}}h)$ for the internal wave field given by figure 3.3.1. The top image shows vertical velocity measurements taken at $x/h = 1$, while the bottom image shows measurements taken at $x/h = -1$. In each case, $N_{\text{ave}}T = 234$ ($T = 300\,\text{s}$).

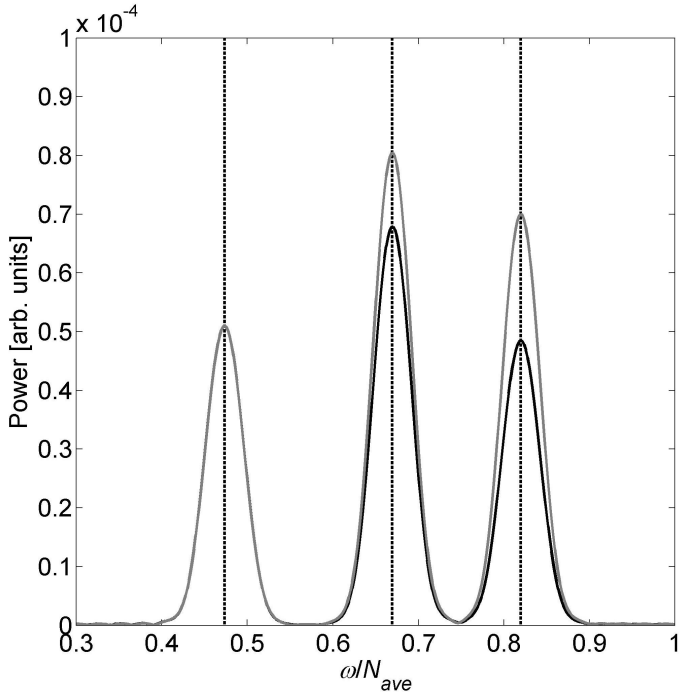

Figure 3.3.4: Frequency spectra of the vertical velocity data shown in figure 3.3.3. The solid black line corresponds to the location $x/h = 1$, while the solid grey line is from $x/h = -1$. The data are padded to $N_{\text{ave}}T = 2337$ (3000 s) and a Gauss window is applied. The vertical dashed lines represent the exact frequency values.

such, no modification to the FFT routine described in Chapter 2 is required for frequency recovery for wave fields with variable N.

The FFT outputs for the timeseries data of figure 3.3.3 are shown in figure 3.3.4. The data are padded with zeros to a total length of $N_{\text{ave}}T = 2337$ (3000 s), and a Gauss window is applied. As expected, the spectra for the wave field on either side of the topography exhibit coincident peaks.

3.3.2 Mode recovery

As noted in § 3.2.2, in constructing the matrix equation $A\gamma = \mathbf{b}$, the influence of the ς_{jn} values, as defined by (3.2.18), are assumed to be second-order relative to the β_{jn*} and are thus neglected in the definition of the matrix equation. To assess the validity of this approximation with reference to the present example, the

Table 3.3.1: Mode 1 relative values of β_{jn} and ς_{jn} when mapped onto the basis functions $\cos\omega_j t$ and $\sin\omega_j t$, at $x/h = 1$. Forcing frequencies ω_j are expressed in rad/s.

ω_j	$\int \varsigma_{jn}\cos\omega_j t\,\mathrm{d}t$	$\int \beta_{jn}\cos\omega_j t\,\mathrm{d}t$	$\int \varsigma_{jn}\sin\omega_j t\,\mathrm{d}t$	$\int \beta_{jn}\sin\omega_j t\,\mathrm{d}t$
0.3650	1.36×10^{-6}	-2.19×10^{-3}	-6.86×10^{-6}	9.13×10^{-4}
0.5162	-4.82×10^{-8}	-1.29×10^{-3}	2.14×10^{-6}	-8.20×10^{-4}
0.6322	-9.85×10^{-10}	1.02×10^{-4}	3.21×10^{-9}	-8.04×10^{-4}

values of $\int_0^T \sum_{k=0,k\neq j}^{J} \varsigma_{jn}\cos\omega_j t\,\mathrm{d}t$ and $\int_0^T \sum_{k=0,k\neq j}^{J} \varsigma_{jn}\sin\omega_j t\,\mathrm{d}t$ are computed using the first 100 modes and compared, in table 3.3.1, with the associated values from the $\mathbf{b}$ vector. Here

$$\mathbf{b} = \begin{bmatrix} \int_0^T \beta_{0n}\cos\omega_0 t\,\mathrm{d}t \\ \int_0^T \beta_{0n}\sin\omega_0 t\,\mathrm{d}t \\ \int_0^T \beta_{1n}\cos\omega_1 t\,\mathrm{d}t \\ \vdots \\ \int_0^T \beta_{Jn}\sin\omega_J t\,\mathrm{d}t \end{bmatrix} = \begin{bmatrix} \int_0^T (\beta_{0n*}+\varsigma_{jn})\cos\omega_0 t\,\mathrm{d}t \\ \int_0^T (\beta_{0n*}+\varsigma_{jn})\sin\omega_0 t\,\mathrm{d}t \\ \int_0^T (\beta_{1n*}+\varsigma_{jn})\cos\omega_1 t\,\mathrm{d}t \\ \vdots \\ \int_0^T (\beta_{Jn*}+\varsigma_{jn})\sin\omega_J t\,\mathrm{d}t \end{bmatrix}. \tag{3.3.4}$$

For all three frequencies considered, the magnitudes of the ς_{jn} terms are at least two orders of magnitude smaller than those of the β_{jn} terms. Thus, the assumption that these terms have relatively little influence on the system of equations $A\gamma = \mathbf{b}$ (i.e. $\beta_{jn} \approx \beta_{jn*}$) appears to be justified.

The mode strength magnitudes corresponding to the locations $x/h = 1$ and $x/h = -1$ are shown in figure 3.3.5 for both the generating frequencies and the frequencies found from the FFT outputs. Excellent qualitative and quantitative agreement is seen between the calculated values of the mode strength magnitudes $|\gamma_{jn}|$ and those given directly by iTides. In contrast to figure 2.6, the small errors in the frequencies found using FFT do not appear to significantly influence the veracity of this comparison. As expected, figure 3.3.5 shows that the spatial structure of the wave field varies depending on which side of the asymmetric topography is being considered.

Finally, it should be noted that the synthetic data is itself generated using the

WKB approximation, and so in comparing the theoretical and recovered modes in figure 3.3.5 no additional error has been introduced through the use of this approximation. Clearly, however, some care must be applied when considering low vertical modes for which it may be inaccurate to assume that N varies slowly over the vertical wavelength.

3.4 Oceanographic scales

Because the modal decomposition algorithm described in Chapter 2 and in § 3.2.2 is intended to be used for both experimental and observational data, it is of interest to consider data at oceanographic length scales. For illustrative purposes, the topographic profile given by (3.3.1) is scaled to an ocean of depth $h = 5000\,\mathrm{m}$, with $h_0 = 0.3h$ and standard deviations $\sigma_r = h_0 \mathrm{e}^{-0.5}$ (as above) and $\sigma_l = 5\sigma_r$. The background stratification used in generating the synthetic data is that given by Llewellyn Smith & Young's fit to stratification data from the World Ocean Database (with units of cycles per hour):

$$N(z') = 0.35 + 0.0115\big(\mathrm{e}^{5.85z'/h} - 1\big) \tag{3.4.1}$$

where the vertical coordinate z' is defined such that $z' = 0$ at the ocean surface and $z' = -h$ at the ocean floor [Llewellyn Smith and Young, 2003].

The forcing frequencies used correspond to the five primary tidal constituents (M2, K1, S2, N2, and O1), and can be seen in table 3.4.1. The data are generated using a Coriolis frequency of $1.8822 \times 10^{-5}\,\mathrm{rad/s}$, corresponding to a location of 15° latitude.

A snapshot image of the (nondimensionalized) vertical velocities of the associated wave field at time $t = 0$ is shown in figure 3.4.1. The corresponding vertical velocity timeseries data measured at the locations $x/h = \pm 3$ are shown in figure 3.4.2 for a total time of $N_{\mathrm{ave}}T = 359$ ($T = 168\,\mathrm{hr}$), sampled once per hour.

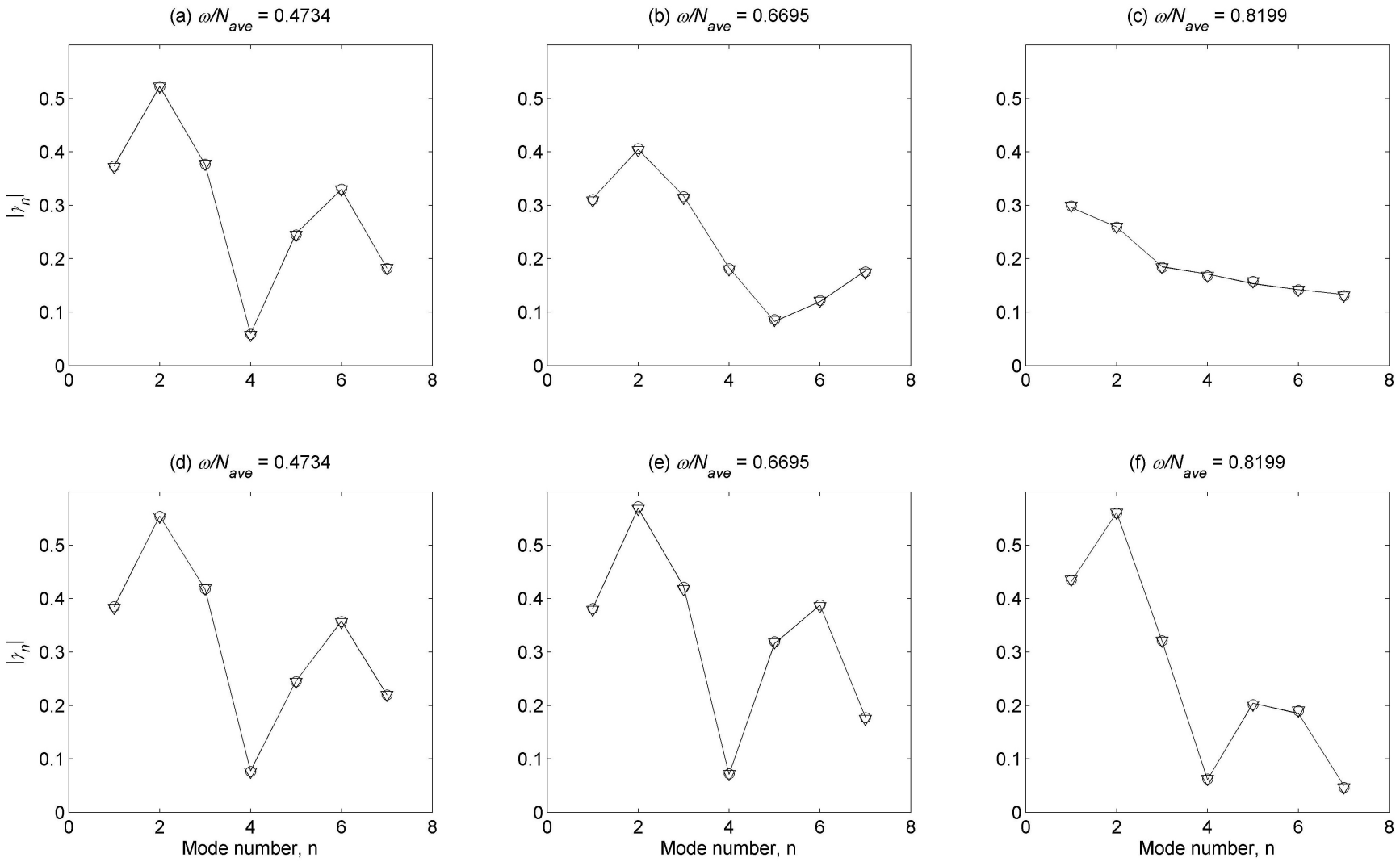

Figure 3.3.5: Mode strengths calculated from the vertical velocity timeseries data of figure 3.3.3. Panels (a)-(c) are calculated for $x/h = 1$, while panels (d)-(f) are calculated for $x/h = -1$. The triangles correspond to mode strengths calculated with FFT frequencies, the circles to mode strengths calculated with generating frequencies, and the solid lines to the mode strengths given directly using iTides.

Table 3.4.1: Primary tidal constituents included in the internal wave fields of figures 3.4.1 and 3.4.2. (Frequencies are based on data from NOAA Tides & Currents website (`http://co-ops.nos.noaa.gov/`).)

Tidal constituent	Frequency (rad/s)
M2	1.4052×10^{-4}
K1	7.2921×10^{-5}
S2	1.4544×10^{-4}
N2	1.3788×10^{-4}
O1	6.7598×10^{-5}

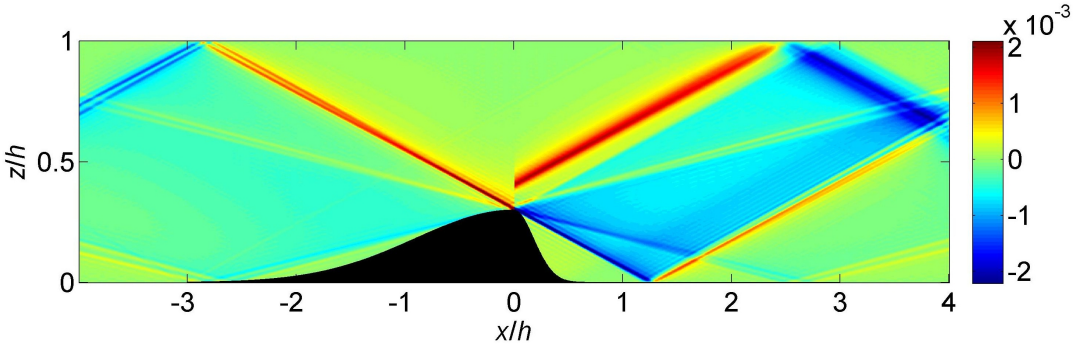

Figure 3.4.1: Snapshot of nondimensional vertical velocity field $w/(N_{\text{ave}}h)$ for oceanographic length scales. Note that the discontinuity seen at $x/h = 0$ is an artificat of using an expression for far-field vertical velocity in generating synthetic data in the near field.

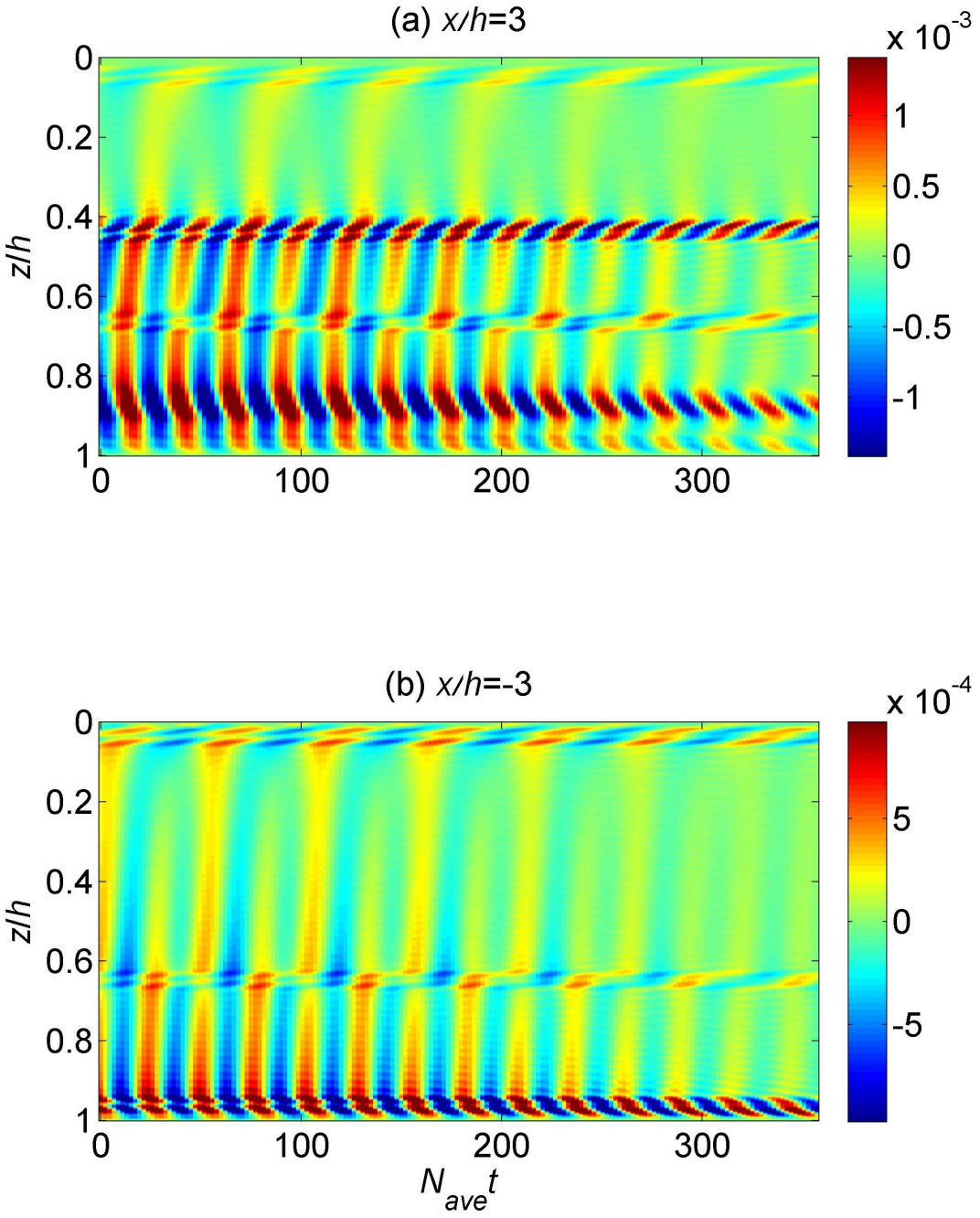

Figure 3.4.2: Nondimensional vertical velocity timeseries data $w/(N_{\text{ave}}h)$ corresponding to the wave field in figure 3.4.1. Panel (a) is measured at $x/h = 3$, while panel (b) is measured at $x/h = -3$, for $N_{\text{ave}}T = 359$ ($T = 168\,\text{hr}$).

Using the matrix equation $A\gamma = \mathbf{b}$ and the exact forcing frequencies corresponding to the five tidal constituents, the mode strength magnitudes can then be determined, as shown in figure 3.4.3. Consistent with the discussion of § 3.3.2, there is excellent qualitative and quantitative agreement between the mode strengths recovered from the vertical velocity timeseries data and the input mode strengths specified by iTides.

Note moreover that at both locations considered in figure 3.4.2, the modal decomposition associated with the diurnal tidal constituents (O1 and K1) shows a different trend from that of the semidiurnal tidal constituents (M2, S2, and N2). These differences are more pronounced in panels (f) through (j), corresponding to $x/h < 1$ for which the topography is supercritical for the diurnal constituents but subcritical for the semidiurnal constituents.

However, there is relatively little variation in the recovered mode strength magnitudes amongst the diurnal constituents (panels (a) vs. (b) and (f) vs. (g)) and also the semidiurnal constituents (panels (c) vs. (d) vs. (e) and (h) vs. (i) vs. (j)). This is to be expected; as discussed in § 2.5.1, small changes in the forcing frequency yield relatively little change in the overall modal decomposition associated with the frequency component in question.

3.5 Discussion and conclusions

The modal decomposition algorithm described in Chapter 2 has been extended to the scenario of a polychromatic internal wave field in a stratified fluid with varying buoyancy frequency (i.e. nonlinear stratification). The buoyancy frequency profiles considered here are such that all forcing frequencies ω_j are less than $N(z)$ throughout the entire depth of the ocean, i.e. the waves do not become evanescent at any point throughout the fluid depth. As such, turning points such as those considered by King et al. [2012], or instances of internal wave beam ducting [Mathur and Peacock, 2009], are not considered within the

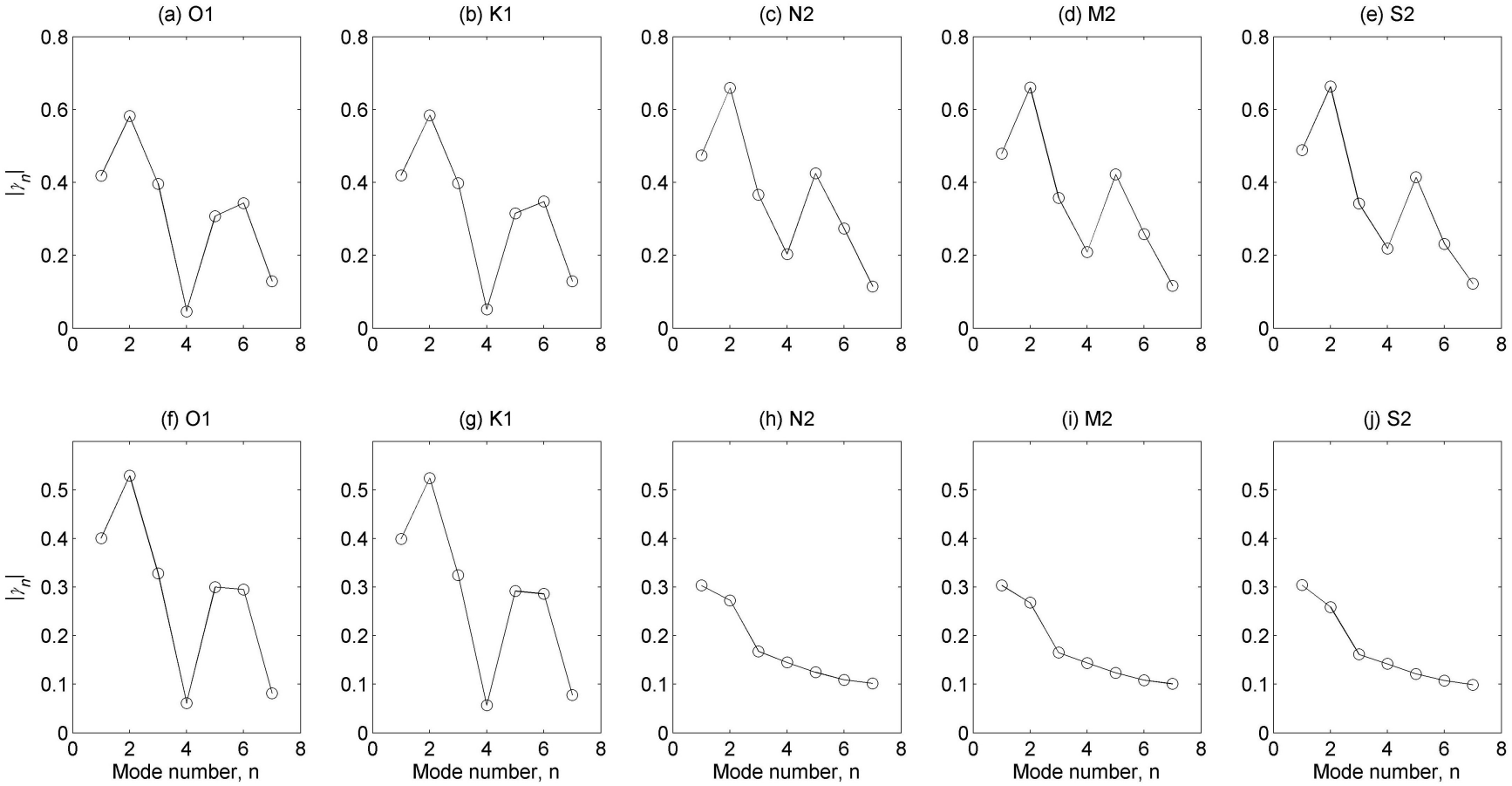

Figure 3.4.3: Calculated mode strengths for the synthetic data at oceanographic scales at $x/h = \pm 3$. The top row (a-e) are calculated using the data from the top panel of figure 3.4.2, while the bottom row (f-j) are calculated from the data in the bottom panel of figure 3.4.2. The circles correspond to the calculated mode strengths, and the solid black lines are the mode strengths calculated directly using iTides.

context of the modal decomposition algorithm outlined in § 3.2.2.

For verification of the modal decomposition approach outlined above, synthetic data generated at both laboratory and oceanographic length scales is considered, using theoretical mode strengths generated using the iTides software [Saidi et al., 2012]. Excellent quantitative agreement is seen when comparing the calculated and theoretical mode strengths, for both exact frequencies and those determined by an FFT routine.

This accuracy should be interpreted with some care, however, because the generation and modal decomposition of the synthetic data each presume a slowly varying background stratification so that the WKB approximation may be applied. However, for a profile such as that shown in figure 3.3.2, the stratification changes relatively rapidly near the free surface compared to the large length scales of the low-mode waves. When considering real internal wave fields, some inaccuracy is thus expected for the lower modes. In oceanographic settings, the low modes tend to be more energetic than the high modes [Di Lorenzo et al., 2006], and consequently errors in the estimated tidal conversion by a given topographic feature may arise.

This investigation, unlike with the Green's function approach commonly used in studies of tidal conversion [Balmforth et al., 2002; Llewellyn Smith and Young, 2003; Pétrélis et al., 2006; Balmforth and Peacock, 2009; Echeverri and Peacock, 2010], does not require knowledge of the specifics of the generating topography to determine the mode strengths associated with each forcing frequency. Instead, the mode strengths are computed from vertical velocity timeseries data alone.

Whereas satisfactory results have been found when considering synthetic data at both laboratory and oceanographic length scales, this algorithm has not yet been applied to real experimental or observational data.Because additional complications may arise with such measurements (e.g. noise, measure-

ment uncertainty, or difficulties in measuring velocities near the extremes of the domain), the robustness of this algorithm when faced with such complications remains to be evaluated.

Thus far, a two-dimensional topographic profile has been assumed. However, when considering three-dimensional topography, the resulting wave field may exhibit several significant differences owing to the ability of fluid parcels to go around (rather than simply over) the topography. Furthermore, the assumption of a linear wave field precludes the consideration of nonlinear effects (e.g. the Parametric Subharmonic Instability) which may play an important role in the evolution of a tidally-forced internal wave field (particularly for high-mode components) [St. Laurent and Garrett, 2002]. Such activity is expected to become significant for large tidal excursions [Echeverri et al., 2009]. As such, the algorithm described herein should in the future be adapted to include these additional physical phenomena.

3.A Derivation of expressions from § 3.2.2

3.A.1 Derivation of the expression for β_{jn}

The expression for the vertical velocity field as forced by multiple forcing frequencies reads

$$w = \sum_{k=0}^{J} \operatorname{sgn}(X_k) \frac{\delta_k \omega_k}{\mu_k} \left\{ \sum_{m=1}^{\infty} [\gamma_{kmr} \cos(\varphi_{km} - \omega_k t) - \gamma_{kmi} \sin(\varphi_{km} - \omega_k t)] \frac{\sin m Z_k}{\sqrt{\mathcal{N}_k}} \right\} \tag{3.2.11}$$

where

$$\varphi_{km} = |mX_k| + \pi/2\,. \tag{3.2.12}$$

The right-hand side of (3.2.11) is multiplied by

$$\frac{\sin nZ_j}{\sqrt{\mathcal{N}_j}} (N^2 - \omega_j^2) \operatorname{sgn}(X_j) \tag{3.2.14}$$

and note that $\mathrm{sgn}(X_j) = \mathrm{sgn}(X_k)$. This yields

$$\sum_{k=0}^{J} \frac{\delta_k \omega_k}{\mu_k} \left\{ \sum_{m=1}^{\infty} [\gamma_{kmr} \cos(\varphi_{km} - \omega_k t) - \gamma_{kmi} \sin(\varphi_{km} - \omega_k t)] \right.$$
$$\left. \times \frac{\sin mZ_k}{\sqrt{\mathcal{N}_k}} \frac{\sin nZ_j}{\sqrt{\mathcal{N}_j}} (N^2 - \omega_j^2) \right\} . \qquad (3.A.1)$$

Integrating the above expression over the depth $0 \leq z \leq h$ yields

$$\beta_{jn} \equiv \sum_{k=0}^{J} \frac{\delta_k \omega_k}{\mu_k} \left\{ \sum_{m=1}^{\infty} [\gamma_{kmr} \cos(\varphi_{km} - \omega_k t) - \gamma_{kmi} \sin(\varphi_{km} - \omega_k t)] \right.$$
$$\left. \times \int_0^h \frac{\sin mZ_k}{\sqrt{\mathcal{N}_k}} \frac{\sin nZ_j}{\sqrt{\mathcal{N}_j}} (N^2 - \omega_j^2) \, \mathrm{d}z \right\} . \qquad (3.A.2)$$

Recalling that

$$\mathcal{N}_j = \frac{1}{\overline{N}_j} \sqrt{N(z)^2 - \omega_j^2} \, , \qquad (3.2.2)$$

(3.A.2) can be written as

$$\int_0^h \frac{\sin mZ_k}{\sqrt{\sqrt{N^2 - \omega_k^2}/\overline{N}_k}} \frac{\sin nZ_j}{\sqrt{\sqrt{N^2 - \omega_j^2}/\overline{N}_j}} (N^2 - \omega_j^2) \, \mathrm{d}z \, . \qquad (3.A.3)$$

Because $\overline{N}_j$ and $\overline{N}_k$ are independent of height, the above expression can be replaced with

$$\sqrt{\overline{N}_j \overline{N}_k} \int_0^h \sin mZ_k \sin nZ_j \sqrt[4]{\frac{(N^2 - \omega_j^2)^3}{N^2 - \omega_k^2}} \, \mathrm{d}z \, , \qquad (3.A.4)$$

which matches the right-hand side of (3.2.13). Thus β_{jn} can be written as

$$\beta_{jn} = \sum_{k=0}^{J} \frac{\delta_k \omega_k}{\mu_k} \sum_{m=1}^{\infty} [\gamma_{kmr} \cos(\varphi_{km} - \omega_k t) - \gamma_{kmi} \sin(\varphi_{km} - \omega_k t)] \, I_{mnkj} \qquad (3.2.15)$$

3.A.2 Orthogonal and non-orthogonal components

Equation (3.2.15) contains an infinite sum and is therefore awkward to apply in the process of recovering the mode strengths for a given wave field. Here the this expression is decomposed into two components with the objective of further simplifying the above results.

This is achieved by first adding zero to β_{jn} in the form of

$$\sum_{k=0}^{J} \frac{\delta_k \omega_k}{\mu_k} [\gamma_{knr} \cos(\varphi_{kn} - \omega_k t) - \gamma_{kni} \sin(\varphi_{kn} - \omega_k t)] \left(\frac{h\overline{N}_j^2}{2} - \frac{h\overline{N}_j^2}{2} \right), \quad (3.A.5)$$

i.e.

$$\begin{aligned}
\beta_{jn} &= \sum_{k=0}^{J} \left\{ \frac{\delta_k \omega_k}{\mu_k} \sum_{m=1}^{\infty} \left([\gamma_{kmr} \cos(\varphi_{km} - \omega_k t) - \gamma_{kmi} \sin(\varphi_{km} - \omega_k t)] \, I_{mnkj} \right) \right. \\
&\quad \left. + \frac{\delta_k \omega_k}{\mu_k} [\gamma_{knr} \cos(\varphi_{kn} - \omega_k t) - \gamma_{kni} \sin(\varphi_{kn} - \omega_k t)] \left(\frac{h\overline{N}_j^2}{2} - \frac{h\overline{N}_j^2}{2} \right) \right\} \\
&= \sum_{k=0}^{J} \frac{\delta_k \omega_k}{\mu_k} \left\{ [\gamma_{knr} \cos(\varphi_{kn} - \omega_k t) - \gamma_{kni} \sin(\varphi_{kn} - \omega_k t)] \frac{h\overline{N}_j^2}{2} \right\} \\
&\quad + \sum_{k=0}^{J} \frac{\delta_k \omega_k}{\mu_k} \left\{ \sum_{m=1}^{\infty} \left([\gamma_{kmr} \cos(\varphi_{km} - \omega_j t) - \gamma_{kmi} \sin(\varphi_{km} - \omega_j t)] I_{mnkj} \right) \right. \\
&\quad \left. - \left([\gamma_{knr} \cos(\varphi_{kn} - \omega_j t) - \gamma_{kni} \sin(\varphi_{kn} - \omega_j t)] \frac{h\overline{N}_j^2}{2} \right) \right\}. \quad (3.A.6)
\end{aligned}$$

When $\omega_k = \omega_j$, the integral $I_{mnkj} = I_{mnjj}$ can be further simplified through orthogonality to give

$$I_{mnjj} = \frac{h\overline{N}_j^2}{2} \delta_{mn} \qquad \text{where} \qquad \delta_{mn} = \begin{cases} 1 & m = n \\ 0 & m \neq n \end{cases}. \quad (3.A.7)$$

I_{mnjj} is an orthogonality condition, i.e. $\sin mZ_j$ and $\sin nZ_j$ are orthogonal with weight $N^2 - \omega_j^2$ [Haberman, 2004]. Notice in particular that $I_{mmjj} = I_{nnjj} = (h\overline{N}_j^2)/2$.

Thus, (3.A.6) can be expressed as

$$\beta_{jn} = \beta_{jn*} + \varsigma_{jn} \quad (3.2.16)$$

where

$$\beta_{jn*} = \sum_{k=0}^{J} \frac{\delta_k \omega_k}{\mu_k} \left([\gamma_{knr} \cos(\varphi_{kn} - \omega_k t) - \gamma_{kni} \sin(\varphi_{kn} - \omega_k t)] \frac{h\overline{N}_j^2}{2} \right) \quad (3.2.17)$$

and

$$\begin{aligned}
\varsigma_{jn} &= \frac{\delta_k \omega_k}{\mu_k} \left\{ \sum_{m=1}^{\infty} \left([\gamma_{kmr} \cos(\varphi_{km} - \omega_j t) - \gamma_{kmi} \sin(\varphi_{km} - \omega_j t)] I_{mnkj} \right) \right. \\
&\quad \left. - \left([\gamma_{knr} \cos(\varphi_{kn} - \omega_j t) - \gamma_{kni} \sin(\varphi_{kn} - \omega_j t)] \frac{h\overline{N}_j^2}{2} \right) \right\}.
\end{aligned}$$

The variable β_{jn*} represents the component of β_{jn} that would be obtained were I_{mnkj} identically equal to the orthogonal expression I_{mnjj} as given by (3.A.7). Conversely the variable ς_{jn} can be thought of as the "non-orthogonal" component of β_{jn}, or the component that arises due to the fact that I_{mnkj} is not exactly a diagonal matrix (although it is diagonally dominant). Assuming that $\beta_{jn} \approx \beta_{jn*}$ allows the matrix equation $A\gamma = \mathbf{b}$ to be defined in the absence of the infinite sum from (3.2.18).

Bibliography

N. J. Balmforth and T. Peacock. Tidal conversion by supercritical topography. *Journal of Physical Oceanography*, 39(8):1965–1974, 2009.

N. J. Balmforth, G. R. Ierley, and W. R. Young. Tidal conversion by subcritical topography. *Journal of Physical Oceanography*, 32(10):2900–2914, 2002.

E. Di Lorenzo, W. R. Young, and S. Llewellyn Smith. Numerical and analytical estimates of M_2 tidal conversion at steep oceanic ridges. *Journal of Physical Oceanography*, 36(6):1072–1084, 2006.

P. Echeverri and T. Peacock. Internal tide generation by arbitrary two-dimensional topography. *Journal of Fluid Mechanics*, 659:247–266, 2010.

P. Echeverri, M. R. Flynn, K. B. Winters, and T. Peacock. Low-mode internal tide generation by topography: an experimental and numerical investigation. *Journal of Fluid Mechanics*, 636:91–108, 2009.

A. E. Gill. *Atmosphere-Ocean Dynamics*. Academic Press, Inc., New York, NY, 1982. ISBN 0-12-283520-4.

R. Haberman. *Applied Partial Differential Equations with Fourier Series and Boundary Value Problems*. Pearson Prentice Hall, Upper Saddle River, NJ, fourth edition, 2004. ISBN 0-13-065243-1.

B. King, M. Stone, H. P. Zhang, T. Gerkema, M. Marder, R. B. Scott, and H. L. Swinney. Buoyancy frequency profiles and internal semidiurnal tide turning

depths in the oceans. *Journal of Geophysical Research*, 117(C04008):1–15, 2012.

Y. Kistovich and Y. D. Chashechkin. Linear theory of the propagation of internal wave beams in an arbitrarily stratified liquid. *Journal of Applied Mechanics and Technical Physics*, 39(5):729–737, 1998.

S. G. Llewellyn Smith and W. R. Young. Tidal conversion at a very steep ridge. *Journal of Fluid Mechanics*, 495:175–191, 2003.

M. Mathur and T. Peacock. Internal wave beam propagation in non-uniform stratifications. 639:133–152, 2009.

J. Pedlosky. *Waves in the Ocean and Atmosphere: Introduction to Wave Dynamics*. Springer-Verlag, Berlin, 2003. ISBN 3540003401.

F. Pétrélis, S. Llewellyn Smith, and W. R. Young. Tidal conversion at a submarine ridge. *Journal of Physical Oceanography*, 36(6):1053–1071, 2006.

S. Saidi, M. Mercier, P. Echeverri, M. Mathur, and T. Peacock. iTides manual. `http://sourceforge.net/projects/itides/`, 2012. [accessed 07-05-2012].

L. St. Laurent and C. Garrett. The role of internal tides in mixing the deep ocean. *Journal of Physical Oceanography*, 32:2882–2899, 2002.

Chapter 4

Conclusions

4.1 Summary of present contribution

In this thesis, an algorithm has been developed which finds the complex mode strengths, γ_{jn}, or normalized mode strength ratios, $\gamma_{jn}/|\gamma_{j1}|$, of a tidally-forced polychromatic internal wave field from velocity timeseries data alone. This approach differs from past analytical work in the field of tidal conversion in two fundamental respects. First of all, unlike in the Green's function approach to calculating these mode strengths, no knowledge of the specific details of the topographic profile generating the internal wave field is needed – rather, the structure of the wave field is found from velocity timeseries data alone. Secondly, this algorithm examines polychromatic wave fields, unlike the monochromatic wave fields commonly considered in past theoretical and laboratory experimental work. In this chapter, further salient details of the algorithm for linear and nonlinear background stratifications are reviewed and areas for future research that may extend the present model to still more realistic geophysical scenarios are identified.

4.1.1 Linear stratification

If the frequency spectrum of the system is unknown, a fast Fourier transform (FFT) routine is used to ascertain which forcing frequencies are present. Both

zero-padding and windowing are employed to improve the resulting spectrum: zero-padding to achieve finer frequency resolution and windowing to decrease spectral leakage. As mentioned in § 2.3.1, the forcing frequencies correspond to peaks in the frequency spectrum; a mean flow superposed on the wave field would give a peak at $\omega/N = 0$. Using the $J + 1$ forcing frequencies (either recovered from the FFT analysis or known *a-priori*), a $2(J + 1) \times 2(J + 1)$ system of equations can be constructed for each mode n. Writing this system in compact matrix form as $A\boldsymbol{\Upsilon} = \mathbf{b}$ (where A, $\mathbf{b}$, and $\boldsymbol{\Upsilon}$ are defined by (2.17), (2.18), and (2.19), respectively), the values of $\boldsymbol{\Upsilon}$ can be found through matrix inversion. With these values, it is then straightforward to solve for the complex mode strengths γ_{jn} or normalized mode strength ratios $\gamma_{jn}/|\gamma_{j1}|$ using (2.23).

Synthetic data based on the theory of Pétrélis et al. [2006] are used for validation of the algorithm. Vertical velocity timeseries data are generated for each forcing frequency and superposed to create polychromatic linear internal wave fields in a fluid of constant buoyancy frequency, N, as forced by a symmetric Gaussian topography.[1] These data have been shown to be of high fidelity, both experimentally [Echeverri et al., 2009] and numerically [Di Lorenzo et al., 2006]. In comparing the theoretical mode strengths used in constructing the synthetic data with those recovered by the matrix equation approach described above, excellent qualitative and quantitative agreement is found when forcing frequencies are known precisely. Although some small discrepancies are observed when forcing frequencies are not known precisely, the observed agreement is still very good, as shown in figures 2.6 and 2.10. This verification is performed using wave fields consisting of either a limited or large number of discrete forcing frequencies where in either case the timeseries is of sufficient length to adequately resolve each individual peak in the power spectrum (see e.g. figures 2.8 and

[1]It should be noted, however, that neither the work of Pétrélis et al. nor the algorithm described here are limited to Gaussian topographies.

2.11).

The impact of additional unresolved frequencies (i.e. frequencies not included in the construction of the matrix equation) is examined in § 2.5.1. Equations (2.27) and (2.29) demonstrate that the impact of these unresolved frequencies decreases with increasing timeseries length T. This is seen when considering additional forcing frequencies above, below, or in the middle of the frequency range being resolved; for the aforementioned synthetic data sets where NT is on the order of 400 to 4000, the recovered mode strengths are not significantly influenced by these additional frequency components.

With this in mind, data corresponding to a continuous frequency spectrum are considered. For the long timeseries examined in this work, the recovered mode strength ratios exhibit excellent qualitative and quantitative agreement. However, the minimum allowable frequency spacing within the A matrix to avoid large condition numbers, $\Delta\omega_{\min}$, is found to scale inversely with timeseries length, T. For synthetic timeseries data such as that considered here, this is not a major concern because the timeseries length can be made arbitrarily long and thus the frequency spacing can be made arbitrarily fine. Additionally, for such long timeseries, the preceding discussion suggests that unresolved interstitial frequencies, which must arise for any timeseries of finite length, have only a small significance. However, for experimental flows such as those considered by Flynn and Sutherland [2004], the associated short timeseries length demands a coarse frequency spacing so as to avoid ill-conditioned matrices and suggests that unresolved interstitial frequencies will exert a more marked influence. As such, the short timeseries length of such flows is an acute limitation in accurately resolving the associated modal structure.

In § 2.5.2, an alternate approach to finding the modal structure of polychromatic wave fields is considered, i.e. rather than solving the $2(J+1) \times 2(J+1)$ system of equations as before, a single forcing frequency is instead isolated us-

ing a bandpass filter and the mode strengths are then found for this filtered monochromatic wave field (using only a 2×2 matrix equation). Here, a Butterworth bandpass filter is applied to a wave field forced by several sparsely-spaced discrete forcing frequencies, and the associated normalized mode strength ratios are calculated. As figure 2.14 shows, while good agreement between the theoretical mode strength ratios and those calculated from the filtered wave field is found for longer timeseries lengths, the recovered ratios begin to deviate from the theoretical value for small NT. This is due to the non-ideal behaviour exhibited by bandpass filters for shorter timeseries; in the case of the Butterworth filter considered here, the passbands become very wide as T becomes small, and as such the filter does not fully attenuate the other frequencies in the system. Consequently, for shorter timeseries it is found that the $2(J+1) \times 2(J+1)$ matrix equation gives more accurate values for the recovered mode strength ratios.

4.1.2 Nonlinear stratification

Because the stratification of the oceans and atmosphere cannot, in general, be characterized by a constant buoyancy frequency, it is appropriate to extend the algorithm described above to the case of a nonlinear stratification. In order to consider the effects of a vertically-varying buoyancy frequency N, the Wentzel-Kramers-Brillouin (WKB) approximation is employed, as discussed by Llewellyn Smith and Young [2003] and Echeverri and Peacock [2010].

Frequency information, if unknown, can be found through the same FFT procedure as for the constant-N case. For an inviscid wave field, a $2(J+1) \times 2(J+1)$ matrix equation, $A\gamma = \mathbf{b}$, can be derived using the associated frequencies (see § 3.2.2). Here the contribution of "non-orthogonal" components is neglected; mathematically speaking, the matrix I_{mnkj}, defined by (3.2.13), is regarded as diagonal rather than diagonally dominant. This assumption is

justified *a-posteriori* by contrasting the magnitudes of the diagonal and off-diagonal elements of I_{mnkj}. As indicated in table 3.3.1, the former are larger than the latter by roughly three orders of magnitude. As such, the resulting matrix equation can be inverted to find the complex mode strengths γ_{jn}.

Again, synthetic data are used to verify the algorithm, constructed by linearly superposing the contributions of the $J + 1$ forcing frequencies present within the system. The theoretical mode strengths are found using the iTides software [Saidi et al., 2012]. Two scenarios are examined here, namely a wave field at laboratory length scales and another at oceanographic length scales. In either circumstance, the background stratification used in generating the data is based on the exponential profiles found by Llewellyn Smith and Young [2003] in fitting data from the World Ocean Database. The topographic profiles considered here are chosen to be asymmetric Gaussian profiles, based on those considered by Echeverri and Peacock [2010].

For both the laboratory and oceanographic cases, excellent qualitative and quantitative agreement is found between the mode strengths given by iTides and those recovered through the modal decomposition algorithm. This agreement is observed for timeseries data on both sides of the asymmetric topography, as indicated by figures 3.3.5 and 3.4.3. It is, however, important to note that the WKB approximation was used in both calculating the theoretical mode strengths and constructing the synthetic wave fields, and as such no additional errors are introduced through the use of this approximation in the modal decomposition algorithm. Because the WKB approximation assumes that the background buoyancy frequency only changes a small amount over the length scale of the internal wave, when considering "real" data sets errors are expected in the values returned for the mode strengths of the lower modes (i.e. $n = 1, 2, 3, \ldots$), for which this assumption may be invalid.

4.2 Outlook and future work

Although the algorithm described herein is able to consider polychromatic internal wave fields in nonlinear stratifications, there remain several future adaptations so as to improve the applicability of the model to real geophysical scenarios.

Firstly, whereas the algorithm has been verified using synthetic data generated at both laboratory and oceanographic scales, giving excellent qualitative and quantitative agreement between recovered and theoretical mode strengths, this approach remains untested on either experimental or observational data. Such data sets introduce additional complications, compared to their synthetic counterparts. For instance, image loss near the edges of the domain ($z = 0$ and $z = h$), seen in both experimental and observational measurements, leads to a spatial truncation of the timeseries data. Thus the trigonometric orthogonality properties, used to expeditious effect in eliminating the infinite sum of (2.13), can no longer be exploited. Whereas the impact of such truncation is reduced when using the vertical velocity field w rather than horizontal velocity or perturbation buoyancy fields, image loss can still impact the overall accuracy of the recovered mode strengths. This is true even in the case of the variable-N algorithm for which the definition of β_{jn} does not explicitly exploit orthogonality. In particular, the validity of the assumption that the diagonally-dominant matrix I_{mnkj} (as defined by (3.2.13)) can be replaced with a diagonal matrix when the domain is truncated due to image loss would need to be further examined.

Furthermore, physical measurements introduce additional complications. Instrument resolution, for example, may lead to uncertainties in the recovered values of the mode strengths [Taylor, 1997]. Therefore, the algorithm's sensitivity to noise should be assessed, e.g. by the addition of random numbers into the synthetically-determined wave fields, although random noise is expected to have less impact on the low modes (which are of particular interest) as op-

posed to the higher modes. As best as possible, the significance of these additional measurement-related considerations should be quantified when applying the modal decomposition algorithm to experimental or observational data. However, there is reason to be optimistic that application of this algorithm to experimental data will still yield robust results, given the good agreement between experimental and synthetic data shown in figure 2 of Echeverri et al. [2009].

Moreover, although wave fields in nonlinear background stratification have been considered here, there is still an implicit assumption that the forcing frequencies ω_j are everywhere less than the minimum value of the buoyancy frequency N, i.e. the relationship $0 < \omega < N$ is satisfied and the internal waves at no point become evanescent within the domain $0 < z < h$. However, this is not necessarily true within a geophysical setting; such phenomena as internal wave turning points [King et al., 2012], tunnelling [Mathur and Peacock, 2009], and vanishing internal wave beams [Gerkema and van Haren, in press, 2012] are anticipated when the forcing frequency at some point exceeds the local value of the buoyancy frequency. In these locations where $\omega > N$, the vertical wavenumber m becomes imaginary (as shown by equations (1.2) and (1.3)), and internal waves are no longer able to propagate as before. Instead, their amplitude decays exponentially in z [Sutherland, 2010]. In order to consider such additional effects associated with nonlinear stratification, further adaptations to the modal decomposition algorithm are necessary.

In addition, the generating topographies and associated internal wave fields considered here are assumed to be two-dimensional. While there are several topographic features in the oceans which may be considered approximately two-dimensional (e.g. the Mid-Atlantic Ridge [St. Laurent and Garrett, 2002]), there are a great deal more features for which this assumption does not hold. However, when considering internal wave fields generated by three-dimensional

topographic features, additional physics need to be considered. For example, while in the two-dimensional case, perturbed fluid parcels are forced over the generating topography, this may not necessarily be the case when the topography is three-dimensional, because the fluid parcels can flow around, as well as over top of, the topography [Dalziel et al., 2011]. For certain values of ω/N, various out-of-plane flow features have been observed in both numerical simulations and experiments involving three-dimensional topography such as strong non-oscillatory flows perpendicular to the forcing direction, boundary layer currents, and out-of-plane harmonic internal waves [King et al., 2009, 2010].

Finally, the modal decomposition algorithm in its present form assumes the wave field in question is linear. However, Echeverri et al. [2009] note that nonlinear effects become significant as the excursion parameter, χ (defined in § 2.2), exceeds approximately 15%. In this respect, wave-wave interactions (e.g. the Parametric Subharmonic Instability) can cause energy within the internal wave field to be transferred to different frequencies and length scales [Korobov and Lamb, 2008], and are known to play a role in internal wave breaking and mixing in the ocean [St. Laurent and Garrett, 2002]. Although this algorithm is able to consider polychromatic wave fields, the superposition of nonlinear waves is a considerably more complicated process than that of linear waves. Modifications to the modal decomposition algorithm to allow for the evolution of the wave field due to such nonlinear effects, though nontrivial, would further extend the algorithm's applicability to geophysical scenarios of interest.

Bibliography

S. B. Dalziel, M. D. Patterson, C. P. Caulfield, and S. Le Brun. The structure of low Froude-number lee waves over an isolated obstacle. *Journal of Fluid Mechanics*, 689:3–31, 2011.

E. Di Lorenzo, W. R. Young, and S. Llewellyn Smith. Numerical and analytical estimates of M_2 tidal conversion at steep oceanic ridges. *Journal of Physical Oceanography*, 36(6):1072–1084, 2006.

P. Echeverri and T. Peacock. Internal tide generation by arbitrary two-dimensional topography. *Journal of Fluid Mechanics*, 659:247–266, 2010.

P. Echeverri, M. R. Flynn, K. B. Winters, and T. Peacock. Low-mode internal tide generation by topography: an experimental and numerical investigation. *Journal of Fluid Mechanics*, 636:91–108, 2009.

M. R. Flynn and B. R. Sutherland. Intrusive gravity currents and internal gravity wave generation in stratified fluid. *Journal of Fluid Mechanics*, 514: 355–383, 2004.

T. Gerkema and H. van Haren. Absence of internal tidal beams due to non-uniform stratification. *Journal of Sea Research*, pages 6–11, in press, 2012.

B. King, H. P. Zhang, and H. L. Swinney. Tidal flow over three-dimensional topography in a stratified fluid. *Physics of Fluids*, 21(116601):1–10, 2009.

B. King, H. P. Zhang, and H. L. Swinney. Tidal flow over three-dimensional topography generates out-of-forcing-plane harmonics. *Geophysical Research Letters*, 37(L14606):1–5, 2010.

B. King, M. Stone, H. P. Zhang, T. Gerkema, M. Marder, R. B. Scott, and H. L. Swinney. Buoyancy frequency profiles and internal semidiurnal tide turning depths in the oceans. *Journal of Geophysical Research*, 117(C04008):1–15, 2012.

A. S. Korobov and K. G. Lamb. Interharmonics in internal gravity waves generated by tide-topography interaction. *Journal of Fluid Mechanics*, 611:61–95, 2008.

S. G. Llewellyn Smith and W. R. Young. Tidal conversion at a very steep ridge. *Journal of Fluid Mechanics*, 495:175–191, 2003.

M. Mathur and T. Peacock. Internal wave beam propagation in non-uniform stratifications. *Journal of Fluid Mechanics*, 639:133–152, 2009.

F. Pétrélis, S. Llewellyn Smith, and W. R. Young. Tidal conversion at a submarine ridge. *Journal of Physical Oceanography*, 36(6):1053–1071, 2006.

S. Saidi, M. Mercier, P. Echeverri, M. Mathur, and T. Peacock. iTides manual. `http://sourceforge.net/projects/itides/`, 2012. [accessed 07-05-2012].

L. St. Laurent and C. Garrett. The role of internal tides in mixing the deep ocean. *Journal of Physical Oceanography*, 32:2882–2899, 2002.

B. Sutherland. *Internal Gravity Waves*. Cambridge University Press, Cambridge, UK, 2010. ISBN 978-0-521-83915-0.

J. R. Taylor. *An Introduction to Error Analysis*. University Science Books, Sausalito, CA, second edition, 1997. ISBN 0-935702-75-X.

Appendix A

Implementation in MATLAB

A.1 FFT routine for frequency recovery

The following is the MATLAB routine used for finding the frequency information of a given internal wave field for the scenario where the forcing frequencies are unknown *a-priori*. This script leverages the built-in MATLAB functions `fft` for the fast Fourier transform and `window` for constructing the window function. Additionally, `zeros` and `linspace` are used to create various arrays and vectors, and several of MATLAB's plotting functions are employed. Note that the vertical velocity timeseries data is loaded in from an external file.

```
%% Parameter input.
% Exact forcing freqs. (rad/s):
om=0.73*[0.10 0.25 0.50 1.0/sqrt(2.0)...
    0.75 sqrt(3.0)/2.0 0.90];
eN=0.73;  % Buoy. freq. (rad/s).
sample_time=1/4;  % sample_time=period/fpc.
%% End of parameter input.

% Calculate sample frequency (rad/s):
sample_freq=2.0*pi/sample_time;

%% Load velocity timeseries data.
load output1; w=wt; clear wt;
[nz,nt]=size(w);

%% Create array of zeros
extended_time=3000; % "Extended" time for array of zeros
% Total number of zeros needed:
extended_points=ceil(extended_time/sample_time);

%% Initialize arrays.
w_extended=zeros(nz,extended_points);
```

```
NFFT=2^nextpow2(extended_points);
wfft=zeros(nz,NFFT);

%% Select a window function.
option=3;
if option==0
    w1=window(@rectwin,nt); % Rectangular window
elseif option==1
    w1=window(@parzenwin,nt); % Parzen window
elseif option==2
    w1=window(@tukeywin,nt,0.9); % Tukey window
elseif option==3
    w1=window(@gausswin,nt); % Gauss window
elseif option==4
    w1=window(@barthannwin,nt); % Bartlett-Hann window
elseif option==5
    w1=window(@hamming,nt); % Hamming window
elseif option==6
    w1=window(@blackmanharris,nt); % Blackman-Harris window
else
    w1=window(@bartlett,nt); % Bartlett window
end

%% Compute FFT then average over z.
for ij=1:nz
 w_extended(ij,1:nt)=w(ij,:).*w1';
 wfft(ij,:)=fft(w_extended(ij,:),NFFT)/nt;
end
meanwfft=mean(wfft(1:nz,:));

%% Define frequency vector. (See matlab doc. on 'fft').
freq=0.5*sample_freq*linspace(0.0,1.0,NFFT/2);

%% Plot results.
figure(10);
hold on; box on;
set(gca,'fontsize',18);
plot(freq/eN,2.0*abs(meanwfft(1:NFFT/2)),'b-','linewidth',2);
maxheight=max(2.0*abs(meanwfft(1:NFFT/2)));
for j=1:length(om) % Plot location of exact forcing freqs.
    plot([om(j)/eN om(j)/eN],[0.0 maxheight],'r--');
end
% Plot location of buoyancy frequency:
plot([1 1],[0.0 maxheight],'k--','linewidth',2);
xlim([0 1.1]);
xlabel(['{\it\omega}/{\itN}'],'fontsize',18);
ylabel('Power [arb. units]','fontsize',18);
hold off;
```

A.2 Mode recovery in a linear stratification

The following is the MATLAB code used to implement the modal decomposition algorithm for the scenario of an internal wave field forced by multiple forcing frequencies with a linear background stratification (constant buoyancy frequency N). Several of MATLAB's internal functions are used in this script, including `trapz` for finding matrix and column vector elements and `linsolve` when solving the matrix equation $A\boldsymbol{\Upsilon} = \mathbf{b}$ for $\boldsymbol{\Upsilon}$. Arrays and vectors are initialized using `zeros` and `linspace`. The resulting mode strength information is displayed using several of MATLAB's plotting functions. The vertical velocity timeseries data to be analyzed is loaded in from an external file.

```
%% Parameter input (mks units).
anu=1e-6; % Fluid viscosity (m2/s).
h=0.3; % Fluid depth (m).
om=0.73*[0.10 0.25 0.50 1.0/sqrt(2.0)...
    0.75 sqrt(3.0)/2.0 0.90];  % Exact wave freqs (rad/s).
%om=[.0737 0.1842 0.3683...
    %0.5157 0.5464 0.6323 0.6569]; % FFT freqs (rad/s).
eN=0.73; % Buoy. freq. (rad/s).
excur=[0.1 0.015569979 0.003481553 0.001421338...
    0.001181813 0.000670025 0.000540847]; % Excursion delta_j (m).
kmax=7; % Number of wavemodes.
horx=0.30; % Horizontal location (m).
t_final=599.75; % Length of timeseries (s).

J=length(om); % Number of frequencies to resolve.
period=2.0*pi./om; % Wave periods.
UU=excur.*om; % Horizontal velocity.
amu=sqrt(eN^2./om.^2-1.0); % mu parameter (SGLS & WRY paper).
% Note however: (i) non-rotating, and, (ii) non-hydrostatic.
% Viscosity parameter:
parm=anu/2.0*pi^2.0*eN^4.0./om/h^2.0./(eN^2.0-om.^2.0).^2.0;
x=pi*horx./amu/h; % Non-dim. horz. position.

%% Load vertical velocity timeseries data.
load output1; w=wt; clear wt;
[nz,nt]=size(w);

%% Initialize arrays.
varphi=zeros(1,J); % Phase parameter.
beta=zeros(kmax,nt); % Beta.
bowtie=zeros(J,kmax); % Coefficient for A matrix.
coli=zeros(2*J,kmax); % Column vector b.
upsi=zeros(2*J,kmax); % Column vector upsilon.
mat1=zeros(2*J,2*J); % A matrix.
```

```
gnc=zeros(J,kmax); % Column vector for complex gamma.

%% Integrate in Z.
Z=linspace(0.0,pi,nz); Z=Z';
for k=1:kmax
 for tn=1:nt
  beta(k,tn)=trapz(Z,w(:,tn).*sin(k*Z));
 end
end

%% Integrate in time.
t=linspace(0.0,t_final,nt);
option=0;

for k=1:kmax % Set up matrix equation for each mode.
 for j=1:J
  coli(2*j-1,k)=trapz(t,beta(k,:).*cos(om(j)*t));
  coli(2*j,k)  =trapz(t,beta(k,:).*sin(om(j)*t));
  for jj=1:J
   mat1(2*j-1,2*jj-1)= pi/2.0*UU(jj)/amu(jj)...
       *exp(-k^3.0*x(jj)*parm(jj))...
       *trapz(t,cos(k*x(jj)+pi/2.0-om(jj)*t).*cos(om(j)*t));
   mat1(2*j-1,2*jj)  =-pi/2.0*UU(jj)/amu(jj)...
       *exp(-k^3.0*x(jj)*parm(jj))...
       *trapz(t,sin(k*x(jj)+pi/2.0-om(jj)*t).*cos(om(j)*t));
   mat1(2*j  ,2*jj-1)= pi/2.0*UU(jj)/amu(jj)...
       *exp(-k^3.0*x(jj)*parm(jj))...
       *trapz(t,cos(k*x(jj)+pi/2.0-om(jj)*t).*sin(om(j)*t));
   mat1(2*j  ,2*jj)  =-pi/2.0*UU(jj)/amu(jj)...
       *exp(-k^3.0*x(jj)*parm(jj))...
       *trapz(t,sin(k*x(jj)+pi/2.0-om(jj)*t).*sin(om(j)*t));
  end
 end
 % Invert matrix equation to solve for upsilon:
 upsi(:,k)=linsolve(mat1,coli(:,k));
 for j=1:J % Calculate gamma values from upsilon.
  gnc(j,k)=(upsi(2*j-1,k)+k^2.0*parm(j)*upsi(2*j,k))...
      /(1.0+(k^2.0*parm(j))^2.0)...
      +1i*(upsi(2*j,k)-k^2.0*parm(j)...
      /(1.0+(k^2.0*parm(j))^2.0)*(upsi(2*j-1,k)...
      +k^2.0*parm(j)*upsi(2*j,k)));
 end
end

%% Compare reconstructed modes with values
%% from synthetic data.

% Load in gamma values, both real and imaginary parts:
gammatheor=cell(J,1);
fortstrings={'fort.33E';'fort.33C';'fort.33A';...
    'fort.33'; 'fort.33D';'fort.33B';'fort.33F'};

for j=1:J
    clear fort
    fortfile=fortstrings{j,1};
```

```
    load(fortfile)
    gammatheor(j,1)={fort(2:end,2)+1i*fort(2:end,3)};
end

% Set number of rows and columns of subplots:
numrows=floor(sqrt(J));
numcolumns=ceil(sqrt(J));
if numrows*numcolumns<J
    numrows=numrows+1;
end

% Plot magnitudes of complex mode strengths:
for j=1:J
    figure(25); hold on; box on;
    subplot(numrows,numcolumns,j);
    hold on;
    set(gca,'fontsize',14);
    plot(linspace(1,kmax,kmax),abs(gnc(j,1:kmax)),...
        'ko','markersize',8);
    gammatheorplot=abs(gammatheor{j,1});
    plot(linspace(1,kmax,kmax),gammatheorplot(1:kmax),'k-');
    xlabel('Mode number, n','fontsize',14);
    ylabel('|{\it\gamma_n}|','fontsize',14);
    titlestring=['{\it\omega}/{\itN} = ' num2str(om(j)/eN)];
    title(titlestring);
    xlim([0 kmax+1]);
    hold off;
end

% Plot real part of complex mode strengths:
for j=1:J
    figure(26); hold on; box on;
    subplot(numrows,numcolumns,j);
    hold on;
    set(gca,'fontsize',14);
    plot(linspace(1,kmax,kmax),real(gnc(j,1:kmax)),...
        'ko','markersize',8);
    gammatheorplot=real(gammatheor{j,1});
    plot(linspace(1,kmax,kmax),gammatheorplot(1:kmax),'k-');
    xlabel('Mode number, n','fontsize',14);
    ylabel('Re({\it\gamma_n})','fontsize',14);
    titlestring=['{\it\omega}/{\itN} = ' num2str(om(j)/eN)];
    title(titlestring);
    xlim([0 kmax+1]);
    hold off;
end

% Plot imaginary part of complex mode strengths:
for j=1:J
    figure(27); hold on; box on;
    subplot(numrows,numcolumns,j);
    hold on;
    set(gca,'fontsize',14);
    plot(linspace(1,kmax,kmax),imag(gnc(j,1:kmax)),...
        'ko','markersize',8);
```

```
    gammatheorplot=imag(gammatheor{j,1});
    plot(linspace(1,kmax,kmax),gammatheorplot(1:kmax),'k-');
    xlabel('Mode number, n','fontsize',14);
    ylabel('Im({\it\gamma_n})','fontsize',14);
    titlestring=['{\it\omega}/{\itN} = ' num2str(om(j)/eN)];
    title(titlestring);
    xlim([0 kmax+1]);
    hold off;
end
```

A.3 Mode recovery in a nonlinear stratification

The following is the MATLAB code used to implement the modal decomposition algorithm for the scenario of a polychromatic internal wave field in nonlinear background stratification. Several of MATLAB's internal functions are used in this script, including `trapz` for finding matrix and column vector elements and `linsolve` when solving the matrix equation $A\gamma = \mathbf{b}$ for γ. The functions `zeros` and `linspace`, and the plotting functions are used as in § A.1 and § A.2. Both the buoyancy frequency profile $N(z)$ and the vertical velocity timeseries data are loaded from external files.

```
%% Parameter input (mks units).
anu=0; % Fluid viscosity (m2/s).
h=5000.0; % Fluid depth (m).
f0=2.0*pi/24.0/3600.0*sind(15.0); % Coriolis freq. (rad/s).
% Load vertically-varying buoy. freq. (rad/s):
load stratification_SGLS_WRY_2003_WOD;eN=N';
clear stratification_SGLS_WRY_2003_WOD;
% Dominant wave frequencies (rad/s):
om=[6.7598e-5 7.2921e-5 1.3788e-4 1.4052e-4 1.4544e-4];
% Excursion delta_j (m):
excur=[0.003/6.7598e-5 0.003/7.2921e-5 0.003/1.3788e-4...
    0.006/1.4052e-4 0.004/1.4544e-4];
horx=15000; % Horizontal location (m).
t_final=601200.00; % Length of timeseries (s).

kmax=7; % Number of wavemodes.
J=length(om); % Number of frequencies to resolve.
period=2.0*pi./om; % Wave periods.
UU=excur.*om; % Horizontal velocity.

%% Define WKB-related variables.

Nbar=zeros(1,J);
N_fancy=zeros(nz,J);
amu=zeros(1,J);
```

```
parm=zeros(1,J);
for j=1:J
    % Nbar_j:
    Nbar(j)=trapz(linspace(0,h,length(eN)),...
        sqrt(eN.^2-om(j)^2))/h;
    % mathcal{N}_j:
    N_fancy(:,j)=sqrt(eN.^2-om(j)^2)./Nbar(j);
    % mu parameter (non-hydrostatic, with rotation):
    amu(j)=Nbar(j)/sqrt(om(j)^2-f0^2);
end
x=pi*horx./amu/h; % Non-dim. horz. position.

%% Load vertical velocity timeseries data.
load output1; w=wt; clear wt;
[nz,nt]=size(w);

%% Initialize arrays.
beta=zeros(kmax,nt,J); % Beta.
bowtie=zeros(J,kmax); % Coefficient for A matrix.
coli=zeros(2*J,kmax); % Column vector b.
upsi=zeros(2*J,kmax); % Column vector for matrix inversion.
mat1=zeros(2*J,2*J); % A matrix.
gnc=zeros(J,kmax); % Column vector for complex gamma.

%% Integrate in z.
z=(0:(nz-1))/(nz-1)*pi;
Z=zeros(nz,J);
zoriginal=z*h/pi;
N_ave=1/h*trapz(zoriginal,eN); % Ave. buoy. freq. (rad/s)

for j=1:J % Define scaled vertical coordinate Z_j.
 Z(1,j)=0;
 for zloc=2:nz
  zpos=(zloc-1)*h/(nz-1);
  integral=trapz(linspace(0,zpos,zloc),...
    sqrt(eN(1:zloc).^2-om(j)^2));
  Z(zloc,j)=pi/h/Nbar(j)*integral;
 end
 for k=1:kmax % Calculate beta.
  for tn=1:nt
   beta(k,tn,j)=trapz(z*h/pi,w(:,tn)/sign(horx)...
    .*sin(k*Z(:,j))./sqrt(N_fancy(:,j)).*(eN.^2-om(j)^2));
  end
 end
end

%% Integrate in time.
t=linspace(0.0,t_final,nt);
option=0;

for k=1:kmax % Set up matrix equation for each mode.
 for j=1:J
  coli(2*j-1,k)=trapz(t,beta(k,:,j).*cos(om(j)*t));
  coli(2*j,k)  =trapz(t,beta(k,:,j).*sin(om(j)*t));
  for jj=1:J
```

```
   phi=abs(k*x(jj))+pi/2.0; % Phase parameter.
   mat1(2*j-1,2*jj-1)= Nbar(j)^2*h/2.0*UU(jj)/amu(jj)...
       *exp(-k^3.0*x(jj)*parm(jj))...
       *trapz(t,cos(phi-om(jj)*t).*cos(om(j)*t));
   mat1(2*j-1,2*jj)  =-Nbar(j)^2*h/2.0*UU(jj)/amu(jj)...
       *exp(-k^3.0*x(jj)*parm(jj))...
       *trapz(t,sin(phi-om(jj)*t).*cos(om(j)*t));
   mat1(2*j  ,2*jj-1)= Nbar(j)^2*h/2.0*UU(jj)/amu(jj)...
       *exp(-k^3.0*x(jj)*parm(jj))...
       *trapz(t,cos(phi-om(jj)*t).*sin(om(j)*t));
   mat1(2*j  ,2*jj)  =-Nbar(j)^2*h/2.0*UU(jj)/amu(jj)...
       *exp(-k^3.0*x(jj)*parm(jj))...
       *trapz(t,sin(phi-om(jj)*t).*sin(om(j)*t));
  end
 end
 % Invert matrix equation to solve for gamma vector.
 upsi(:,k)=linsolve(mat1,coli(:,k));
 for j=1:J % Find gamma in complex form.
  gnc(j,k)=upsi(2*j-1,k)+1i*upsi(2*j,k);
 end
end


%% Compare reconstructed modes with values
%% from synthetic data.

%Load in gamma values, both real and imaginary parts.
gammatheor=cell(J,1);
datastrings={'wavefield_O1_WOD_subsuper';...
    'wavefield_K1_WOD_subsuper';...
    'wavefield_N2_WOD_subsuper';...
    'wavefield_M2_WOD_subsuper';...
    'wavefield_S2_WOD_subsuper'};

for j=1:J
    datafile=datastrings{j,1};
    load(datafile)
    if horx>=0
        gammatheor(j,1)={modes_t};
    else
        gammatheor(j,1)={modes_r};
    end
    clear(datafile)
end

% Set number of rows and columns of subplots:
numrows=floor(sqrt(J));
numcolumns=ceil(sqrt(J));
if numrows*numcolumns<J
    numrows=numrows+1;
end

% Plot magnitudes of complex mode strengths.
for j=1:J
    figure(25);hold on; box on;
```

```
    subplot(numrows,numcolumns,j);
    hold on;
    set(gca,'fontsize',14);
    plot(linspace(1,kmax,kmax),abs(gnc(j,1:kmax)),...
        'ko','markersize',8);
    gammatheorplot=abs(gammatheor{j,1});
    plot(linspace(1,kmax,kmax),gammatheorplot(1:kmax),'k-');
    xlabel('Mode number, n','fontsize',14);
    ylabel('|{\it\gamma_n}|','fontsize',14);
    titlestring=['{\it\omega/\itN_{ave}} = '...
        num2str(om(j)/N_ave)];
    title(titlestring);
    xlim([0 kmax+1]);
    hold off;
end

% Plot real part of complex mode strengths.
for j=1:J
    figure(26); hold on; box on;
    subplot(numrows,numcolumns,j);
    hold on;
    set(gca,'fontsize',14);
    plot(linspace(1,kmax,kmax),real(gnc(j,1:kmax)),...
        'ko','markersize',8);
    gammatheorplot=real(gammatheor{j,1});
    plot(linspace(1,kmax,kmax),gammatheorplot(1:kmax),'k-');
    xlabel('Mode number, n','fontsize',14);
    ylabel('Re({\it\gamma_n})','fontsize',14);
    titlestring=['{\it\omega/\itN_{ave}} = '...
        num2str(om(j)/N_ave)];
    title(titlestring);
    xlim([0 kmax+1]);
    hold off;
end

% Plot imaginary part of complex mode strengths.
for j=1:J
    figure(27); hold on; box on;
    subplot(numrows,numcolumns,j);
    hold on;
    set(gca,'fontsize',14);
    plot(linspace(1,kmax,kmax),imag(gnc(j,1:kmax)),...
        'ko','markersize',8);
    gammatheorplot=imag(gammatheor{j,1});
    plot(linspace(1,kmax,kmax),gammatheorplot(1:kmax),'k-');
    xlabel('Mode number, n','fontsize',14);
    ylabel('Im({\it\gamma_n})','fontsize',14);
    titlestring=['{\it\omega/\itN_{ave}} = '...
        num2str(om(j)/N_ave)];
    title(titlestring);
    xlim([0 kmax+1]);
    hold off;
end
```